RHIC II FEASIBILITY STUDY

Table of Contents

1 Introduction

RHIC II will be a high luminosity upgrade for RHIC, to be achieved through electron cooling at various energies of the full RHIC beam inventory. Electron cooling will counteract the heating of the beam caused by Intra-Beam Scattering (IBS), eliminating the emittance growth, bunch-lengthening and beam loss which result from this heating. Electron cooling of RHIC gold stored beams will increase the average store luminosity to $7x10^{27}$ $cm^{-2}s^{-1}$. This is about 15 times higher than presently achieved. The proposed electron beam-cooling scheme for RHIC uses a double pass, energy-recovery superconducting linac to generate the electron beam needed for cooling both RHIC rings. To cool ions from protons to gold at store, we need electron beam energies of 54 MeV, at bunch charge of 5 nC and emittance smaller than 4 microns (rms, normalized), at a repetition frequency of 9.4 MHz. The necessary transverse and longitudinal electron beam brightness will be generated by a CW laser photocathode RF gun as the injector. The electron accelerator is a superconducting, energy-recovery linac.
Electron cooling for RHIC presents various technical challenges. While electron cooling has been known for many years, it has never been applied to conditions anywhere near the conditions of RHIC.

1) At 54 MeV the RHIC cooler will be by far the highest energy cooler, e.g. the FNAL recycler cooler is 4.5 MeV.
2) The RHIC cooler is the only machine designed to use a bunched electron beam and requires a very high average electron current due to the high ion energy.
3) The RHIC cooler will be the first instance in which a collider will be directly cooled.

For the past five years the Collider-Accelerator Department has been engaged in developing our knowledge base of electron cooling and its associated scientific and technical issues. Feasibility of the luminosity increase of RHIC via electron cooling was demonstrated through numerical simulations of the electron cooling process and numerical simulations of the electron beam dynamics of the electron cooler. The electron cooling simulation work was done with codes that have been benchmarked by a series of experiments on cooler rings, in particular the FNAL Recycler ring cooler which is closest in characteristics to the RHIC cooler than any other electron cooler. IBS at RHIC was benchmarked by measurements on RHIC. The electron cooling codes were benchmarked against other codes and are also known to agree with experimental results. Thus we have confidence in the ability of the Collider-Accelerator Department to carry out the electron cooling element of the RHIC II luminosity upgrade.

In this document we present the simulations and benchmarking that document the feasibility of RHIC II. The introduction (Chapter 1) includes a minimal general description of the facility including layout drawings and parameter tables. Chapter 2 describes the RHIC ion beam lattice modifications which accommodate an electron cooler at IP2. Chapter 3 provides the electron cooling physics and benchmarking and Chapter 4 provides the electron cooler beam dynamics.

1.1 General features

Facility layout

The layout of the RHIC electron cooler is shown in Figure 1.1. The electron cooling system will be located in the 2 o'clock Interaction Point (IP2) of RHIC. It comprises the RHIC beam tunnel section in which the electron beam is co-propagated with the ion beams of the two RHIC rings, the Blue Ring and the Yellow Ring, and the electron beam generation source and accelerator, located outside the RHIC ring. The cooling section in IP2 is designed to maximize the length of the cooling sections as well as provide a large ion beta function for optimal cooling. The electron source is a laser-photocathode superconducting RF gun, and the accelerator is a superconducting Energy Recovery Linac (ERL). It is designed to provide a high beam charge at the RHIC ion beam repetition frequency at a low emittance. The electron gun, ERL and service buildings are located at the lower right corner of Figure 1, inside the area bounded by the RHIC ring tunnel.

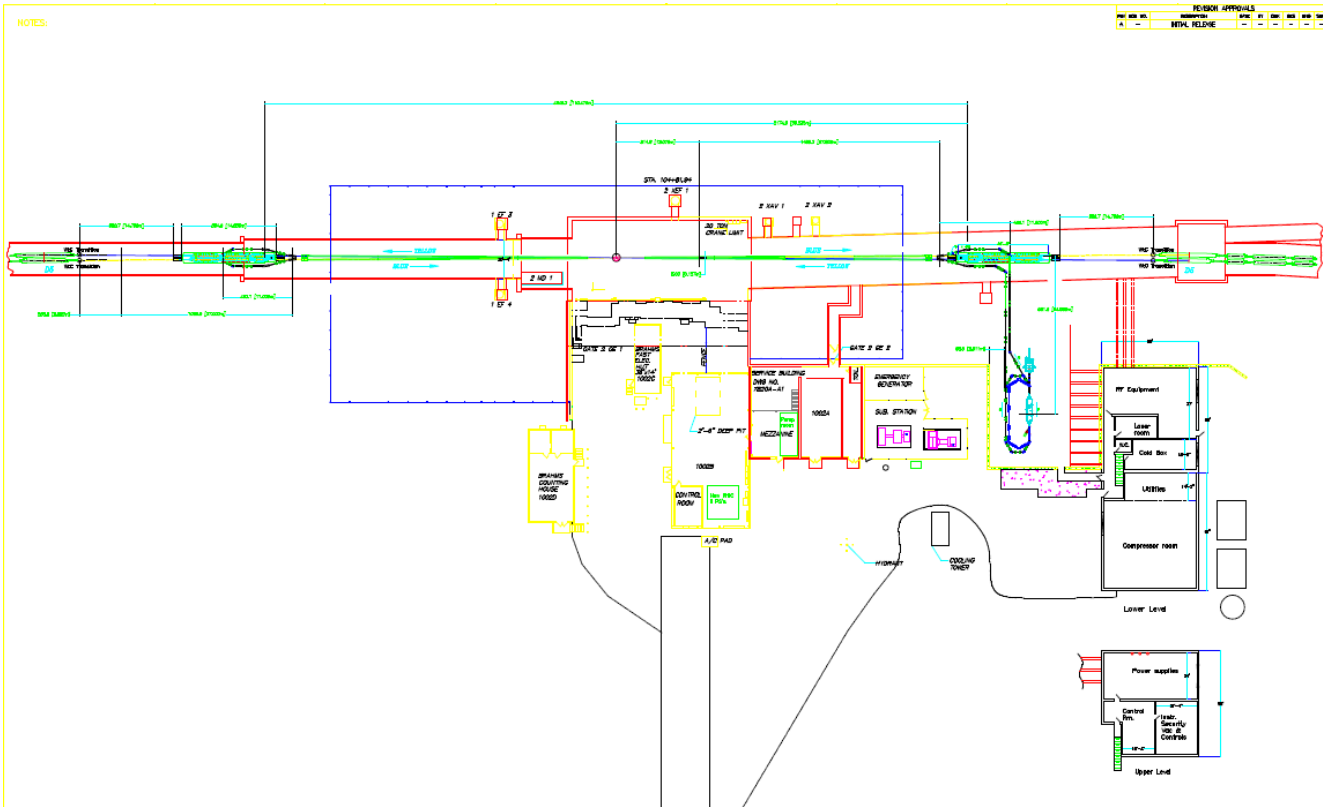

Figure 1.1 Layout of the RHIC electron cooler in IP2.

A detailed description of the cooling section is provided in Chapter 2 for the ion beam optics and layout, and in Chapter 4 for the electron beam optics and layout. Briefly we note that the electron beam will enter the RHIC tunnel through a new access tunnel. This access tunnel holds both outgoing beam from the electron accelerator and return beam. The outgoing beam is turned left, and following a matching section is merged with the ion beam of the Yellow ring. The co-propagating electron and ion beams travel for about 100 meters in a special beam transport which is described in Chapter 3. This beam transport channel incorporates ample beam diagnostics and beam steerers to provide a precise overlap and small angle between the ions and electrons as well as undulators

aimed at reduction of the recombination rate for heavy ions, solenoids to compensate for coherent angles in the electron beam induced by space-charge and vacuum hardware. The electron beam is separated from the ions of the Yellow ring at the left end of the interaction region, it then makes a turn about carefully designed to match the electron beam again to the ion bunches of the Blue ring both in time and in beam parameters and then merged with the ion beam of the Blue ring. The electrons cool the Blue ring ions traveling clockwise (right in the figure) and then separated and returned to the ERL.

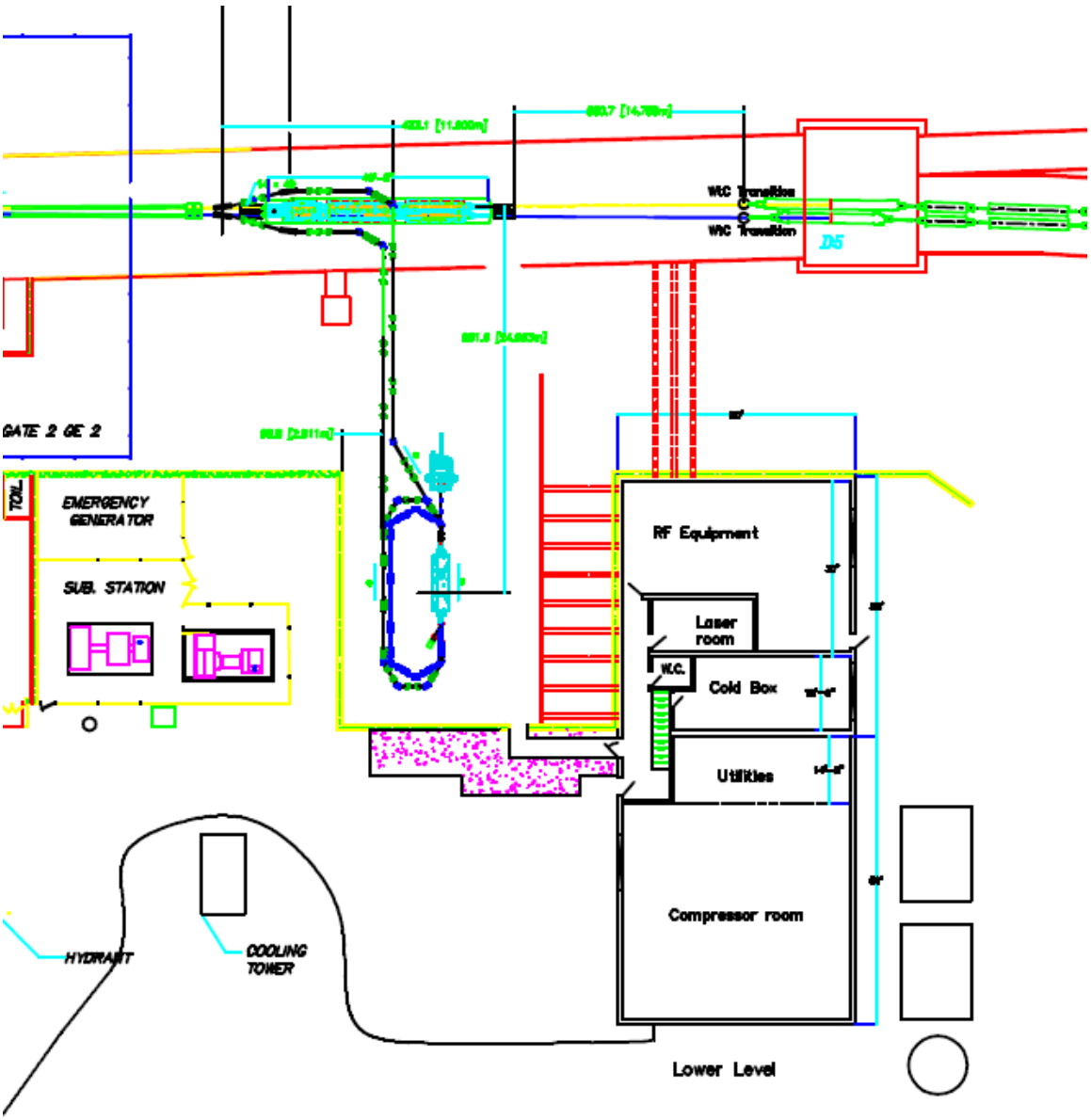

Figure 1.2 Detail of the RHIC II electron cooler.

Figure 1.2 shows a detail of the Energy Recovery Linac (ERL) used for generating the high-current, high-charge electron beam. The beam is generated in a superconducting laser photocathode RF gun, accelerated to about 54 MeV in a two-pass superconducting ERL, sent to the ion rings, then returns (as described above) through the access tunnel to the ERL. There it is decelerated in two passes and dumped at essentially the injection (gun) energy.

Nearby service building hold the RF equipment, control room, power supply, beam instrumentation, vacuum, cryogenics, personnel and machine safety, cooling water systems, power systems etc.

1.2 List of parameters

In this section we provide a short list of the main parameters for the RHIC electron cooler. More parameters are listed in greater detail in tables provided in the body of this report.

Common Parameters
Protons to gold ions at 100 GeV/A
Ion number per bunch 10^9 gold or $2x10^{11}$ protons
Ion charge 79 or 1
Initial ion normalized rms emittance 2.5 μm
(in both transverse planes)
Initial rms momentum spread $5 \cdot 10^{-4}$
Initial rms bunch length 19 cm
110 stored bunches
RF frequency (store) 197.043
Bunch frequency 9.383 MHz
ERL RF frequency 703.75 MHz
Harmonic number 2520
RF voltage 3 MV

Cooling section
Wiggler, helical, length 80 meters
Magnetic field range 0.001 Tesla
Wiggler pitch period 8 cm
Rms magnetic error $\leq 5\ 10^{-6}$
Ions β function in wiggler ≥ 400 m
Max rms beam size: 6.5 mm
Vacuum chamber ID 12*rms_size: 8 cm diameter

Electron beam (for 100 GeV/n cooling)
Kinetic energy 54.3 MeV
Bunch charge 5 nC
rms bunch length ~1 cm
rms normalized emittance ≤4 μm
rms relative momentum spread < 0.0005

ERL RF
1½ SRF Gun:
703.75 MHz, 5 MeV energy at the exit.
Two 5 cell SRF cavities:
703.75 MHz cavities,15 MeV energy gain per cavity
One 3rd harmonic SRF cavity:
2.111 GHz, 3.5 MeV energy gain per cavity

Average store luminosity (with electron cooling) *in units of [$cm^{-2}sec^{-1}$]*
Gold ions: Up to $70x10^{26}$
Protons: Up to $50x10^{31}$

2 RHIC ION BEAM LATTICE FOR ELECTRON COOLING

The current geometry of the RHIC interaction region (IR) must be modified to accommodate the requirements for electron cooling. The requirements are:

1. Moderate β functions of 50 *m* for injection acceptance.
2. Large β functions of 400 *m* through the electron cooling region.
3. Vertical beam separation of 7 *cm* at the interaction point (IP).

To achieve these goals we need to modify the existing RHIC IR. In the sections that follow, we present a proposal on necessary modifications to achieve the above requirements.

2.1 Geometry

To provide enough drift space, we present a local approach has been proposed. In the local approach, only one IR is modified. The crossing dipoles are removed and the strengths for the D5 magnets are adjusted so the beams continue through their respective rings. Fig 2.1.1 shows a schematic of this proposal. The change in geometry causes this insertion to be shorter by 1.996 *mm* than the standard RHIC insertion.

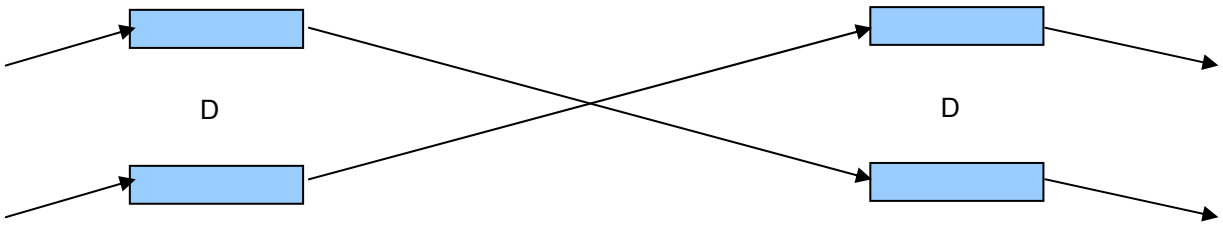

Figure 2.1.1 Schematic for changing only one IR. This approach provides enough drift space to meet the electron cooling requirements. Since the beams can still cross, vertical separation will be required to prevent this.

2.2 Optics

The goal for the optics is to provide a large β function in both planes through a large warm drift space. This β function should be 400 *m*. Furthermore, we would like to reuse as much existing hardware as possible to reduce the overall cost. Without the crossing dipoles, the triplets can be moved much further from the IP providing a large drift space for the electron cooling. Additionally, we will not be using the quadrupoles Q4 and Q5. Due to the need of a large current in the outer Q6, this is replaced with the longer Q4 magnet. The calculated currents assume this change. To find a solution, there is a minimum of 12 constraints as shown in the schematic Fig 2.2.1.

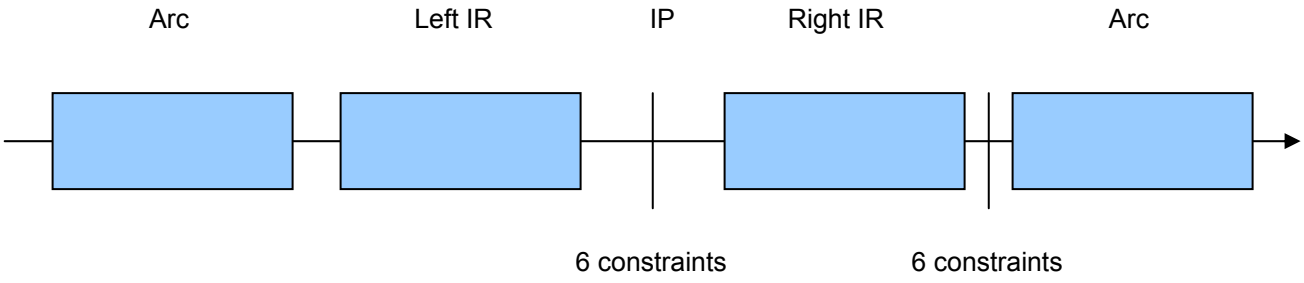

Figure 2.2.1 Schematic showing the minimum of 12 constraints used in the matching. Six constraints at the IP to achieve the large β functions desired and 6 more constraints to match the insertion to the arcs. Additional constraints for controlling the β functions in the IR sections are also used.

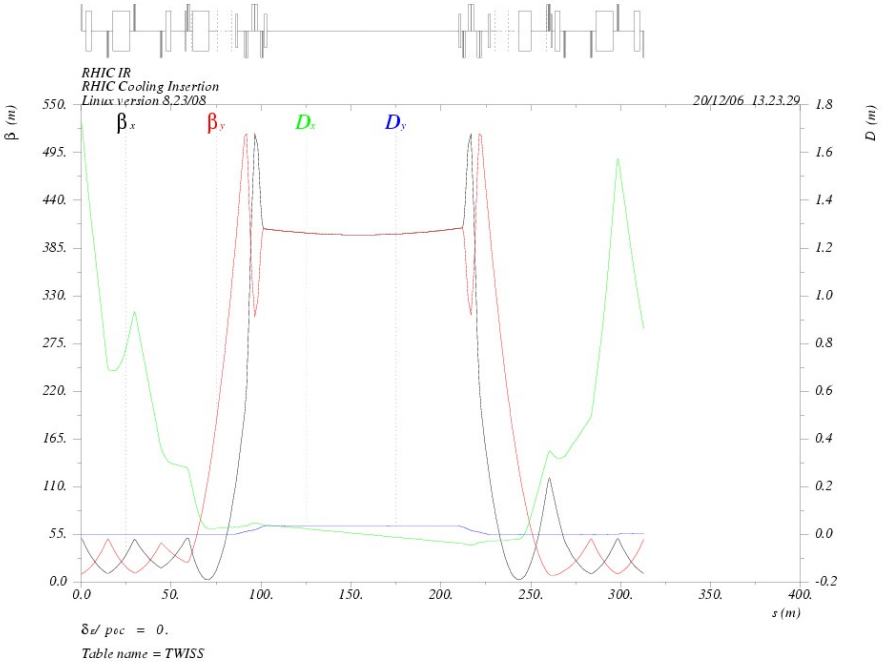

Figure 2.2.2 The Twiss and dispersion functions for the electron cooling section with a 400*m* β functions through the large warm drift space.

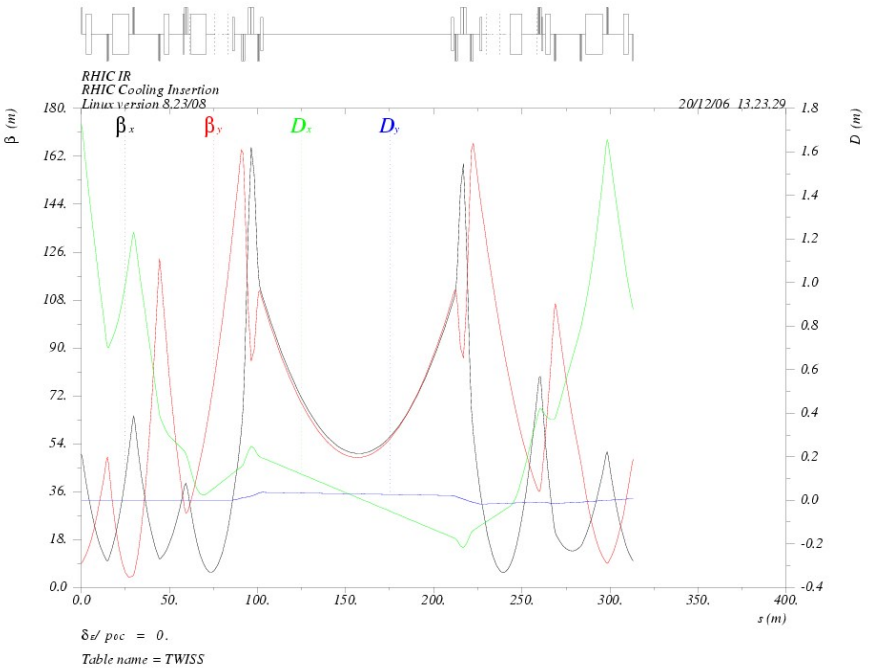

Figure 2.2.3 The Twiss and dispersion functions for the electron cooling section with a 50*m* β functions through the large warm drift space for injection optics.

The optics matching is performed using the MAD program. Fig. 2.2.2 shows the Twiss and dispersion for optics with 400 *m* through the electron cooling region.

Since the β function is large, injection acceptance needs to be addressed. To allow sufficient acceptance, a 50 *m* β insertion is desired. Furthermore, a smooth squeeze path of the power supplies from 50 *m* to 400 *m* is required. Fig. 2.2.3 shows the optics for the 50 *m* β solution.

2.2.1 Vertical Separation Bumps

The vertical separation of the 'blue' and 'yellow' crossing rings was designed without affecting the existing horizontal solution of [~110 *m* long cooling interaction region with the β_x~400 *m* high betatron function throughout]. The vertical dispersion matching is accomplished by the simplest possible solution with the four small vertical bending magnets. Four magnets per ring, 1.1 *m* long, are identical, and placed right before and after the triplet cryostat. The crossing point at the center of the interaction region needs to have two rings vertically separated. The vertical separation at the crossing region (see Fig. 2.2.4) is 7 *cm*. This is satisfying very much the aperture limitations set up in RHIC because the sigma of the beam is $\sigma = \sqrt{\frac{(\varepsilon_N/\pi)\beta_y}{6(\gamma\beta)}} = \sqrt{\frac{20\times10^{-6}\cdot 400}{6\cdot 108}} = 3.5mm$, making the size of the pipe diameter ~ 60 *mm* equal to 17σ.

The long straight sections connect the ends of the D5O magnets from outside ring to the other side of the interaction region with the D5I inside ring and opposite (as presented in figures bellow).
The ~105*m* long straight pipe of one ring is in the horizontal plane is 35*mm* above the ring plane. The solution is schematically shown in both horizontal and vertical projections in Fig. 2.2.5.

The same solution schematically presented in three dimensions is shown in Fig. 2.2.6. Additional drifts to allow the vacuum valves to be placed at the end of the cryostats are provided. At the present triplet cryostat design a distance from the end of the magnetic edge of the quadrupole Q3 to the end of the valve is 2.7059*m*, this is preserved in the present design. The first vertical dipole, as presented in Fig. 2.2.5, is connected to that valve. A distance from the magnetic edge of the quadrupole Q1, on the other side of the cryostat, to the flange to connect the present D0 magnet (to be removed in future) is 1.26465*m*. Additional 0.04872*m* are added for a vacuum valve. The second vertical dipole, presented in Fig. 2.2.5 is connected to the valve.

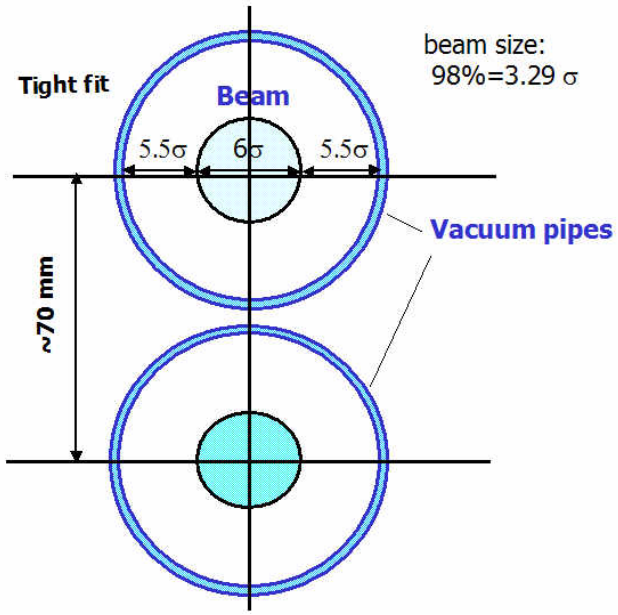

Figure 2.2.4 Two vertically separated rings at the crossing point.

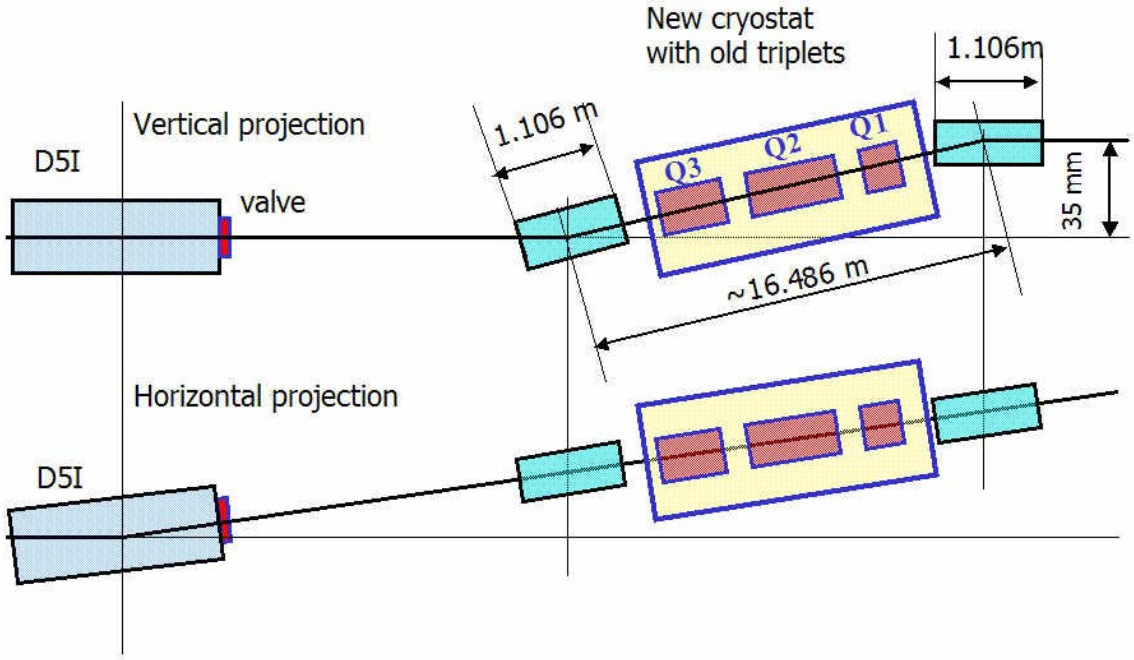

Figure 2.2.5 Vertical and horizontal projections of the two rings, schematically presented at one side of the cooling section of the RHIC straight section.

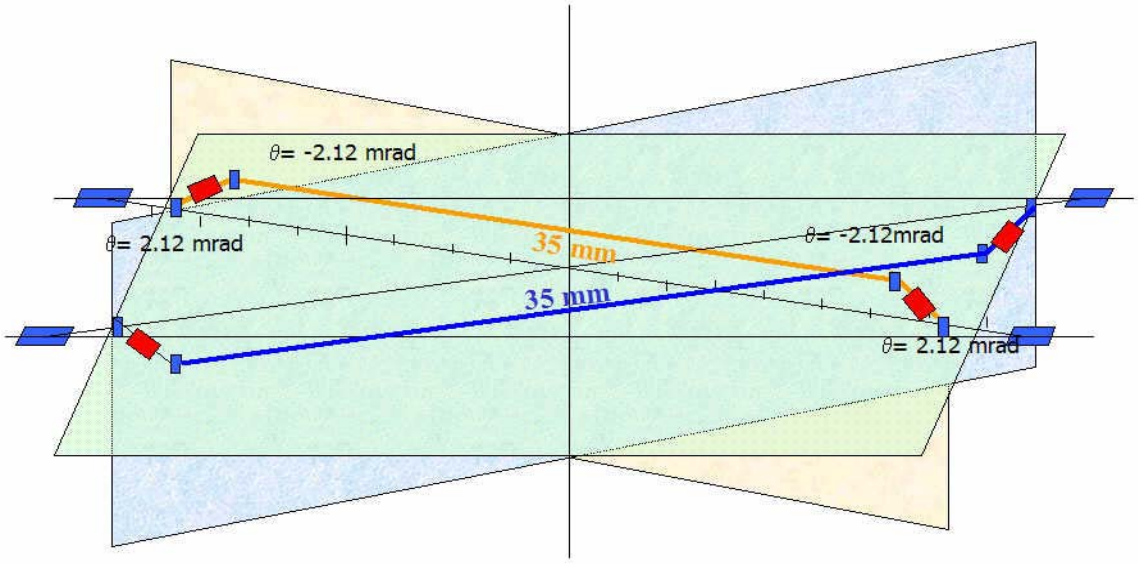

Figure 2.2.6 The vertical separation schematically presented in three dimensions.

2.3 Design procedure

The required vertical separation or geometrical conditions and the vertical dispersion matching are accomplished without affecting the present horizontal design. The vertical separation of 7 *cm* between the two rings is obtained by L_d=1.101 *m* long warm dipole with magnetic field of B_y=1.6 *T*. All dipoles are the same and provide vertical bending angle of θ=2.124 *mrad* at the maximum energy (Bρ=833.9 *Tm*). The required geometrical condition is schematically presented in Fig. 2.3.1.

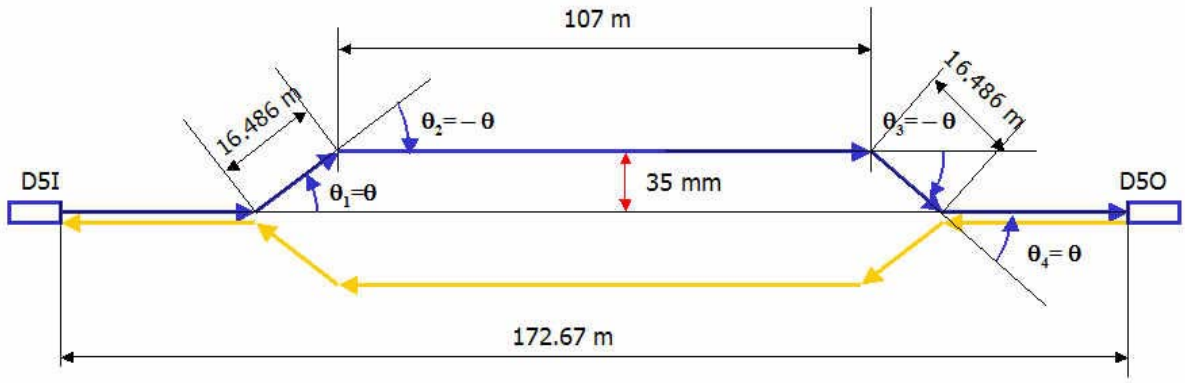

Figure 2.3.1 Geometrical constraints.

The vertical dispersion matching was obtained by placement of the vertical dipoles at the lattice positions with the required vertical betatron functions values. First, the second and third vertical dipole are placed as close as possible to the triplet cryostat to allow the longest free space distance between them, making the longest possible cooling section. The design is presented in the normalized dispersion space in Fig 2.3.2. The horizontal and vertical axes are defined as:

$$\zeta = D_{y}' \sqrt{\beta_y} + \frac{D_y \alpha_y}{\sqrt{\beta_y}} \quad and \quad \chi = \frac{D_y}{\sqrt{\beta_y}}.$$

The vector ξ_1 is defined $\xi_1 = \theta_1 \sqrt{\beta_1}$, while the betatron phase difference between the two vertical dipoles is presented as angle. The strength of the vector representing the second vertical dipole is related to the strength of the first vector as: ξ_2=0.99407 ξ_1. This is a consequence of the relationship between the vectors presented in Fig. 2.3.2.

The matching is achieved by starting from the origin at the end of the last bending dipole labeled as ξ_4. The betatron phase differences between the first and the second dipole and between the second and third dipole are $\phi_{1,2}$=2.48° $\phi_{3,4}$=2.088°, while the phase difference between the second and third dipole is $\phi_{2,3}$= 14.933°.

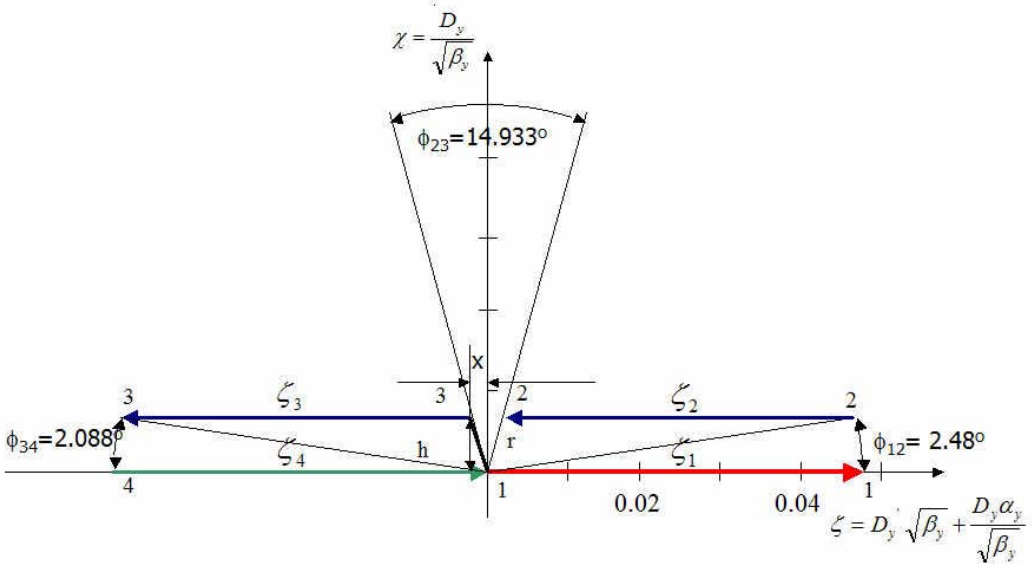

Figure 2.3.2 Four vertical dipoles presented in the normalized dispersion space, showing the final result very close to the origin of the graph, indicating excellent dispersion matching.

$$\zeta_4 \cos \phi_{34} = |\zeta_3| + r \sin \frac{\phi_{23}}{2}$$

$$h = \zeta_4 \sin \phi_{34}$$

$$r = \frac{h}{\cos \frac{\phi_{23}}{2}} = \zeta_4 \frac{\sin \phi_{34}}{\cos \frac{\phi_{23}}{2}}$$

$$\zeta_4 = \frac{\zeta_3}{\cos \phi_{34} - \sin \phi_{34} \tan \frac{\phi_{23}}{2}} = 1.00487 \cdot \zeta_3$$

The second vertical dipole has the same bending direction as well as the strength as the third one $\xi_2 = \xi_3$. The position of the first vertical dipole in the lattice should provide matching conditions presented in the next equations:

$$|\zeta_1| \cos\phi_{12} = |\zeta_2| + r \sin\frac{\phi_{23}}{2}$$

$$h = |\zeta_1| \sin\phi_{12}$$

$$r = \frac{h}{\cos\frac{\phi_{23}}{2}} = |\zeta_1| \frac{\sin\phi_{12}}{\cos\frac{\phi_{23}}{2}}$$

$$\zeta_2 = \frac{\zeta_1}{\cos\phi_{12} - \sin\phi_{12}\tan\frac{\phi_{23}}{2}} = 1.00685 \cdot \zeta_1$$

The interaction region (IR) for the RHIC cooling is designed as a symmetric solution with respect to the center. The quadrupole triplets on one side of the IR follow the same DFD structure. The regular RHIC lattice is made of anti-symmetric triplets: on one side of there is DFD while on the other is FDF. The horizontal betatron function matching of the RHIC cooling section to the rest of the RHIC lattice is accomplished by adjusting the quadrupole strengths in the interaction region between the triplets and the arc magnets. Due to existing asymmetry the vertical dispersion matching is more difficult. The betatron functions in the interaction region are presented in Table 1.

Table 1. Vertical betatron functions in the cooling interaction region

Element	s(m)	β_y	α_y	ν_y
TLSCI1	83.350	348.251	-10.239	0.583
TLSCI1	83.35	348.251	-10.239	0.583
VKCK1	**86.662**	**412.733**	**-11.1537**	**0.5842**
OQ3Q4	90.693	515.016	-12.47	0.586
Q1I	99.722	381.912	-17.599	0.59
TLSCI1	102.427	407.274	0.135	0.591
VKCK2	**103.092**	**407.1369**	**0.133575**	**0.5911**
MCR	156.522	400	0	0.612
VKCK3	**209.952**	**407.1369**	**-0.133575**	**0.6339**
TLSCO	210.617	407.357	-0.136	0.634
Q3O	222.351	513.876	13.187	0.638
VKCK4	**226.4389**	**411.747**	**11.8701**	**0.6397**
TLSCO1	229.694	338.556	10.687	0.641
TLSCI1	83.35	348.251	-10.239	0.583

2.4 Conclusions:

Matching of the vertical dispersion is excellent at the top energy – full cancellation outside of the vertical bending. There will be a small mismatch in the vertical plane from injection to the full energy as the betatron function at the first dipole are not be absolutely the same as after the triplet. The kick size: θ=2.123 *mrad* .The magnetic field assumed B=1.6 *T*, at the full energy Bρ=833.904

Tm, the magnetic length required is ~1.106 *m*. There are four dipoles per ring – total of eight dipoles.

3 COOLING PERFORMANCE

3.1 RHIC-II parameters

In this chapter we present the physics, simulation and benchmarking of the performance of the RHIC electron cooler. We freely use material prepared for BNL by our collaborators. In particular, by the Dubna group as part of our collaboration on the development of the BETACOOL code [1], by the Tech-X group as part of our collaboration on numerical study of the friction force with the VORPAL [2] code, and by the Fermilab electron cooling group as part of our collaboration on experimental study of the non-magnetized friction force [3].

3.1.1 Expected performance for heavy ions and protons

The present performance of the RHIC collider with heavy ions is limited by the process of Intra-Beam Scattering (IBS). To achieve the required luminosities for the future upgrade of the RHIC complex (known as RHIC-II) an electron cooling system was proposed [4].

The baseline of the heavy-ion program for RHIC is operation with Au ions at total energy per beam of 100 GeV/n. For such an operation, the electron cooling should compensate IBS and provide an increase by about factor of 10 in the average luminosity per store.

For RHIC operations with protons, the electron cooling should assist in obtaining required initial transverse and longitudinal emittances or prevent their significant increase due to IBS. Although, IBS is not as severe for protons as for heavy ions, a proposed increase in proton intensity for RHIC-II upgrade makes IBS one of the dominant effects as well.

Table 3.1.1 Performance for RHIC-II

Gold at 100 GeV/n per beam	**w/o e-cooling**	**With e-cooling**
Emittance (95% norm.) [π μm]	15 → 30 (depending on the length of the store)	15 → 12
β-function in IR [m]	1.0	0.5
Number of bunches	112	112
Bunch population [10^9]	1	1
Peak luminosity [10^{26} cm^2 s^{-1}]	30	90
Average store luminosity [10^{26}]	8	70-80
Protons at 250 GeV	**w/o e-cooling**	**with e-cooling**
Emittance (95% norm.) [π μm]	20 (initial)	12 (initial)
β-function	1.0	0.5
Number of bunches	112	112
Bunch population [10^{11}]	2	2
Average store luminosity [10^{30}]	150	500

RHIC luminosity without cooling:

For present operations with Au ions:

a) There is a significant emittance increase due to IBS which results in the luminosity loss. This is shown, for example, in Fig. 3.1.1 (Run-2004 experimental data).

b) In addition, there is a significant growth of the bunch length which leads to particle loss from the bucket. Also, with such a long bunch length only the central portion of the longitudinal beam distribution can effectively contribute to counts in the detector which results in an additional loss of effective luminosity.

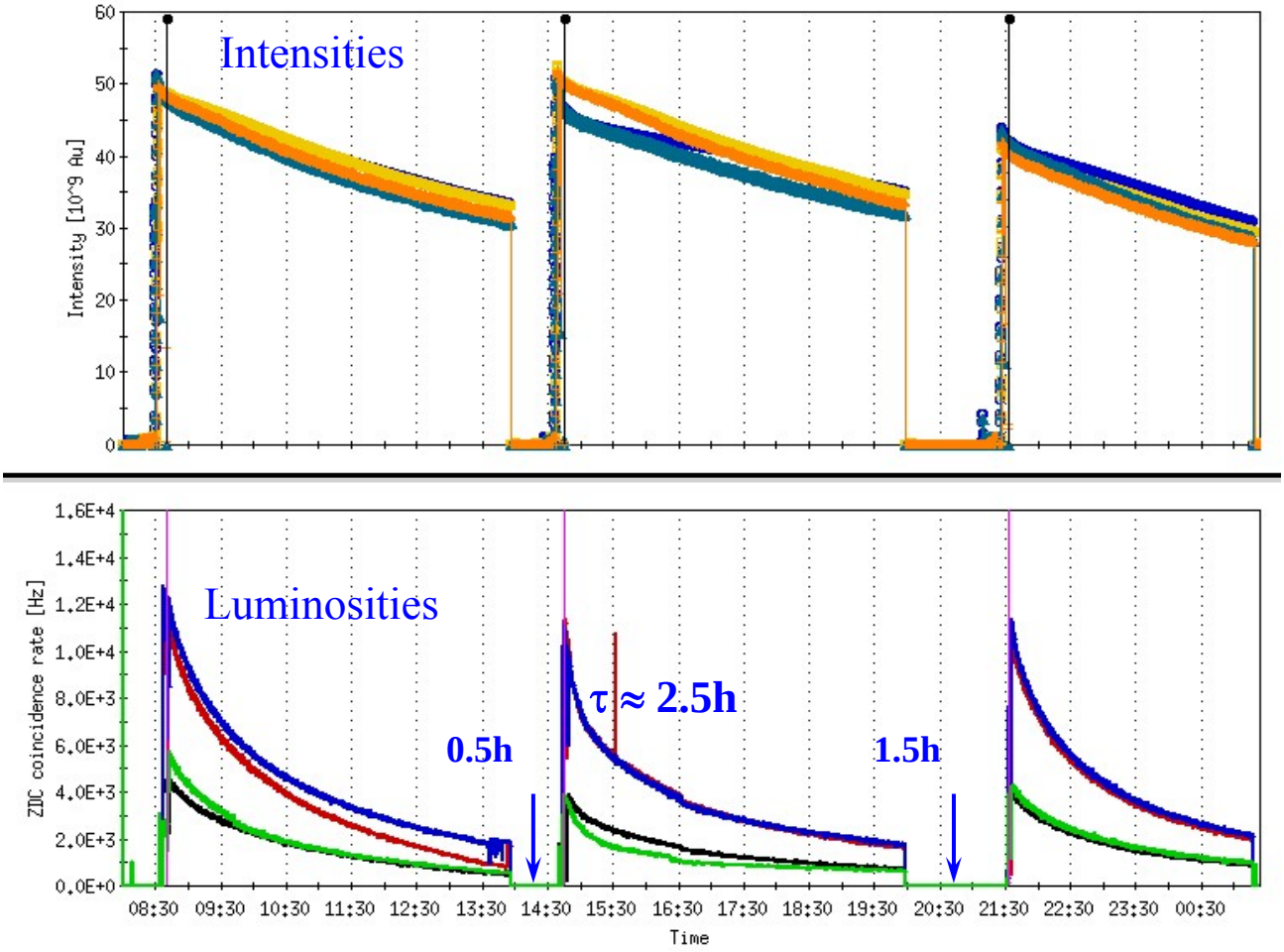

Fig. 3.1.1 Run-2004 experiment with Au ions (40 bunches).

Note that for the enhanced luminosity of RHIC-II without cooling, the optimum length of the store is shorter than for typical RHIC stores, shown in Fig. 3.1.1.

RHIC luminosity with cooling:

Electron cooling of Au ions at the total beam energy of 100 GeV/n can provide about factor of 10 increase in the average store luminosity as compared to the upgraded RHIC without cooling. This will be the final step in a series of improvements, which will bring the average luminosity of RHIC to about factor of 40 larger than the original design value.

Figure 3.1.2 shows the luminosity for RHIC-II parameters (Table 3.1.2) based on the present approach, which calls for non-magnetized cooling. For present RHIC operations without electron cooling, β* (the beta function at the IP) is limited to about one meter (or slightly less), because the emittance is increased by a factor of two due to IBS. Further reduction of β* with such an increase of the emittance would lead to a significant angular spread and beam loss. On the other hand, keeping the rms emittance constant (by cooling), allows one to begin a store cycle with smaller values of β*. This is taken into account in Fig. 3.1.2, where β*=0.5 and 1 m were used with and without electron cooling, respectively.

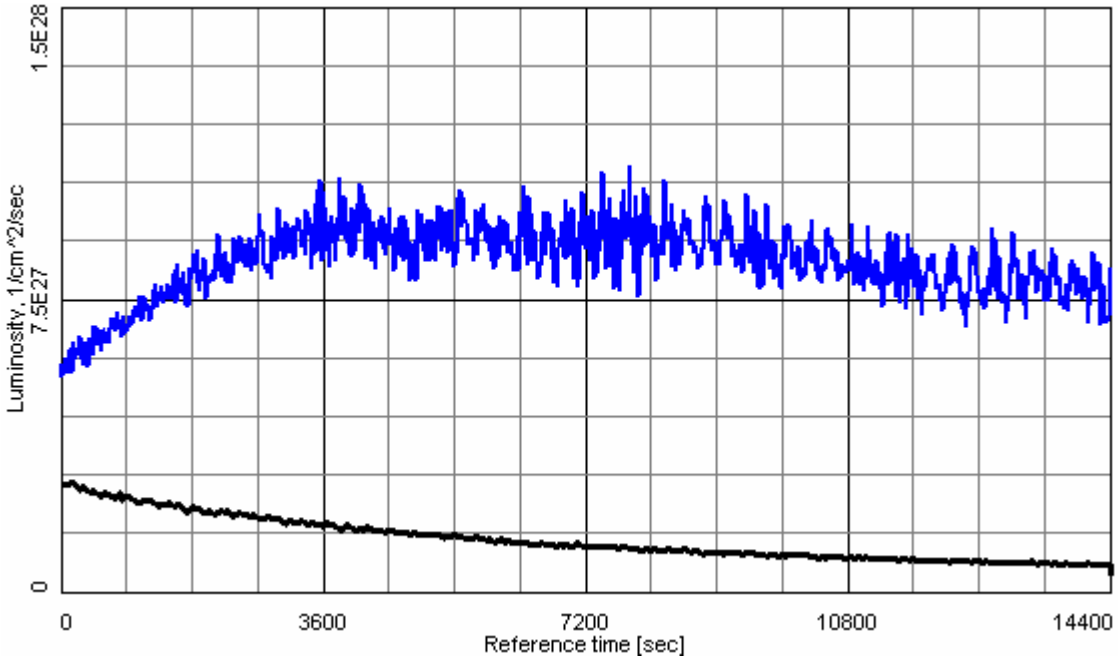

Fig. 3.1.2: Simulated luminosity for the RHIC-II upgrade (with two IP's), with (blue top curve) and without (black bottom curve) electron cooling, taking β*=0.5 m and 1 m, respectively.

The average luminosity with cooling in Fig. 3.1.2 (using parameters in Table 3.1.2) is $<L>=8.5\cdot10^{27}$ [$cm^{2}sec^{-1}$]. This number is a result of simulations based on the "modeled beam" approach in BETACOOL code which simulates detailed evolution of ions distribution. Simulations based on such a detailed dynamics predict larger average luminosity than a more simplified "rms dynamics" approach but the uncertainty of various algorithms and numerical effects becomes larger as well. All this is summarized in Section 3.5.

3.1.2 Non-magnetized vs. magnetized cooling

The traditional electron cooling system employed at a typical low-energy cooler is based on electron beam generated with an electrostatic electron gun in DC operating mode, immersed in a longitudinal magnetic field. The magnetic field is used for the transport of an electron beam through the cooling section from the gun to the collector. The magnetic field value is determined by

condition of electron "magnetization" – radius of the electron Larmor rotation in the transverse plane has to be much less than the beam radius. The presence of a strong longitudinal magnetic field changes the collision kinetics significantly. The magnetic field limits transverse motion of the electrons. In the limit of a very strong magnetic field, the transverse degree of freedom does not take part in the energy exchange, because collisions are adiabatically slow relative to the Larmor oscillations. As a result, the efficiency of electron cooling is determined mainly by the longitudinal velocity spread of the electrons. Such cooling is typically referred to as "magnetized cooling". Magnetized cooling was found to be an extremely useful technique in obtaining high-brightness hadron beams with extremely low longitudinal momentum spread [5].

However, if an rms velocity spread within electron beam is comparable or smaller than the spread within the ion beam and, and there is no requirement of getting ultra-cold ion state, the cooling can be done without the help of the strong external magnetic field. Such type of cooling is referred to as the "non-magnetized cooling"; although a weak external field can be still employed, for example, to ensure focusing and alignment of electron and ion beams.

The first cooling system which is based on the "non-magnetized" approach was successfully constructed at the FNAL Recycler ring. It has been in operation since July 2005. The Recycler's cooling system has by far the highest energy of the electrons presently in operation (4.3 MeV) [3].

Although extensive studies of the magnetized cooling approach for RHIC showed that such approach is feasible [4, 6] and would provide required luminosities for the RHIC-II, the baseline was recently changed to the non-magnetized one.

Electron cooling at RHIC using the non-magnetized electron beam significantly simplifies the cooler design. The generation and acceleration of the electron bunch without longitudinal magnetic field allows us to reach a low value of the emittance for the electron beam in the cooling section. The cooling rate required for suppression of the Intra-Beam Scattering (IBS) can be achieved with a relatively small charge of the electron bunch ~ 5 nC ($3 \cdot 10^{10}$ electrons per bunch).

For cooling of Au ions in RHIC at the beam energy of 100 GeV/n, the kinetic energy of the electron beam has to be 54.3 MeV. Such a high-energy electron cooling system for RHIC is based on the use of an Energy Recovery Linac (ERL) [7].

3.1.3 Parameters of the electron cooler

Table 3.1.2 summarizes the parameters of a typical beam of Au ions at the store energy of 100GeV/n and settings of the proposed RHIC-II cooler.

Table 3.1.2 Ion and electron beam parameters

Ion rms beam emittance normalized [π·mm·mrad]	2.5
Ion rms momentum spread	$5\cdot10^{-4}$
Number of ions per bunch	10^9
Ion beta functions in the cooling section [m]	400
Ion rms beam radius [mm]	3
Ion initial rms bunch length [cm]	20
Circumference of RHIC ring [m]	3833
Electron cooler length [m]	80
Electron rms beam emittance normalized [π·mm·mrad]	4
Electron rms momentum spread	$3\cdot10^{-4}$
Number of electrons per bunch	$3\cdot10^{10}$
Electron rms beam radius [mm]	4.3
Electron rms bunch length [cm]	1
Relativistic factor γ (ions, electrons)	107.35

Table 3.1.3 Ion and electron beam rms velocities (PRF) corresponding to Table 3.1.2:

Ion transverse rms velocity [m/s]	$2.5\cdot10^5$
Ion longitudinal rms velocity [m/s]	$1.5\cdot10^5$
Electron transverse rms velocity [m/s]	$2.8\cdot10^5$
Electron longitudinal rms velocity [m/s]	$9.0\cdot10^4$

3.1.4 Suppression of recombination with undulators

Non-magnetized cooling requires low temperature of the electrons in the cooling section. However, a problem with such an approach may be a high recombination rate for low electron temperature [4].

Presently, suppression of the ion recombination for RHIC is considered for the heaviest ions (such as gold) using an undulator field in the cooling section [8, 9]. In the presence of an undulator field, trajectories of all electrons have the same coherent azimuth angle θ, determined by the undulator period λ and field value B at the axis:

$$\theta = \frac{eB\lambda}{2\pi pc}, \qquad (3.1.1)$$

where p is the electron momentum.

The recombination coefficient, determined via the recombination cross section σ as

$$\alpha_r = \int (V_i - v_e)\sigma(V_i - v_e) f(v_e) d^3 v_e, \qquad (3.1.2)$$

has to be calculated taking into account the coherent transverse electron velocity. Therefore, one can expect sufficient suppression of the recombination without significant loss in the friction force (see Section 3.2.4).

To provide an estimate of undulator efficiency we use the BETACOOL code with calculation of the friction force and recombination rates based on numerical evolution of the integrals over the electron velocity distribution. For an accurate estimate of the loss due to recombination one should take into account that the intensity of the ion beam is decreasing due to beam-beam collisions with disintegration in the IP region. Such disintegration (burn-off) depends on the distribution function of the ion beam which one gets as a result of Intra-beam Scattering (IBS) and cooling. All together, these dynamics processes (IBS, cooling, burn-off, recombination) are included in BETACOOL and provide an estimate of the loss due to the recombination.

3.2 Friction force description

3.2.1 Non-magnetized friction force calculation

In the particle rest frame (PRF) the friction force acting on the ion with a charge number Z passing through an electron beam of density n_e can be accurately evaluated by numerical integration of the following formula [10, 11]:

$$\vec{F} = -\frac{4\pi n_e e^4 Z^2}{m}\int \ln\left(\frac{\rho_{\max}}{\rho_{\min}}\right)\frac{\vec{V}-\vec{v}_e}{\left|\vec{V}-\vec{v}_e\right|^3} f(v_e)d^3v_e, \qquad (3.2.1)$$

where e and m are the electron charge and mass, V and v_e are the ion and electron velocities respectively. The Coulomb logarithm $L_c = \ln\frac{\rho_{\max}}{\rho_{\min}}$ is kept under the integral because the minimal impact parameter depends on electron velocity:

$$\rho_{\min} = \frac{Ze^2}{m}\frac{1}{\left|\vec{V}-\vec{v}_e\right|^2}. \qquad (3.2.2)$$

At a given value of the ion velocity the maximum impact parameter is constant and determined by either the dynamic shielding radius or the ion time of flight through the electron cloud. The radius of the dynamic shielding sphere coincides with the Debye radius

$$\rho_D = \frac{\Delta_e}{\omega_p}, \qquad (3.2.3)$$

when the ion velocity is less than the electron velocity spread Δ_e. The plasma frequency ω_p is equal to

$$\omega_p = \sqrt{\frac{4\pi n_e e^2}{m}}. \qquad (3.2.4)$$

When the ion velocity is larger than the electron velocity spread, the shielding distance is given by:

$$\rho_{sh} = \frac{V}{\omega_p}. \tag{3.2.5}$$

The formulae (3.2.3) and (3.2.5) can be combined together to have a smooth dependence of the shielding radius on the ion velocity:

$$\rho_{sh} = \frac{\sqrt{V^2 + \Delta_e^2}}{\omega_p}. \tag{3.2.6}$$

In the case when the shielding sphere does not contain a large number of electrons to compensate the ion charge (such a situation takes a place, for example, in the case of the magnetized electron beam at low longitudinal velocity spread) it has to be increased in accordance with the electron beam density and the ion charge. In the BETACOOL program such a radius is estimated from the expression

$$n_e \rho^3 \sim 3Z. \tag{3.2.7}$$

As a result, the maximum impact parameter is calculated as a minimum from three values:

$$\rho_{\max} = \min\left\{\max\left(\rho_{sh}, \sqrt[3]{\frac{3Z}{n_e}}\right), V\tau\right\}. \tag{3.2.8}$$

The second term describes the distance, which the ion passes inside the electron beam. Here τ is the ion time of flight through the cooling section in the PRF:

$$\tau = \frac{l_{cool}}{\beta\gamma c}. \tag{3.2.9}$$

In the case of an axial symmetry the electron distribution function can be written in the following form:

$$f(v_e) = \left(\frac{1}{2\pi}\right)^{3/2} \frac{1}{\Delta_\perp^2 \Delta_\parallel} \exp\left(-\frac{v_\perp^2}{2\Delta_\perp^2} - \frac{v_\parallel^2}{2\Delta_\parallel^2}\right), \tag{3.2.10}$$

where $\Delta_\perp$ and $\Delta_\parallel$ are the electron rms velocity spreads in the transverse and longitudinal direction, respectively. The shielding cloud in this case has an ellipsoidal shape which can be approximated by the sphere with the radius, calculated using effective electron velocity spread:

$$\Delta_e^2 = \Delta_\perp^2 + \Delta_\parallel^2. \tag{3.2.11}$$

The components of the friction force (3.2.1) can be evaluated in a cylindrical coordinate system as follows [1]:

$$F_\perp = -\sqrt{\frac{2}{\pi}}\frac{Z^2e^4n_e}{m\Delta_\perp^2\Delta_\parallel}\int_0^\infty\int_{-\infty}^{\infty}\int_0^{2\pi}\ln\left(\frac{\rho_{\max}}{\rho_{\min}}\right)\frac{\left(V_\perp - v_\perp\cos\varphi\right)\exp\left(-\frac{v_\perp^2}{2\Delta_\perp^2}-\frac{v_\parallel^2}{2\Delta_\parallel^2}\right)}{\left(\left(V_\parallel - v_\parallel\right)^2+\left(V_\perp - v_\perp\cos\varphi\right)^2+v_\perp^2\sin^2\varphi\right)^{3/2}}v_\perp d\varphi dv_\parallel dv_\perp,$$

$$F_\parallel = -\sqrt{\frac{2}{\pi}}\frac{Z^2e^4n_e}{m\Delta_\perp^2\Delta_\parallel}\int_0^\infty\int_{-\infty}^{\infty}\int_0^{2\pi}\ln\left(\frac{\rho_{\max}}{\rho_{\min}}\right)\frac{\left(V_\parallel - v_\parallel\right)\exp\left(-\frac{v_\perp^2}{2\Delta_\perp^2}-\frac{v_\parallel^2}{2\Delta_\parallel^2}\right)}{\left(\left(V_\parallel - v_\parallel\right)^2+\left(V_\perp - v_\perp\cos\varphi\right)^2+v_\perp^2\sin^2\varphi\right)^{3/2}}v_\perp d\varphi dv_\parallel dv_\perp. \quad (3.2.12)$$

Within an accuracy of about 2% the upper limit of the integrals over velocity components can be replaced from infinity to three corresponding rms values, and integration over φ can be performed from 0 to π due to symmetry of the formulae. In this case the friction force components can be calculated as (such expressions are used in BETACOOL):

$$F_\perp = -\frac{4\pi Z^2e^4n_e}{m\cdot Int}\int_0^{3\Delta_\perp}\int_{-3\Delta_\parallel}^{3\Delta_\parallel}\int_0^{\pi}\ln\left(\frac{\rho_{\max}}{\rho_{\min}}\right)\frac{\left(V_\perp - v_\perp\cos\varphi\right)\exp\left(-\frac{v_\perp^2}{2\Delta_\perp^2}-\frac{v_\parallel^2}{2\Delta_\parallel^2}\right)}{\left(\left(V_\parallel - v_\parallel\right)^2+\left(V_\perp - v_\perp\cos\varphi\right)^2+v_\perp^2\sin^2\varphi\right)^{3/2}}v_\perp d\varphi dv_\parallel dv_\perp,$$

$$F_\parallel = -\frac{4\pi Z^2e^4n_e}{m\cdot Int}\int_0^{3\Delta_\perp}\int_{-3\Delta_\parallel}^{3\Delta_\parallel}\int_0^{\pi}\ln\left(\frac{\rho_{\max}}{\rho_{\min}}\right)\frac{\left(V_\parallel - v_\parallel\right)\exp\left(-\frac{v_\perp^2}{2\Delta_\perp^2}-\frac{v_\parallel^2}{2\Delta_\parallel^2}\right)}{\left(\left(V_\parallel - v_\parallel\right)^2+\left(V_\perp - v_\perp\cos\varphi\right)^2+v_\perp^2\sin^2\varphi\right)^{3/2}}v_\perp d\varphi dv_\parallel dv_\perp, \quad (3.2.13)$$

where the normalization factor is calculated in accordance with:

$$Int = \int_0^{3\Delta_\perp}\int_{-3\Delta_\parallel}^{3\Delta_\parallel}\int_0^{\pi}\exp\left(-\frac{v_\perp^2}{2\Delta_\perp^2}-\frac{v_\parallel^2}{2\Delta_\parallel^2}\right)v_\perp d\varphi dv_\parallel dv_\perp. \quad (3.2.14)$$

The minimal impact parameter is the following function of the electron velocity components:

$$\rho_{\min} = \frac{Ze^2}{m_e}\frac{1}{\left(V_\parallel - v_\parallel\right)^2+\left(V_\perp - v_\perp\cos\varphi\right)^2+v_\perp^2\sin^2\varphi}. \quad (3.2.15)$$

When the Coulomb logarithm L_C is constant the two of the three integrals in Eq. (3.2.12) can be performed analytically and the friction force components can be written in accordance with Binney's formulae [12]. Such an algorithm significantly speeds up numerical evaluation of the friction force and is also included in the BETACOOL code.

3.2.2 Comparison with direct numeric simulation

The first step towards accurate calculation of cooling times is to use an accurate description of the cooling force. As for the previous case of the magnetized cooling, the VORPAL code [2] is being used to simulate from first principles the non-magnetized friction force and diffusion coefficients for the parameters of the RHIC cooler. For simulation of electron cooling problem, VORPAL uses molecular dynamics techniques and explicitly resolves close binary collisions to obtain the friction force and diffusion coefficient with a minimum of physical assumptions [13].

The latest version of the BETACOOL code [1] includes numerical integration over the electron velocity distribution. This numerical evaluation of the force enables an accurate comparison with the VORPAL results, both for the magnetized and non-magnetized friction force with an anisotropic velocity distribution of the electrons. The results of such benchmarking are summarized in [14, 15].

For example, Fig. 3.2.1 compares VORPAL data (dots with error bars) with the result of numerical integration based on Eq. (3.2.1) (solid red line), for the case of an anisotropic Maxwellian velocity distribution of the electrons given in Eq. (3.2.10), where $\Delta_{\perp}=4.2\cdot10^{5}$ [m/s] and $\Delta_{\parallel}=1.0\cdot10^{5}$ [m/s] ($Z=79$, $n_e=2\cdot10^{15}$ m^{-3}).

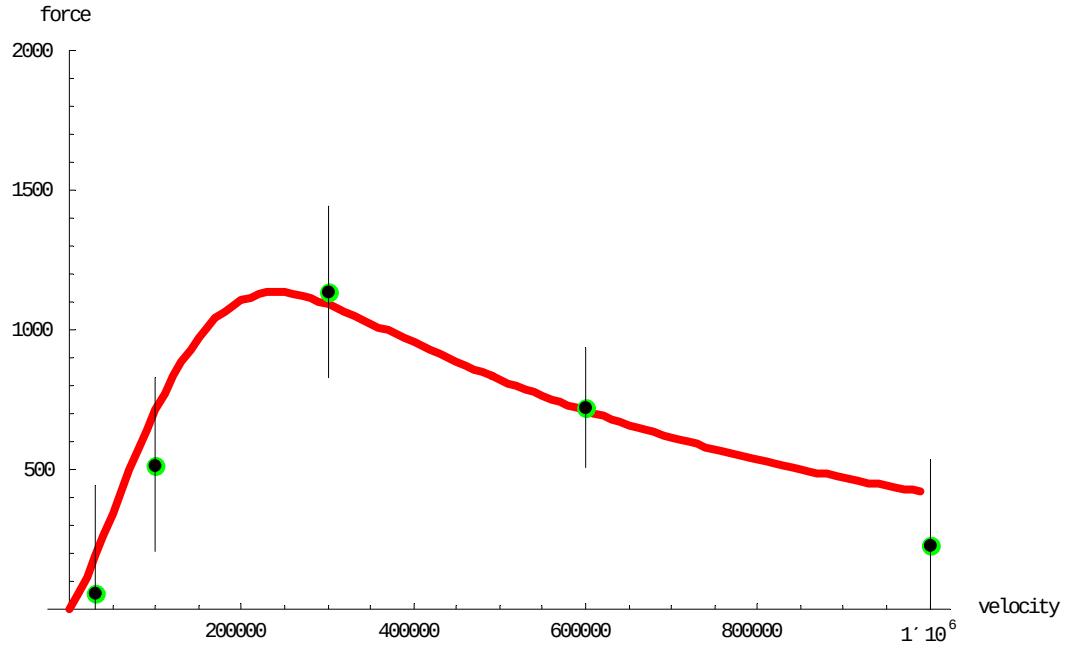

Fig. 3.2.1. Non-magnetized friction force for an anisotropic electron velocity distribution. Force [eV/m] vs. ion velocity [m/s]: solid line (red) – numeric integration using BETACOOL; points with errors bar (3 rms deviation shown)– simulations using VORPAL.

Simulations were done for other degrees of anisotropy of the electron velocity as well. We find the agreement between VORPAL simulations and numeric integration satisfactory, and thus use the non-magnetized friction force in BETACOOL (based on numerical evaluation of the integrals) in our simulations of the non-magnetized cooling.

3.2.3 Comparison with experimental data

In a typical low-energy electron cooling system, a strong longitudinal magnetic field is used for transporting the electron beam. For decreased values of the magnetic field in the cooling section the beam quality is diminished and investigation of the non-magnetized regime of the electron cooling can not be provided with a well controlled conditions.

In July 2005 the Recycler cooling system was put into operation in Fermilab [3]. In the Recycler's cooling system the longitudinal magnetic field in the cooling section is used only to preserve the angular spread of the electrons θ at the level below 200 μrad. The required longitudinal magnetic field value B is about 105 G that corresponds to electron rotation with Larmor radius

$$\rho_{\perp} = \frac{pc}{eB}\theta \approx 2.3 \cdot 10^{-4} m ,$$

where pc = 4.85 MeV is the electron momentum. The cooling section length is l_{cool}=20 m which approximately corresponds to 2 periods of the Larmor helix. A maximum impact parameter for the maximum electron current of 500 mA is restricted by a time of flight through the cooling section and it is equal

$$\rho_{\max} = \frac{l_{cool}}{\beta\gamma c} \approx 1.3 \cdot 10^{-3} m$$

With such parameters the contribution to the friction force is dominated by the non-magnetized collisions, which allows to refer to the cooling in Recycler as "non-magnetized".

To provide a comparison between the results of the experimental studies at Recycler (FNAL) and the numerical simulation with the BETACOOL program, several new algorithms were implemented in the code. A general method for the friction force measurements at the Recycler is the "Voltage Step" method. Such a procedure was also implemented in BETACOOL.

One of the features of the Recycler cooling system is a strong dependence of the electron transverse velocity spread on the distance from the beam centre. This effect appears due to the beam envelope mismatch with the transport channel, and is called "envelope scalloping". In the first approximation this effect can be presented as a linear increase of the velocity spread with radial co-ordinate:

$$\Delta_{\perp} = \frac{d\Delta_{\perp}}{dr} r , \qquad (3.2.16)$$

where the velocity gradient $\frac{d\Delta_{\perp}}{dr}$ is an additional input parameter available in BETACOOL simulations.

An example of simulations of the cooling (using BETACOOL) is presented in the Fig. 3.2.2. The red curve corresponds to an average momentum of the antiprotons. The first 1700 sec correspond to pre-cooling of the antiprotons. At t=1700 sec, the electron momentum was step-shifted by a relative value of 10^{-3} and during the next 2000 sec the average antiproton momentum is cooled to the new momentum of the electrons. This is the essence of the Voltage Step method. The green curve presents the variation in time of the antiproton momentum spread.

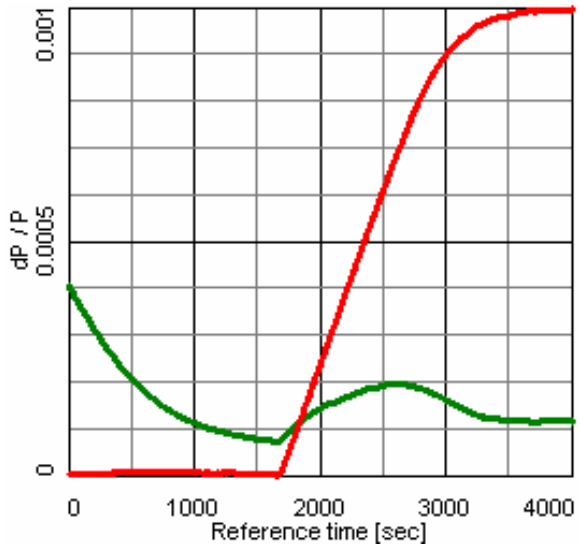

Fig. 3.2.2 Simulation of the voltage step method using BETACOOL program, for the parameters shown in Table 3.2.1.

Table 3.2.1 The Recycler cooling system parameters used in simulations.

Cooling section length, m	20
Electron energy, MeV	4.36
Beta functions in the cooling section, m	20
Electron current, A	0.2
Electron beam radius, cm	0.45
Transverse temperature (PRF), eV	0.5
Longitudinal temperature (PRF), eV	0.01

Evolution of the antiproton momentum during the friction force measurement, as a 3D plot of the profile versus time, is shown in Fig 3.2.3.

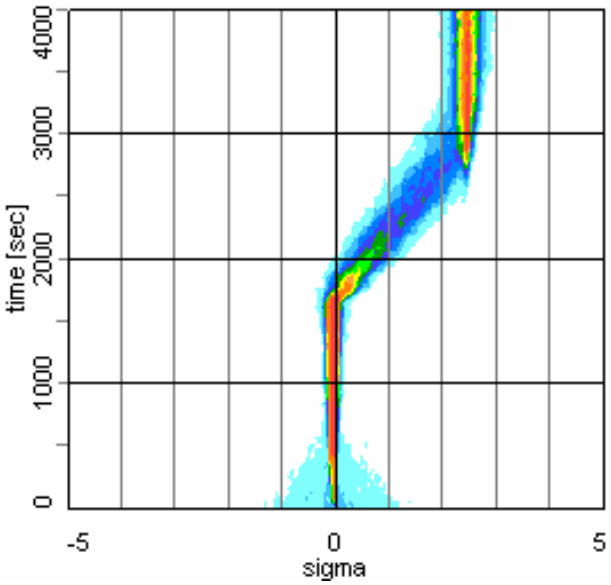

Fig. 3.2.3 The longitudinal profile evolution during friction force measurement.

To reproduce the procedure used in Fermilab for the beam longitudinal distribution measurement the possibility to average over a few consequent longitudinal profiles was also introduced. An example of a few consequent averaged profiles calculated with BETACOOL after 2 keV step of the electron energy is presented in the Fig. 3.2.4. The electron beam current is 500 mA. Figure 3.2.5 shows measured profiles for the same parameters.

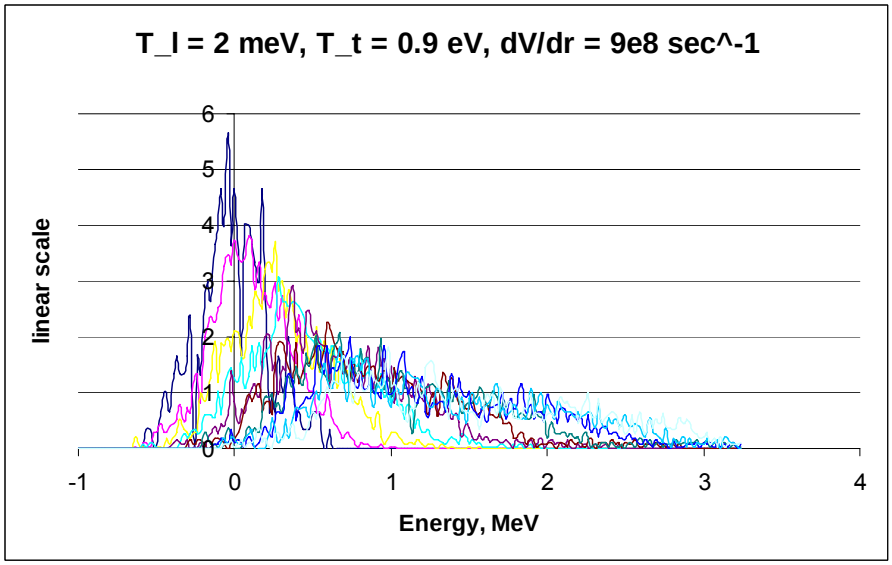

Fig. 3.2.4 Simulations (A. Sidorin, JINR). Evolution of the longitudinal profile in time. Distance between slices is 50 sec.

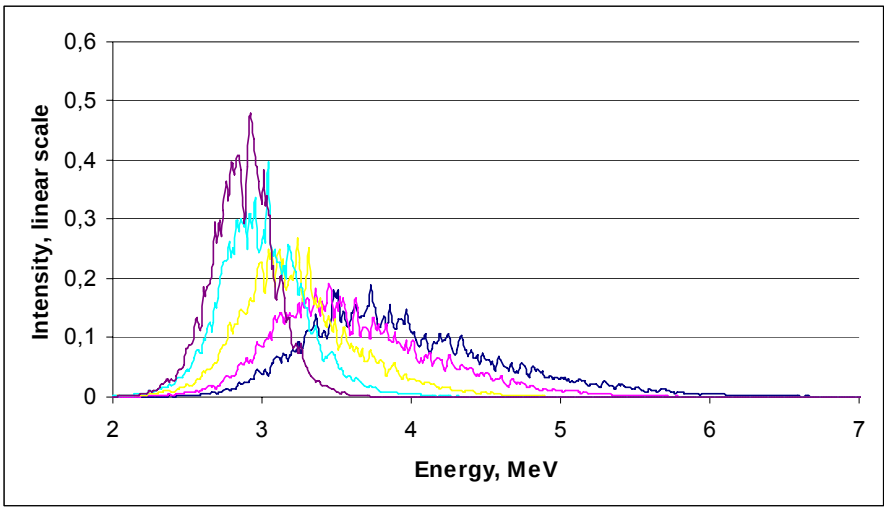

Fig. 3.2.5 Measurements (L. Prost, FNAL). Evolution of the longitudinal profile in time.

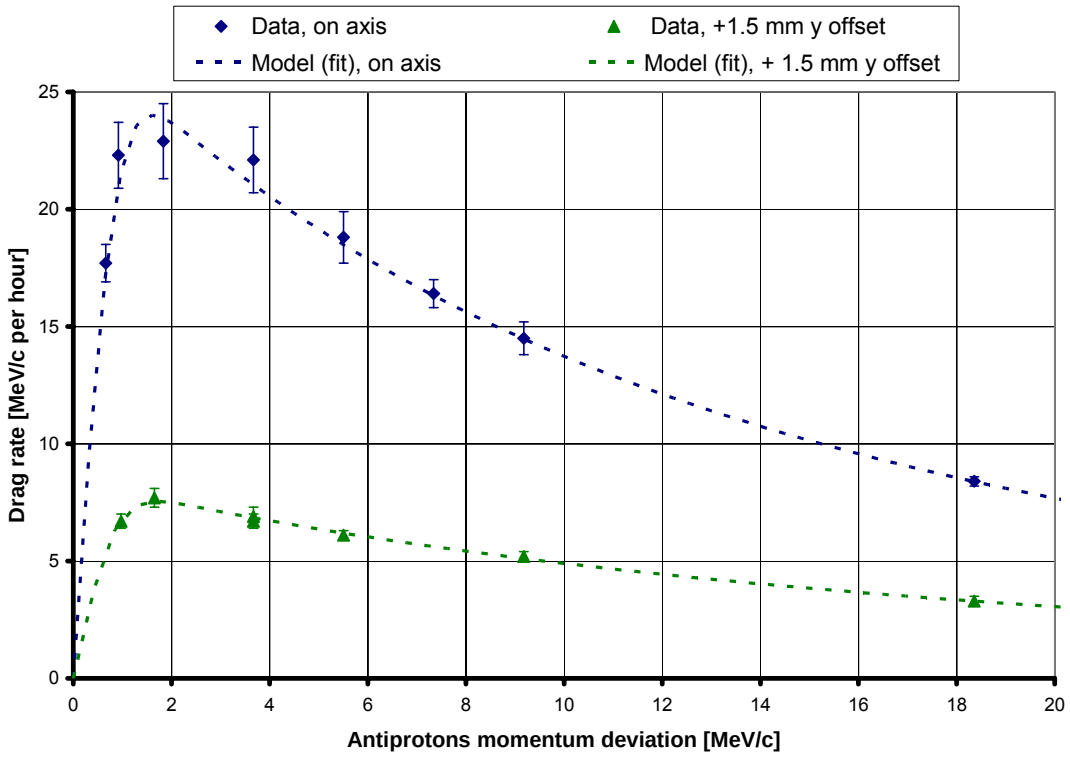

Fig. 3.2.6 (Courtesy of L. Prost, A. Shemyakin, FNAL). Measurements vs theoretical model.

Analysis of the experimental data and comparison with theory is being done in collaboration with the electron cooling groups of Fermilab (S. Nagaitsev, L. Prost, A. Shemyakin, A. Burov) and JINR (A. Sidorin and A. Smirnov).

Presently, the agreement between the theory and experiments is considered to be pretty good [16]. The remaining uncertainty is attributed to the assumptions about the electron beam characteristics. More details on the results of benchmarking can be obtained from the Fermilab group.

3.2.4 Friction force in the presence of an undulator field

Suppression of heavy ion recombination for RHIC is based on the use of an undulator field in the cooling section [8, 9]. In the presence of an undulator field, the trajectories of all the electrons have the same coherent azimuthal angle θ, determined by the undulator period λ and field value B at the axis:

$$\theta = \frac{eB\lambda}{2\pi pc}, \qquad (3.2.17)$$

where p is the electron momentum. Since the recombination cross section is approximately inversely proportional to the electron energy in the ion rest frame, the ion beam life time can be sufficiently improved.

One can expect that at impact parameters significantly larger than the electron rotation radius, the

$$r_0 = \frac{\theta\lambda}{2\pi} = \frac{eB\lambda^2}{4\pi^2 pc} \tag{3.2.18}$$

kinematics of the binary collisions will be similar to Rutherford scattering of a free electron. In this case the friction force acting on the ion inside the electron beam with the velocity distribution function $f(v_e)$ can be still calculated with the usual formula:

$$\vec{F} = -\frac{4\pi n_e e^4 Z^2}{m} \int L_c \frac{\vec{V}_i - \vec{v}_e}{\left|\vec{V}_i - \vec{v}_e\right|^3} f(v_e) d^3 v_e , \tag{3.2.19}$$

where n_e is electron density in the Particle Rest Frame (PRF), v_e, V_i are the electron and ion velocity, L_c– Coulomb logarithm:

$$L_c = \ln \frac{\rho_{\max}}{\rho_{\min}} . \tag{3.2.20}$$

For the RHIC parameters, the maximum impact parameter is determined by the time of flight of the ion through the cooling section and it is not affected by the undulator field. However, the minimum impact parameter ρ_{min} which is determined by a relative velocity between an ion and electron as

$$\rho_{\min} = \frac{Ze^2}{m_e} \frac{1}{\left|\vec{V}_i - \vec{v}_e\right|^2} , \tag{3.2.21}$$

has to be replaced by r_0 value, in the presence of the undulator field. Therefore, the friction force is expected to be reduced by the factor of the order of $\ln \frac{\rho_{\max}}{\rho_{\min}} / \ln \frac{\rho_{\max}}{r_0}$.

To make sure that such a representation of the friction force in the presence of an undulator field is accurate, an undulator field was implemented in the VORPAL code, and numerical simulations were performed (G. Bell et al.) [17] for different strength of the magnetic field B and pitch period λ.

An example of such a comparison between VORPAL simulations (dots with error bars) and numeric integration with the BETACOOL (lines) is shown in Figs. 3.2.7-8, for an rms ion velocity of $3.0 \cdot 10^5$ [m/s] in PRF and the following parameters in simulations ($\Delta_\perp = 3.0 \cdot 10^5$ [m/s] and $\Delta_\parallel = 3.0 \cdot 10^5$ [m/s], τ=0.9 nsec, Z=79, $n_e = 7.32 \cdot 10^{13}$ m^{-3}).

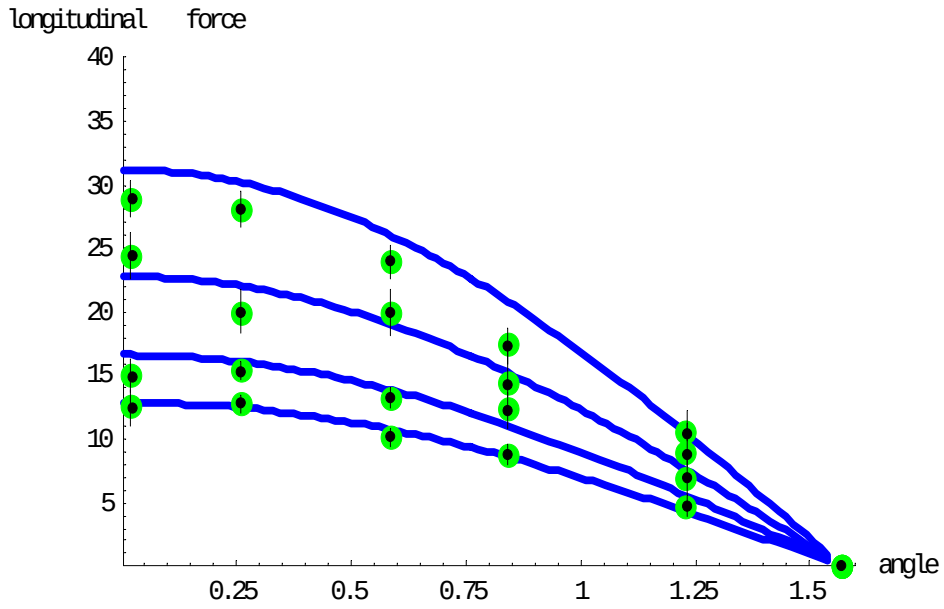

Fig. 3.2.7 Longitudinal component of the friction force at an rms ion velocity of $3.0 \cdot 10^5$ m/s for B=0 (upper curve) and for an undulator with different periods λ=8, 16, 24 cm (B=10G). VORPAL – dots with error bars; BETACOOL numerical integration –lines.

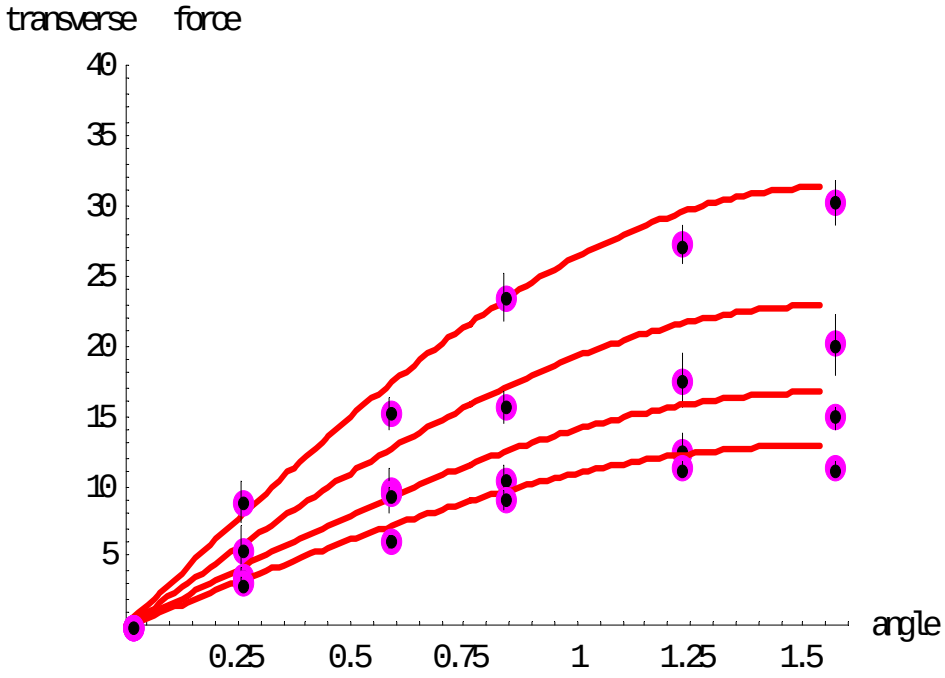

Fig. 3.2.8 Transverse component of the friction force at an rms ion velocity of $3.0 \cdot 10^5$ m/s for B=0 (upper curve) and for an undulator with different periods λ=8, 16, 24 cm (B=10G). VORPAL – dots with error bars; BETACOOL numerical integration – lines.

In all cases, it was found that the friction force scales as predicted by a modified logarithm $\ln \frac{\rho_{\max}}{r_0}$.

Impact of undulator fields was further investigated by including errors in the alignment of individual sections of the undulator. Even with relatively high offsets of 3mm no significant effect on the friction was observed. The study of the effects of errors on the friction force is continuing.

Figure 3.2.9 shows that the force with a random offset between individual undulator sections of 3 mm is the same as the force without misalignments. Simulations in the figure are done for the present baseline parameters of the electron beam and undulator, and observed reduction in the force values in the presence of undulator field is as expected. With such a reduction in the force values, the recombination rates can be suppressed by an order of magnitude.

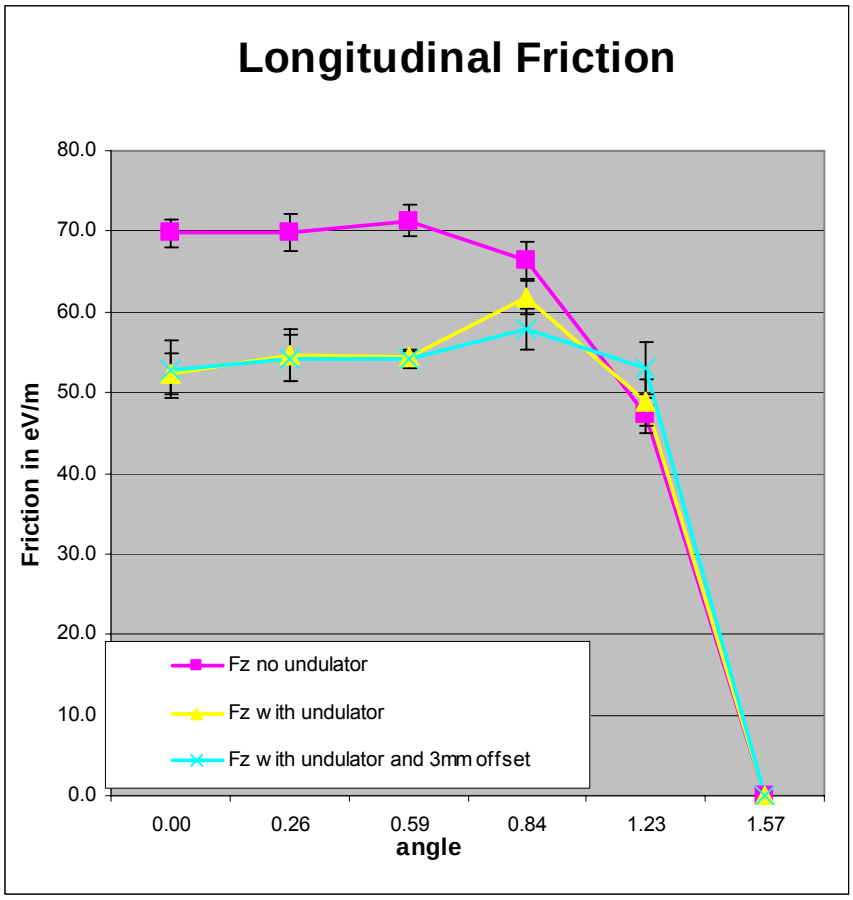

Fig. 3.2.9 (Courtesy of G. Bell, Tech-X Corp.) VORPAL simulations: Longitudinal component of the friction force [eV/m] vs angle [rad] of velocity vector with respect to the longitudinal axis. The plot is done for the amplitude of ion velocity vector of $3.0 \cdot 10^5$ m/s for an undulator with period λ=8 cm (B=10G).

An extensive simulation is presently underway at Tech-X Corp. to study various types of errors in magnetic fields of the undulator, and their impact on the friction force. These studies will help to clarify tolerances for undulator design and construction.

3.3 Intrabeam scattering

Charged particle beam are stored in circular accelerators for a long time. The phenomenon when particles within the beam are scattered from one another via Coulomb scattering is called Intra-Beam Scattering (IBS). Such a process is typically separated in two effects:

1. Scattering on a large angle so that the particles can be lost from a bunch as a result of a single collision – such an effect is called the Touschek effect.

2. Scattering on small angles can randomly add together which can cause beam dimension to grow – such effect is called the Intra-Beam Scattering.

3.3.1 General models

The process of IBS is very similar to collisions in a plasma (ionized gas), which govern gas relaxation towards equilibrium. The corresponding simple diffusion coefficients can be derived. The case of a charged particle beam is in fact very similar to the plasma case when the longitudinal motion is transformed away by going into the Particle-Rest-Frame (PRF) which moves along the storage ring at the nominal beam velocity. The scattering events now appear exactly as in the plasma case; the only difference is that the distribution function is now given in terms of generalized coordinates which describe particle motions in circular accelerator. In circular accelerator, curvature of the orbit produces dispersion, and due to the dispersion a sudden change in energy results in a change of betatron amplitudes. Such a coupling makes an important difference between small-angle Coulomb collisions in plasma (Gas-Relaxation) and in circular accelerators (IBS).

A theory of IBS for protons beams was proposed by Piwinski [18], who calculated the beam growth rates in all three dimensions. In the original theory, growth rates were estimated as an average around the circumference of the ring. For this purpose, the ring lattice functions were also averaged. This model was later extended by a CERN team in collaboration with Piwinski to include variations of the lattice function around the ring. An improved model was later described in a detailed report by Martini [19] and is sometimes referred to as Martini's model. Similar results were also obtained with a completely different approach of S-matrix formalism by Bjorken and Mtingwa [20].

For RHIC parameters, results using both Martini's and Bjorken-Mtingwa's models were found to be in a very good agreement with one another. For our numerical studies of electron cooling presented in this report the Martini's model was used without any approximation. We also used an exact designed lattice of RHIC which includes the derivatives of the lattice functions and insertions in the straight sections for the IP's.

The standard IBS theories were developed in the assumption of uncoupled betatron motion. A more general treatment for the coupled motion was also developed by Piwinski [18] and recently by Lebedev [21]. The standard RHIC operation corresponds to the working point in the vicinity of the coupling resonance with the fully coupled motion. In such a case, the standard treatment of IBS can be used with the horizontal growth rate equally shared between the horizontal and vertical motion –

such an assumption was found to be in good agreement with experimental measurements and is presently used in simulations.

3.3.2 IBS in RHIC: experiments vs. theory

Since the main goal of electron cooling is to overcome emittance growth due to IBS, it was extremely important to make sure that the models of IBS which are being used in cooling simulations are in a good agreement with experimentally measured growth rates.

Several dedicated IBS experiments were performed in 2004 with Au and in 2005 with Cu ions with an intention to increase the accuracy and parameter range of a previous measurements [22]. To ensure an accurate benchmarking of the IBS models, bunches of various intensity and emittance were injected, and growth rates of both the horizontal and vertical emittance and the bunch length were recorded with the Ionization Profile Monitor (IPM) and the Wall Current Monitor (WCM), respectively. Other effects which may obscure comparison, like beam-beam collisions, were switched off. Experiments were done with the RF harmonic h=360 allowing growth of the longitudinal profile without any loss from the bucket.

Although, agreement for the longitudinal growth rate was very good for the 2004 measurements with the Au ions, agreement for the transverse emittance was not that perfect [23]. In fact, the measured transverse emittance growth was larger than the one predicted by simulation using Martini's model of IBS with the exact designed RHIC lattice. As a result of the 2004 studies, a fudge factor was introduced for the transverse growth rate of IBS to make sure that we do not underestimate IBS growth rate for the cooling simulations. Subsequent cooling simulations were done to compensate for such an "enhanced" IBS.

Following the 2004 measurements several studies were done trying to understand a possible source of the disagreement, including IBS growth for the lattice with different average dispersion functions, FODO approximation for the lattice vs. realistic RHIC lattice with straight-section insertions, dispersion mismatch and others [24]. As a result of these studies, it was decided to repeat the measurements with the Cu ions in 2005.

The latest data for IBS with Cu ions showed very good agreement between the measurements and Martini's model of IBS for designed RHIC lattice without any approximation or previously used fudge factors [25]. Below, few examples from these studies are shown in Figs. 3.3.1-3.

Figure 3.3.1 shows growth of the horizontal and vertical emittance in bucket # 100 with the bunch intensity $2.9 \cdot 10^9$.

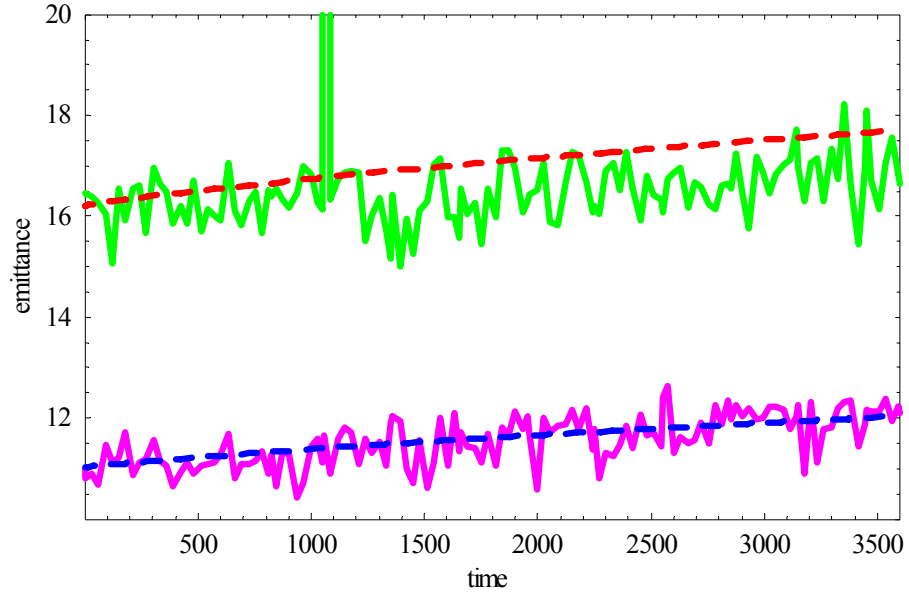

Fig. 3.3.1 Horizontal (upper curve) and vertical 95% normalized emittance [mm mrad] vs time [sec] for bunch intensity $2.9 \cdot 10^9$ Cu ions. Measured emittance: green (horizontal), pink (vertical). BETACOOL simulation using Martini's model: red dash line (horizontal), blue dash line (vertical).

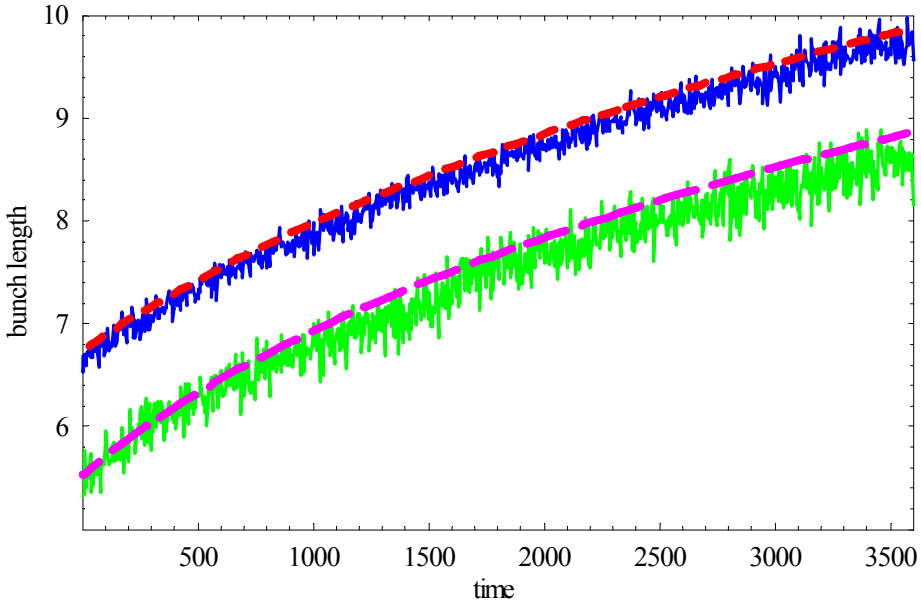

Fig. 3.3.2 Growth of FWHM bunch length [ns] vs time [sec] for two bunch intensities: $2.9 \cdot 10^9$ (upper curve) and $1.4 \cdot 10^9$ (lower curve) Cu ions.

The measured growth rates scale correctly with the bunch intensity and the value of the initial emittance, as shown for the two intensities in Fig. 3.3.2 and Fig. 3.3.3 for the bunch length and horizontal emittance, respectively.

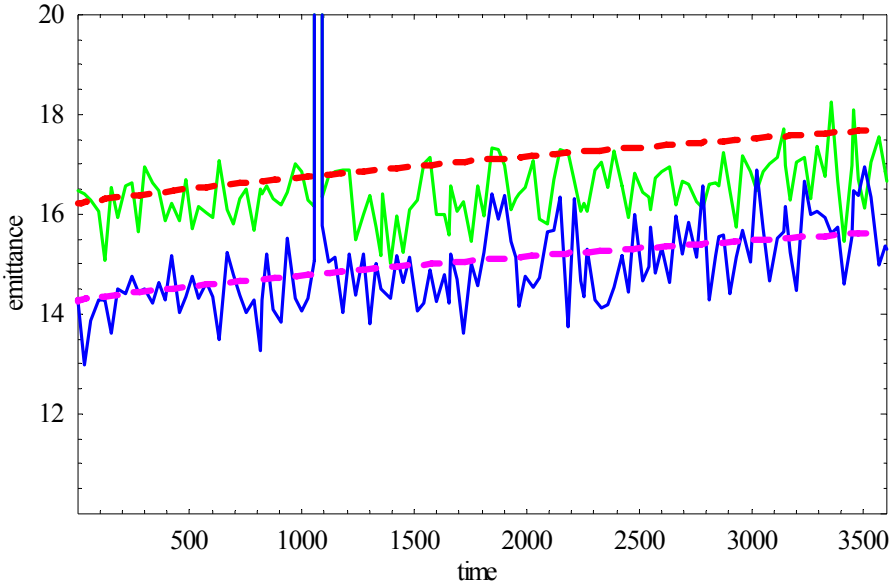

Fig. 3.3.3 Horizontal 95% normalized emittance [μm] for two bunch intensities: $2.9 \cdot 10^9$ (upper curve) and $1.4 \cdot 10^9$ (lower curve) Cu ions.

More details about comparison of IBS measurements in RHIC with the models can be found in [25].

3.3.3 IBS for ion beam distribution under electron cooling

Standard models of IBS discussed above are based on the growth rates of the rms beam parameters for the Gaussian distribution. However, as a result of electron cooling, the core of beam distribution is cooled much faster than the tails. For previous parameters of the magnetized cooling it was found that a simple use of standard rms-based IBS approach would significantly underestimate IBS for beam core. A detailed analytic treatment of IBS, which depends on individual particle amplitude was proposed by Burov [26], with an analytic formulation done for a "flattened" Gaussian distribution. Also, a simplified "core-tail" model, based on a different diffusion coefficients for beam core and tails was also proposed [27]. In addition, the standard IBS theory was reformulated for the rms growth rates of a bi-Gaussian distribution by Parzen [28].

The above formulations, which attempt to calculate IBS for a beam distribution changing under electron cooling, were implemented in BETACOOL [1] and were used for cooling studies of RHIC [27]. The difference between various models and resulting integrated luminosity was found to be substantial for the previous approach of the magnetized cooling where a formation of a distribution with a sharp core was observed.

For the present parameters of the non-magnetized cooling, the formation of such a bi-Gaussian distribution is less pronounced than before for the case of the magnetized cooling. As a result, a deviation between various models and the difference in the integrated luminosity being predicted is expected to be less crucial, although it is probably the largest source of uncertainty in present simulations with the "Modeled Beam" approach. More detailed algorithms for the IBS are presently being developed to reduce remaining uncertainty.

3.4 Recombination

3.4.1 Numerical algorithm

Ion beam life time due to recombination

The ion beam life time due to recombination in the cooling section is calculated via recombination coefficient α_r by the following formula:

$$\frac{1}{N}\frac{dN}{dt} = -\frac{\alpha_r n_e}{\gamma^2}\frac{l_{cool}}{C}, \tag{3.4.1}$$

Here C is the ring circumference. Under assumption that ion velocity in PRF is substantially less than the one of the electrons, recombination coefficient α_r is calculated in PRF by averaging of the recombination cross section over electron distribution function:

$$\alpha_r = \langle v\sigma(v)\rangle \tag{3.4.2}$$

The recombination cross section can be calculated with good accuracy using the following formula:

$$\sigma = A\left(\frac{h\nu_0}{E}\right)\left(\ln\sqrt{\frac{h\nu_0}{E}} + 0.1402 + 0.525\left(\frac{E}{h\nu_0}\right)^{1/3}\right), \tag{3.4.3}$$

where $A = 2^4 3^{-3/2} he^2/\left(m_e^3 c^2\right) = 2.11\times10^{-22}$ cm^2, $h\nu_0 = 13.6\cdot Z^2$ eV is the ion ground state binding energy, and $E = \frac{m_e v_e^2}{2}$ is the kinetic energy of the electrons. In the presence of the undulator field the kinetic energy needs to be calculated as:

$$E = \frac{m}{2}\left(\left(v_\perp + v_{und}\right)^2 + v_\parallel^2\right), \tag{3.4.4}$$

The formula (3.4.2) can be rewritten in the form adopted for numerical integration:

$$\alpha_r = \frac{1}{Int}\int_0^{3\Delta_\perp}\int_{-3\Delta_\parallel}^{3\Delta_\parallel}\sigma(E)\sqrt{\left(v_\perp + v_{und}\right)^2 + v_\parallel^2}\exp\left(-\frac{\left(v_\perp + v_{und}\right)^2}{2\Delta_\perp^2} - \frac{v_\parallel^2}{2\Delta_\parallel^2}\right)v_\perp dv_\parallel dv_\perp . \tag{3.4.5}$$

The normalization factor is calculated as:

$$Int = \int_0^{3\Delta_\perp}\int_{-3\Delta_\parallel}^{3\Delta_\parallel}\exp\left(-\frac{\left(v_\perp + v_{und}\right)^2}{2\Delta_\perp^2} - \frac{v_\parallel^2}{2\Delta_\parallel^2}\right)v_\perp dv_\parallel dv_\perp . \tag{3.4.6}$$

Here

$$\Delta_e = \sqrt{\Delta_\perp^2 + \Delta_\parallel^2} \qquad (3.4.7)$$

is an rms electron velocity spread, with the electron beam temperature being different for the transverse and longitudinal degrees of freedom. The expression in Eq. (3.4.5) is being used in BETACOOL to calculate recombination rate for RHIC.

3.4.2 Experimental measurements and theory.

Radiative recombination of ions was extensively studied experimentally. Perfect agreement between measurements and theoretical prediction for the recombination coefficient was found in a wide range of relative energies between the electrons and ions (>10meV). However, in the region of extremely small relative energies (which is the region typically used for electron cooling), the measured recombination coefficient for experiments with bare ion was found significantly higher than predicted by standard theory of radiative recombination (for ions which are not fully stripped there is an additional channel, dielectronic recombination, which is not relevant for the fully stripped ions in RHIC and thus not discussed here).

The surprising discrepancy between widely recognized theory and measurements resulted in variety of theoretical studies which attempted to address this issue. They range from the influence of three body recombination and density enhancement due to plasma screening effects to the effects of magnetic field on the cross section. However, none of the proposed models was able to account quantitatively for the measured enhancement of recombination coefficients until recently [29].

In the newly proposed model [29], the merging of electron and ion beam results in bound states which, in combination with the radiative stabilization due to a strong magnetic field in a cooling solenoid (typical set-up in low-energy coolers), yield a substantial population of low-lying states in the recombined system. The magnitude of the resulting recombination rates in simulations agreed with measurements very well. Scaling with the ion charge Z and strength of the magnetic field B also agreed with measurements.

In this latest theoretical model [29], which explains the enhancement in the recombination observed, the presence of strong magnetic field in the cooling section is important in radiative stabilization process. This mechanism is not expected to occur in the absence of the solenoidal magnetic field. In addition, in the case of RHIC cooling, the presence of undulator field increases the relative energy to about 30 eV. The agreement between theoretical and experimental recombination coefficient at such high relative energies is very good [30].

3.4.3 Parameters of the undulator

Table 3.4.1 Parameters of the undulator

Magnetic field [G]	10
Period [cm]	8
Introduced effective temperature Teff [eV]	30
Recombination lifetime with Teff [hours]	166

3.5 Detailed calculation of the cooling dynamics

3.5.1 Baseline simulation parameters

Table 3.5.1 Simulation parameters

Electron kinetic energy [MeV]	54.34
Number of electrons per bunch	$3 \cdot 10^{10}$
Electron charge per bunch [nC]	5
Ion beta functions in the cooling section [m]	400
Ion rms beam radius [mm]	3
Ion initial rms bunch length [cm]	20
Circumference of RHIC ring [m]	3833
Electron cooler length [m]	80
Rms electron beam emittance normalized [π·mm·mrad]	4
Electron rms momentum spread	$3 \cdot 10^{-4}$
Ion initial rms momentum spread	$5 \cdot 10^{-4}$
Transverse rms radius of electron beam [mm]	4.3
Electron rms bunch length [cm]	1
Relativistic factor γ (ions, electrons)	107.35
Rms angular spread of ions in cooling section [μrad]	7.6
Transverse rms angular spread of electrons [μrad]	8.7

3.5.2 Detailed evolution of beam distribution

A quick estimate of the cooler performance can be done using an approach with a dynamical tracking of the rms beam parameters. This approach was found to be too inaccurate for previous design with the magnetized cooling for RHIC when a detailed treatment of the beam distribution was found to be extremely important. For the case of a fast cooling in typical low-energy coolers where the whole Gaussian beam is quickly cooled to an approximately Gaussian beam with much smaller rms parameters, a simple approach based on an rms dynamics provides reasonably accurate estimates. For the present parameters of the RHIC cooler based on the non-magnetized approach most of the particles within few sigmas are also effectively cooled, making an rms dynamics approach a reasonable estimate as well.

A more accurate treatment is to use a numerical approach which allows one to track evolution of the beam distribution. Such an approach requires accurate calculation of many effects from a real distribution, including loss on recombination, burn-off process, IBS and calculation of the luminosity from the local charge density. All these algorithms are implemented in BETACOOL and

are being used under the "Modeled beam" approach (which is sometimes is referred to as "detailed" approach since it is based on details of the distribution).

However, each of these effects contributes to the uncertainty (numerical effects and accuracy of the models being used) in the simulations. The effect which results in the largest uncertainty (due to an approximate model) is the treatment of IBS for non-Gaussian distribution. Presently, depending on the model being used, the final result of average luminosity prediction can be different by as much as 20-30%. To remove this largest source of uncertainty new numerical algorithms are being developed within the BETACOOL to describe IBS for an arbitrary distribution more accurately.

Figures 3.5.1-2 show evolution of the horizontal (red), vertical (blue) and longitudinal (green) beam profiles after 0.5 and 2.5 hours of cooling, respectively. Simulations were done for the parameters in Table 3.5.1 using the "Modeled beam" approach in BETACOOL. The corresponding luminosity with and without cooling is shown in Fig. 3.5.3.

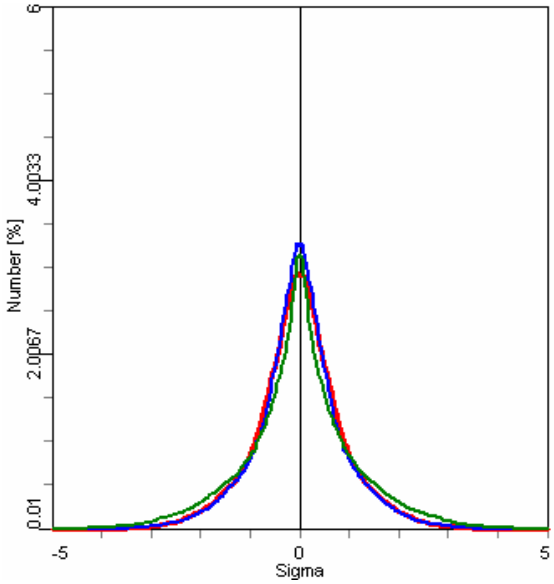

Fig. 3.5.1 Beam profiles (x-red, y-blue, longitudinal -green) after 30 minutes of cooling

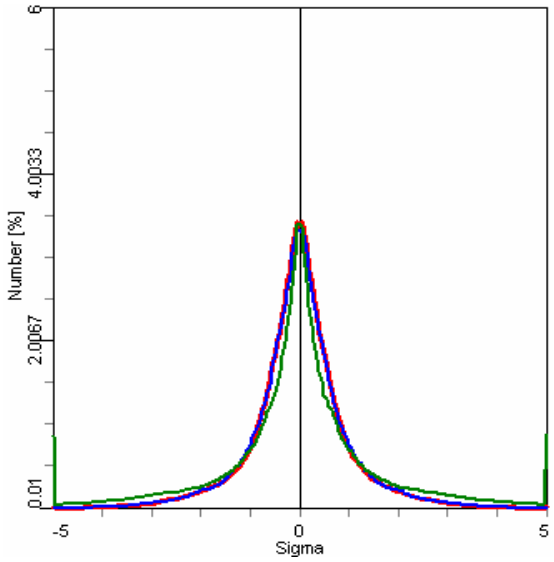

Fig. 3.5.2 Beam profiles after 2.5 hours of cooling.

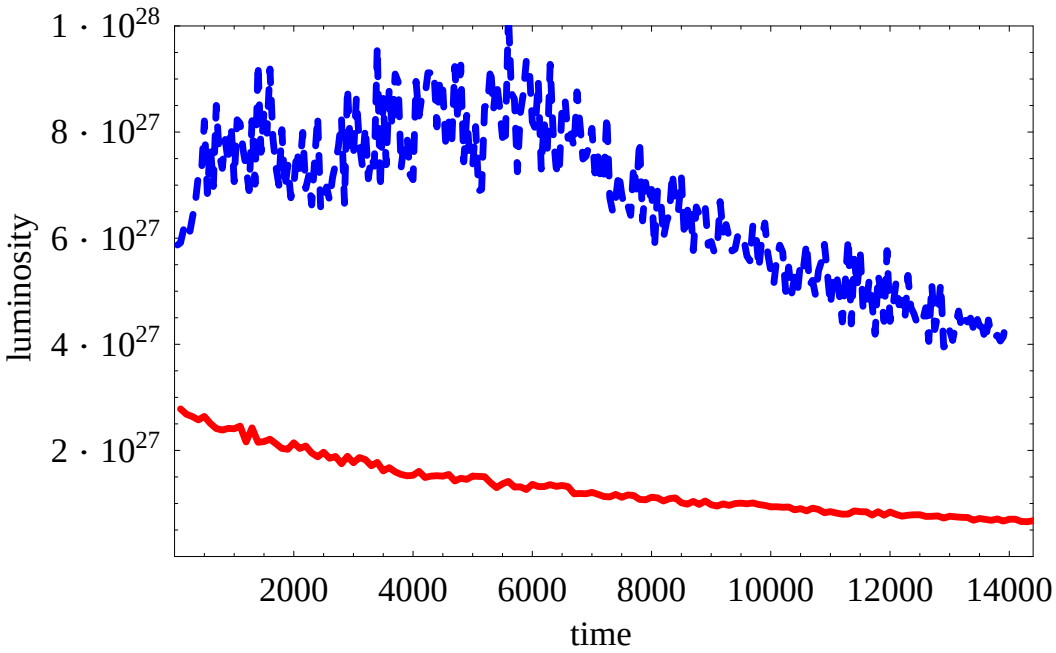

Fig. 3.5.3 Luminosity of Au ions [cm^2 s^{-1}] vs time [sec] with (blue) and without (red) cooling using "Modeled beam" approach in BETACOOL simulations for parameters in Table 3.5.1, and assuming collisions in 3 IP.

For the case shown in Fig. 3.5.3, average luminosity with cooling (blue) per store is $<L>=7\cdot10^{27}$[cm^2sec^{-1}]. Without cooling, Fig. 3.5.3 shows "ideal" luminosity which may be possible to achieve which corresponds to about $<L>=1\cdot10^{27}$ [cm^2sec^{-1}]. More pragmatic estimate for luminosity of RHIC-II without cooling gives $<L>=0.8\cdot10^{27}$ [cm^2sec^{-1}]. The drop in luminosity with cooling is due to collisions in 3 IP's ("burn-off" process). With 2 IP's (which is present baseline for RHIC-II) the burn-off process is less pronounced and average luminosity in 4 hour store is higher than $7\cdot10^{27}$ [cm^2sec^{-1}], as shown in Fig. 3.5.4. The simulation presented in Fig. 3.5.4 also includes automated procedure of painting with electron beam which is discussed in Section 3.6. In addition, further increase in luminosity is possible by going to higher charge of the electron beam and smaller beta function in the IP but the optimum time of store becomes rather short.

3.5.3 Requirements on longitudinal momentum spread of electron beam

The rms momentum spread of the ion beam is about $0.5\cdot10^{-3}$. An effective longitudinal cooling is obtained with the rms momentum spread of the electron beam around $0.3\cdot10^{-3}$. Simulations were performed to find out requirement on the average electron beam energy. The cooling efficiency was significantly affected when the average energy of the electron beam became comparable or bigger than the rms energy spread of the ion beam. This sets a requirement on average energy deviation of the electron beam to be around $0.3\text{-}0.5\cdot10^{-3}$.

3.5.4 Requirements on transverse emittance of electron beam

Ideally, one would like to have the transverse rms velocity spread of the electron beam to be comparable or smaller than the one of the ions. Since the normalized rms emittance of ions is 2.5 μm an ideal electron emittance should be about 2.5 μm or less. However, the necessary cooling power requires charge within electron bunch to be around 5nC. Recent progress in simulations of electron beam transport indicates that for 5nC charge of electron beam one can obtain transverse emittance smaller than 4 μm (see next Section 4 on Electron Beam Dynamics). However, besides emittance there are many other effects which can impact electron beam quality. Such effects are presently under study. This puts an extremely challenging requirement on the control of an angular spread within electron beam, as discussed in next section.

3.5.5 Angular spread within electron beam

To ensure good cooling performance a quality of the electron beam should not suffer significantly as a result of the electron beam transport in ERL, merging of the electron and ion beam, transport through the cooling section and interactions with the ion beam.

An increase in the electron emittance (transverse angular spread) and longitudinal momentum spread was estimated due to various effects and is described in Section 4 in detail. Here, we summarize contribution of various effects to the total angular spread of the electron beam in the cooling section, and discuss how it affects cooling performance.

With the non-magnetized cooling approach, electron angles in the cooling section should be comparable to the angular spread of the ion beam being cooled. With ion beam 95% normalized emittance of 15 [mm mrad] and beta-function in the cooling section of 400 [meters], the rms angular spread of ion beam is 7.6 [μrad].

In our baseline cooling simulations with 5nC electron beam we assumed “effective” rms angular spread of the electrons of 8.6 [μrad], which, for example, corresponds to the electron beam rms normalized emittance (thermal contribution) of 4 [μm] if no other contributions to electron angular spread are present.

With an additional (besides thermal contribution given by electron beam emittance) single contribution of 5 [μrad], the total budget of rms angular spread of the electrons becomes already 10 [μrad]. To have a minimum impact on cooling performance with baseline parameters our goal is to constrain total contribution to the rms angular spread of the electrons to about 10 [μrad].

Emittance of 3 [μm] (rms, normalized) corresponds to rms angular spread of 7.5 [μrad] and allows to have at least few additional contributions from other sources. So, the goal for emittance values of 5nC bunch should be 3 [μm] or even smaller.

Total rms angular spread with the thermal emittance of 3 [μm] and 3 additional contributions of 5 μrad each gives $(7.5^2+3\cdot5^2)^{-1/2}$=11.5 [μrad]. Total rms angular spread with 2 additional contributions of 5 μrad each gives $(7.5^2+2\cdot5^2)^{-1/2}$=10.3 [μrad].

Expected contributions to the rms angular spread of the electrons are summarized in Table 3.5.2.

Effects	Contribution without correction [μ rad]	Measures/tasks	Remaining contribution [μ rad]
Emittance (thermal contribution)	7.5 (for 3 μm rms normalized emittance)		7.5
Space-charge	50	Compensating solenoids. Develop approach to minimize non-linear contribution	5 (presently achieved for ideal distribution; studies are under way to achieve good compensation for realistic distribution).
Effect of wall images		Requirement on beam centroid 1 mm offset from beam pipe center	<1
Undulator errors		integral of transverse mag. fields < 1e-6Tm	5
Residual magnetic field		Shielding to 3mGauss (complications when there is interplay with undulator fields)	5
Neutralization (ni/ne in transport channel)	Control of neutralization to better than 1e-5 level	Find which level of neutralization can be achieved	<1
e-cloud	200	NEG coating – reduction by about factor of 10. suppression of e-cloud with undulator	<1
Aberrations/non-linearities		Needs to be addressed	to be studied
Envelope mismatch		Needs to be addressed	<1
Collective effects (resistive wakes, bellows, cavities)			<1
e/e IBS, e/ion IBS, CSR, e/ion defocusing			<1

Table 3.5.2: Contributions to the rms angular spread of 5nC electron beam in the cooling section.

Based on Table 3.5.2, the total rms angular spread expected (assuming 5nC electron bunch with 3 [μm] rms normalized emittance) is $(7.5^2+3\cdot5^2)^{-1/2}$=11.5 [μrad]. Efforts are presently being made to minimize contributions to this effective angular spread by a proper design of the cooling section.

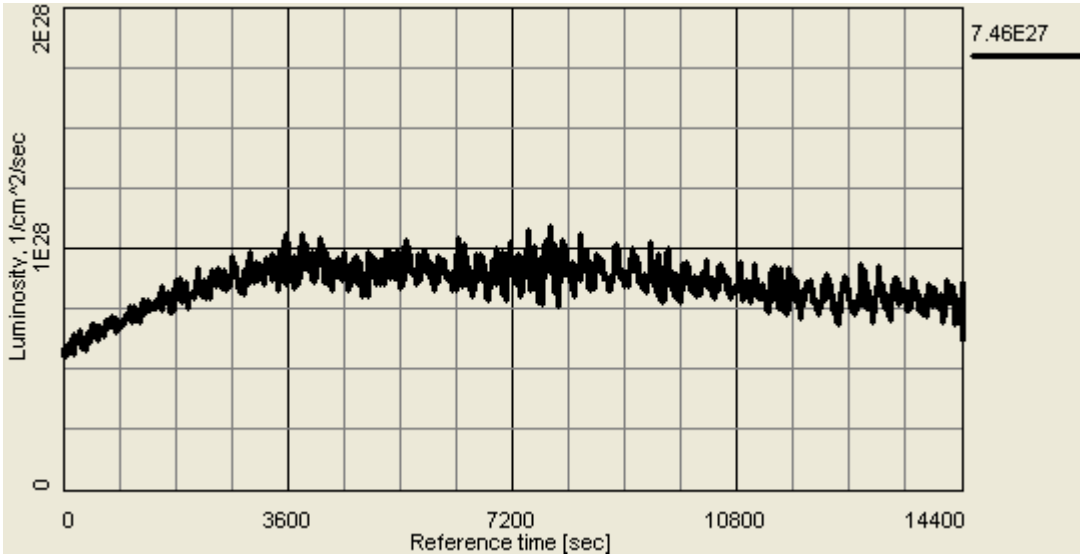

Fig. 3.5.4 Luminosity performance for rms angular spread of electrons 8.7 μrad (with collisions in two IP's).

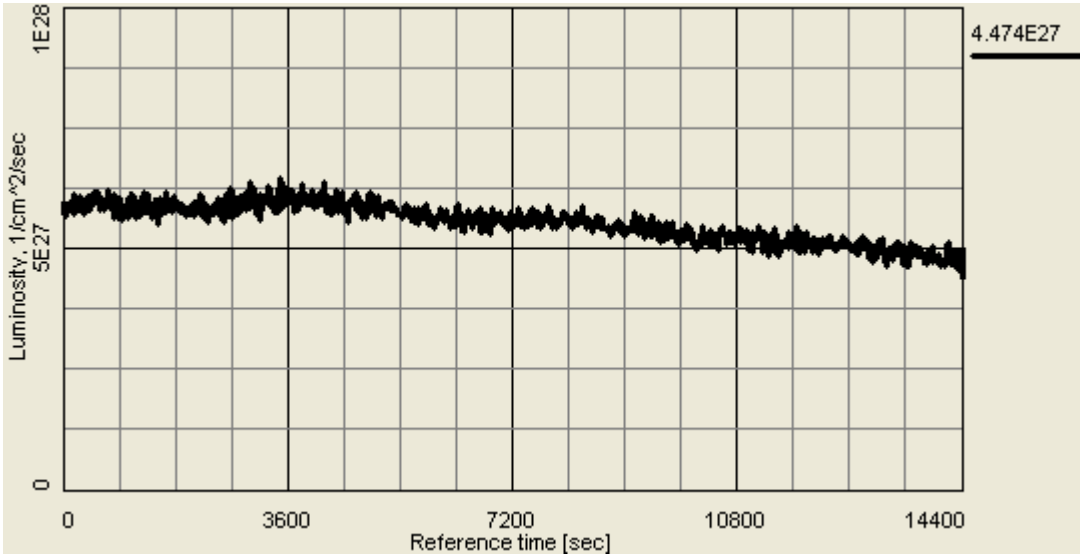

Fig. 3.5.5 Luminosity performance for rms angular spread of electrons 13 μrad (with collisions in two IP's).

For total rms angular spread of electron beam in the cooling section of 8.7 [μrad], average luminosity in 4 hour store in Fig. 3.5.4 is $<L>=8.5\cdot10^{27}$ [cm^2sec^{-1}] (with collisions in two IP's). If rms angular spread is increased to 13 [μrad], average luminosity in 4 hour store in Fig. 3.5.5 becomes $<L>=5.7\cdot10^{27}$[cm^2sec^{-1}], which is a drop of 50% in an average luminosity. If total rms angular spread happens to be factor of 2 larger than the design goal of 10 [μrad], the drop of cooling performance will be much stronger. Presently, careful design of the cooling section is underway to ensure that total angular spread of a design level (<10 [μrad]) is achieved. However, if the angular spread happens to be much bigger than designed, for example 20 [μrad], to recover the average

luminosity needed, other schemes of cooling are also being planned. For example, the 703MHz frequency of ERL corresponds to the longitudinal spacing between electron beams of 40cm. This allows us to put two electron bunches on a single ion bunch with planned rms bunch length of 20 cm (full bunch length about 1 meter). In such an approach, one recovers cooling performance similar to 13 [μrad] with a single electron bunch, as shown in Fig. 3.5.6. Other schemes are also being investigated.

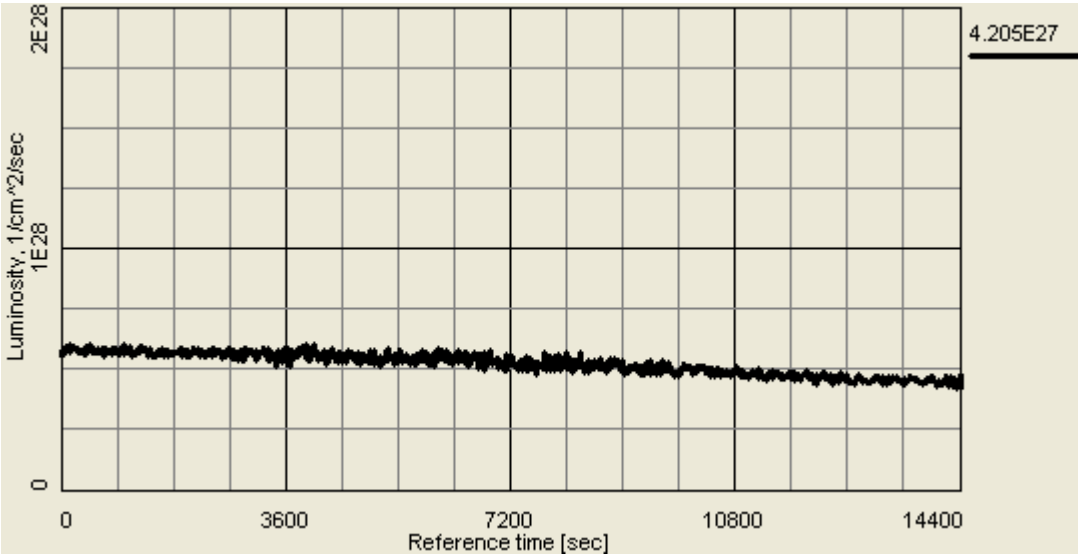

Fig. 3.5.6 Luminosity performance for rms angular spread of electrons 20 μrad. Using a scheme with two electron bunches spaced by 40cm.

3.5.6 Cooling optimization

Major parameters which affect beam cooling are:

1. Length of cooling section – directly impacts cooling speed.
2. Cooling current – directly impacts cooling speed.
3. Dependence on beta-function in the cooling solenoid – partially offset by ion beam size increase – corresponding increase of electron beam size leads to reduction of electron density.
4. Alignment of electron-ion beam.
5. Transverse and longitudinal rms velocity spread within electron beam.

These effects are taken into account in cooling simulations to obtain largest average luminosity per store.

3.5.7 Cooling performance with and without recombination suppression

The undesired beam loss due to recombination can be controlled by an undulator field in the cooling section. However, the resulting friction force with the undulator field is reduced, which was

confirmed by the simulations (see Section 3.2.4). As a result, depending on the parameters of the electron beam and the cooler, there may be even a small loss in the integrated luminosity with the undulator field being switched on compared to the case with the undulator switched off. For the present baseline parameters in Table 3.5.1, the integrated average luminosity is higher with the undulator switched on. This is shown in Figs. 3.5.7-9.

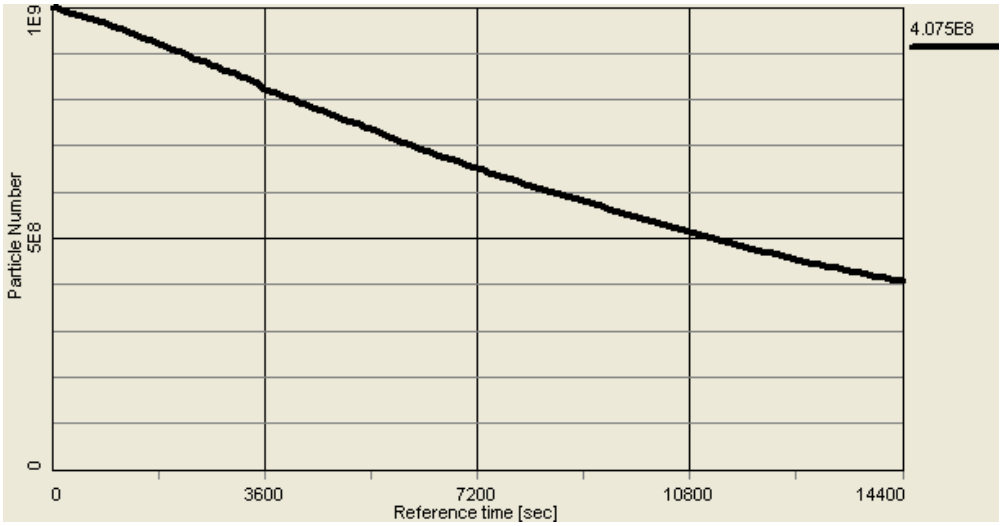

Fig. 3.5.7 Particle loss only due to collisions in 3 IP (recombination loss is turned off).

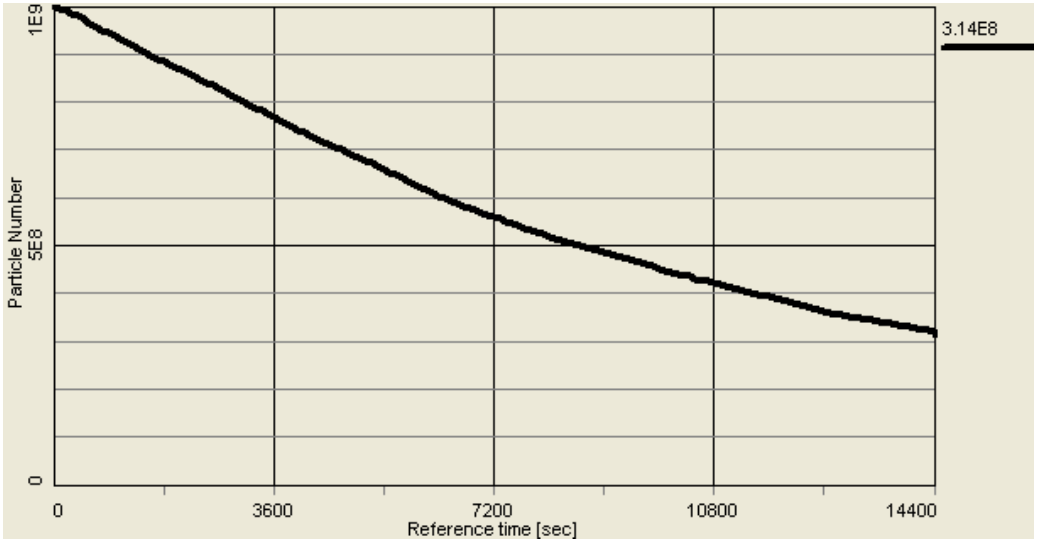

Fig. 3.5.8 Particle loss due to collisions in 3 IP and recombination in the cooler.

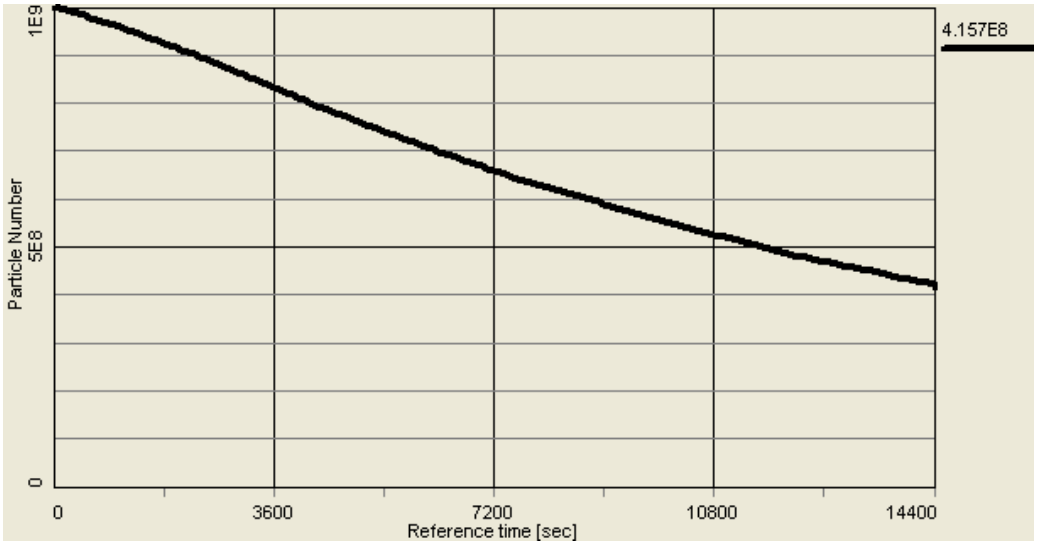

Fig. 3.5.9 Particle loss due to collisions in 3 IP, recombination in the cooler, and undulator with parameters in Table 3.4.1.

For parameters in Table 3.5.1 and 3 IP's, as a result of loss on recombination, an average luminosity during 4-hour store is $<L>=6\cdot10^{27}$ [cm^2sec^{-1}] (corresponding to Fig. 3.5.8), with 18% of luminosity lost on recombination. With the recombination suppressed by undulators (Fig. 3.5.9), most of the luminosity loss during 4-hour store can be recovered.

3.6 Scenarios of cooling at RHIC: heavy ions

There are various possibilities of using electron cooling at RHIC [6]. Direct cooling at 100 GeV is considered as a base line approach for RHIC-II. However, for eRHIC [31], it is important that cooling is fast enough and sufficient to have the rms beam parameters being cooled substantially, especially the rms bunch length. In such a case, pre-cooling at low energy becomes very attractive due to a strong dependence of the cooling time on energy. For the same reason, cooling is very effective for scenarios with collisions at low energy [6].

Direct cooling of Au ions at storage energy of 100 GeV/n with parameters in Table 3.5.1 allows us to reach a desired increase in the luminosity ($<L>=7\cdot10^{27}$ [cm^2sec^{-1}] during 4-hour store with 3 IP's, or higher average luminosity with 2 IP's (less "burn-off")) for the RHIC-II upgrade. Some details of the simulations for various scenarios can be found elsewhere [32, 33].

It can be shown that the longitudinal cooling rate of a long electron bunch with its length approximately equal to the one of ions is identical to the cooling rate of a very short electron bunch which is constantly moved back and forth in the longitudinal direction from the center of ion bunch towards its tails. We refer to such procedure as "painting".

Painting procedure was tested within the BETACOOL code where the electron bunch was moved slowly from the longitudinal center of the ion bunch to 2 rms values in the longitudinal direction and back to the center. The resulting longitudinal distribution (green) can be seen in Figs. 3.6.1 – 3.6.4. Cooling of the longitudinal tails and stabilization of the ion rms bunch length was clearly observed. Figures 3.6.5 –3.6.7 show resulting rms bunch length and emittance, respectively. In addition, painting with the electron beam allows to avoid additional complication in the electron beam transport system by transporting short bunch.

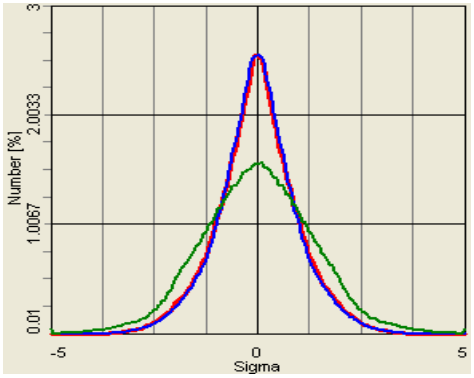

Fig. 3.6.1 Beam profiles with electron bunch moving towards large amplitudes.

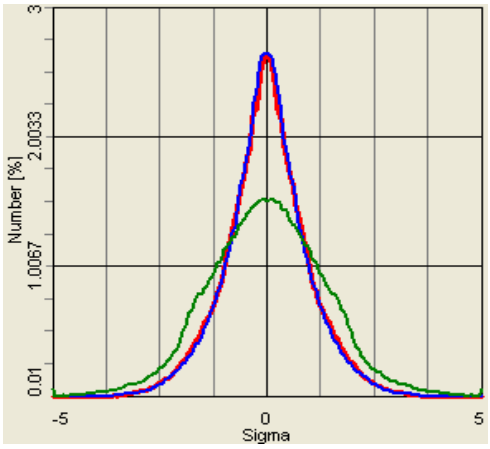

Fig. 3.6.2 Beam profiles with the electron bunch sitting at 2 rms of the distribution.

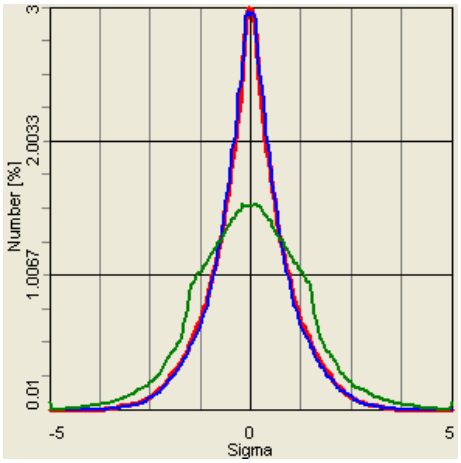

Fig. 3.6.3 Beam profiles with the electron bunch moving back towards the center.

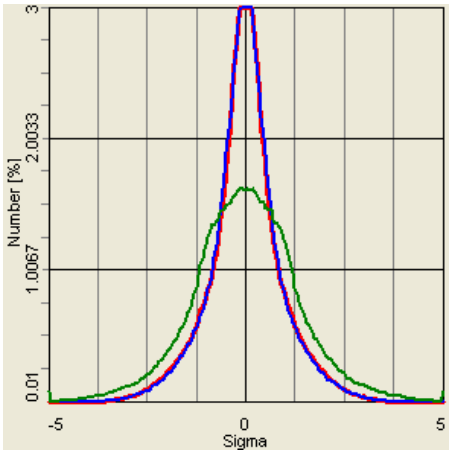

Fig. 3.6.4 Example of the distribution resulting due to the longitudinal painting.

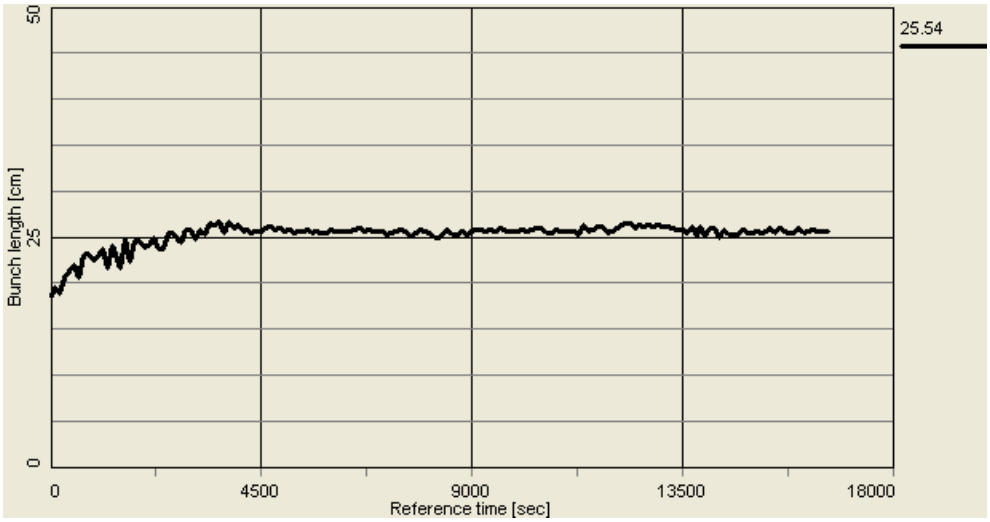

Fig. 3.6.5 Rms bunch length with painting, using "Modeled beam" approach.

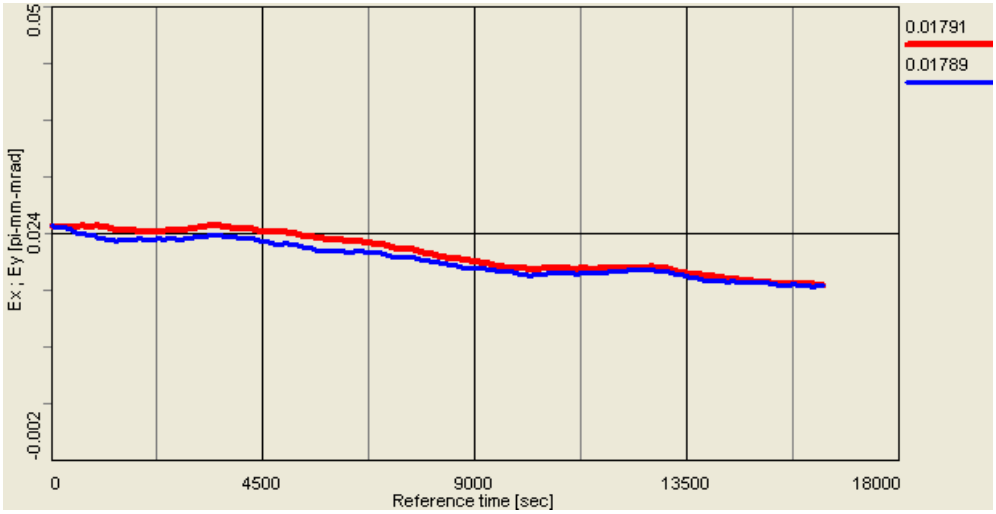

Fig. 3.6.6 Rms emittance with painting, using "Modeled beam" approach.

With a smooth procedure for painting one can prevent any growth of the rms bunch length, as shown in Fig. 3.6.7.

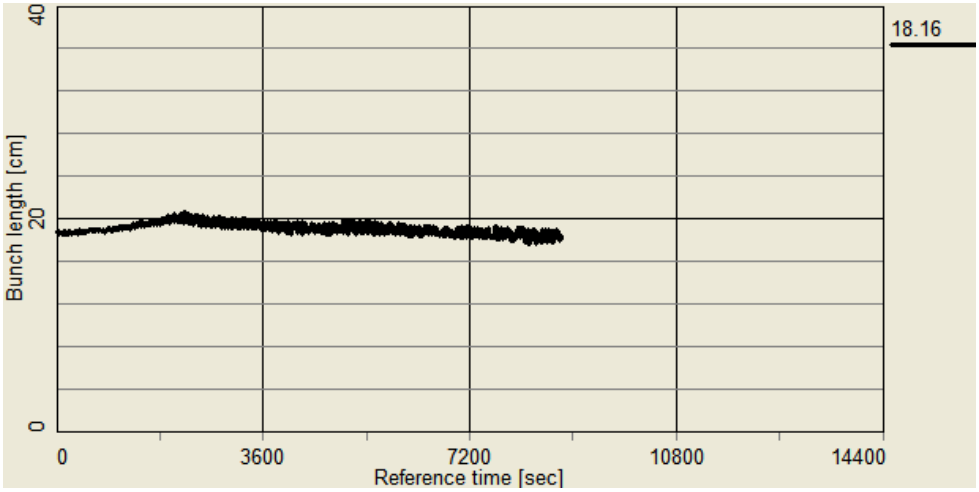

Fig. 3.6.7 Rms bunch length with painting, using "Modeled beam" approach.

As a result of these studies, our conclusion is that painting procedure is an effective way to control the longitudinal bunch length of ions. We found that stretching of electron beam is not necessary and that the needed cooling rates can be obtained with a short electron bunch together with a procedure of painting. The rms length of electron bunch is presently given by the transport of the electron beam and is approximately 1 cm.

In addition to painting, the stochastic cooling system, which is presently under development for RHIC, should be very effective in cooling of tails of the distribution.

3.7 Scenarios of cooling at RHIC: protons

For protons, the best performance is achieved when protons are first pre-cooled at low energy. Various scenarios for cooling of protons were performed (not discussed here). Here, we just give two examples of performance at 100 and 250 GeV.

For the case of collisions at the top energy of 100 GeV, even without pre-cooling at low energy one obtains promising results. Such a direct cooling at 100 GeV is shown in Figs. 3.7.1-2 for the rms emittance and bunch length, respectively.

The following parameters were used. Protons: initial 95% normalized emittance 12 π μm, rms radius 4.7mm (beta function 800m), h=2520. Electrons: q=5nC, rms emittance 3 π μm , rms radius 5.0mm.

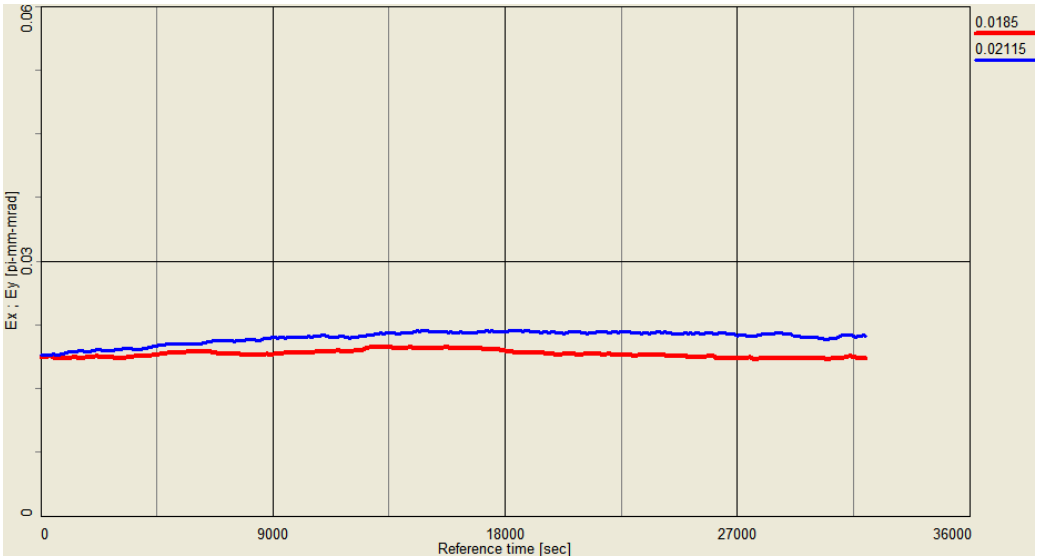

Fig. 3.7.1 Time evolution of horizontal and vertical rms emittances - cooling of protons at 100 GeV (with initial 95% normalized emittance of 12 mm mrad). Plotted emittances are rms unnormalized.

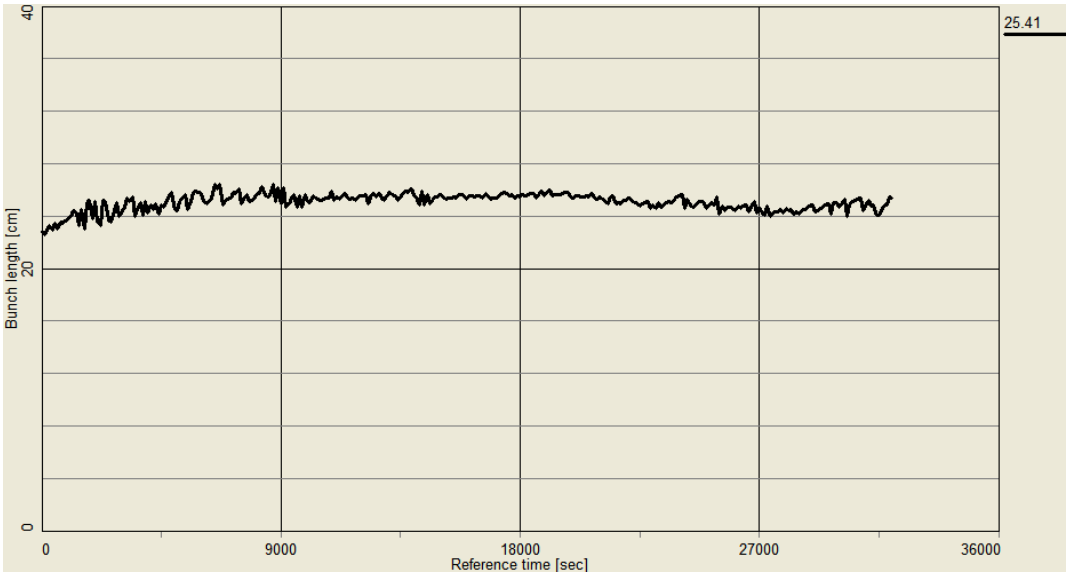

Fig. 3.7.2 Time evolution of rms bunch length – direct cooling at 100 GeV.

For collisions at the top energy of 250GeV, it was found that direct cooling with present baseline parameters do not have significant impact on the luminosity. The purpose of electron cooling is thus to pre-cool proton beam at low energy (if needed) and then let emittances grow at the top energy of 250 GeV due to IBS. The resulting luminosities in such approach are equal or higher than the baseline luminosity of RHIC-II (see Table 3.1.1).

Figures. 3.7.3-4 show time evolution of the rms emittance and bunch length, respectively. The following parameters were used. Protons: initial 95% normalized emittance 12 π μm, h=2520.

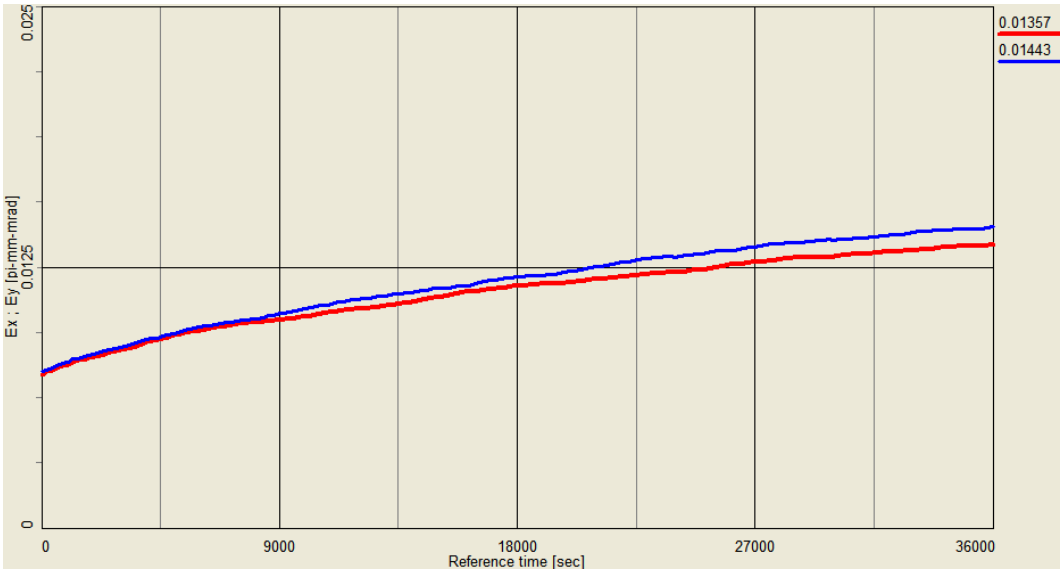

Fig. 3.7.3 Time evolution of horizontal and vertical rms emittances - protons at 250 GeV (no cooling). Plotted emittances are rms unnormalized.

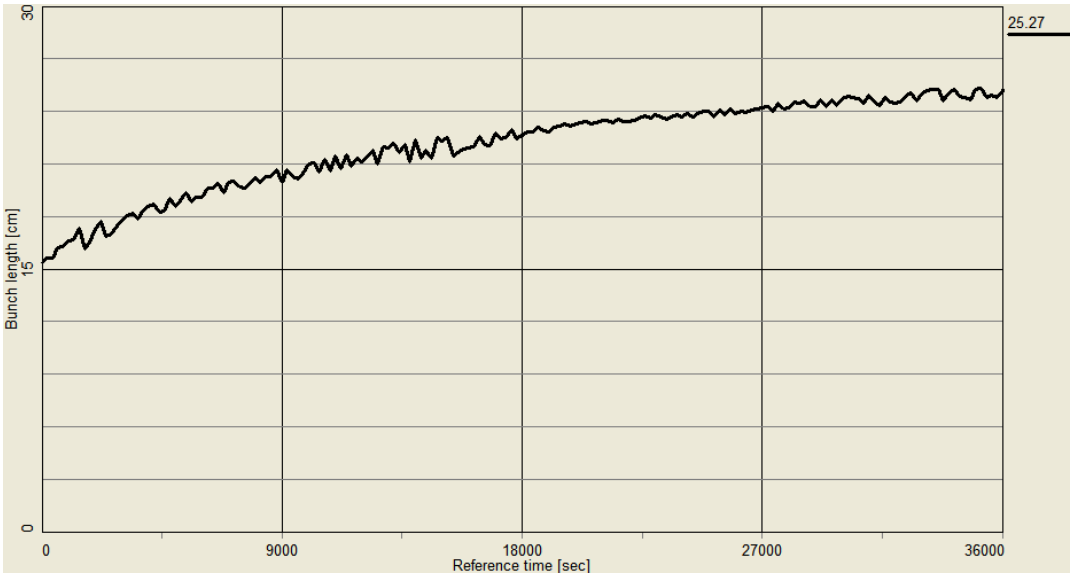

Fig. 3.7.4 Time evolution of rms bunch length – protons at 250 GeV (no cooling).

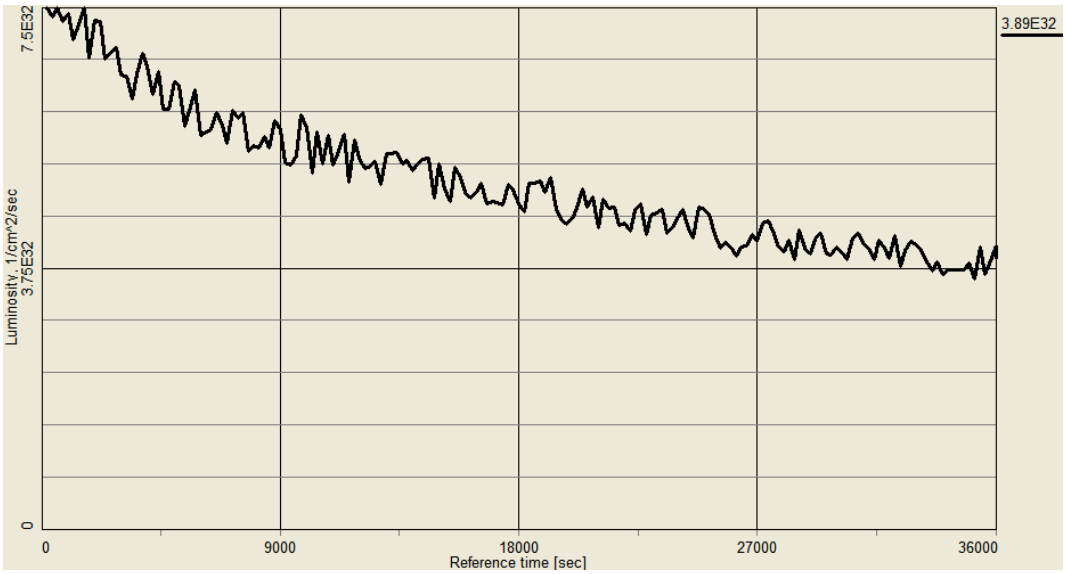

Fig. 3.7.5 Time evolution of luminosity for protons at 250 GeV (no cooling).

For parameters used in simulations in Figs. 3.7.3-5 (112 bunches, beta*=0.5m, N=2e11) the peak luminosity is $L=7.5\cdot10^{32}$ [cm^2sec^{-1}]. The average luminosity during 10-hour store is $<L>=5\cdot10^{32}$ [cm^2sec^{-1}], which is the baseline goal of RHIC-II for protons at 250 GeV (see Table 3.1.1).

Further increase (beyond present RHIC-II design) in proton luminosities is possible by pre-cooling of protons at low energy (for example, pre-cooling at 30 GeV was simulated) and/or minimizing initial beta*. Figures. 3.7.6-9 show time evolution of the rms emittance and bunch length and resulting luminosities for protons at 250 GeV when initial 95% normalized emittance of protons was first pre-cooled to 8 π μm at low-energy (not shown). Evolution of the beam parameters are then shown for the top energy of 250GeV without cooling at this top energy.

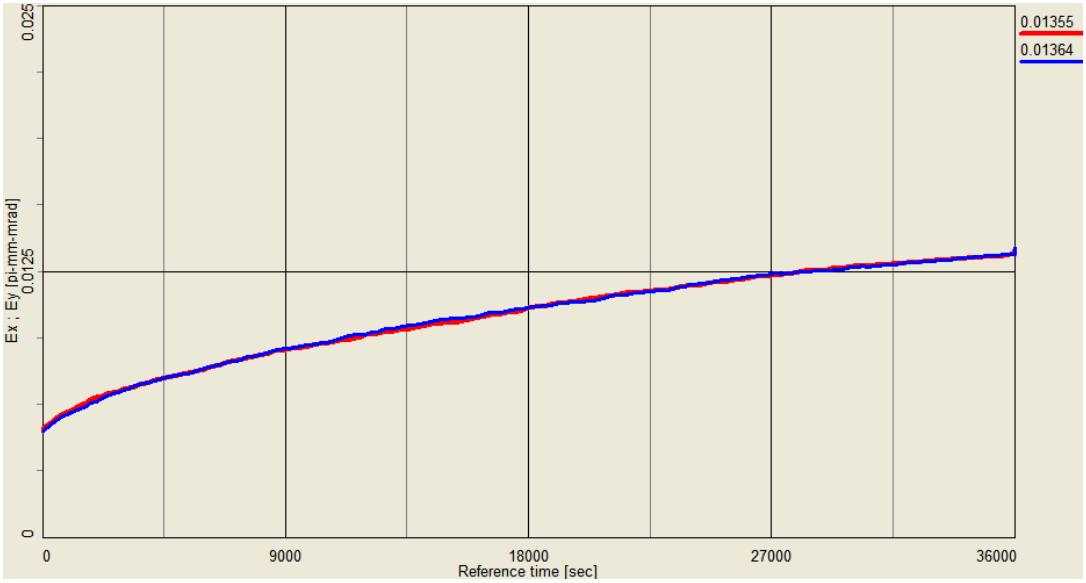

Fig. 3.7.6 Time evolution of horizontal and vertical rms emittances - protons at 250 GeV with initial 95% normalized emittance of 8 π μm (pre-cooled at low energy). Plotted emittances are rms unnormalized.

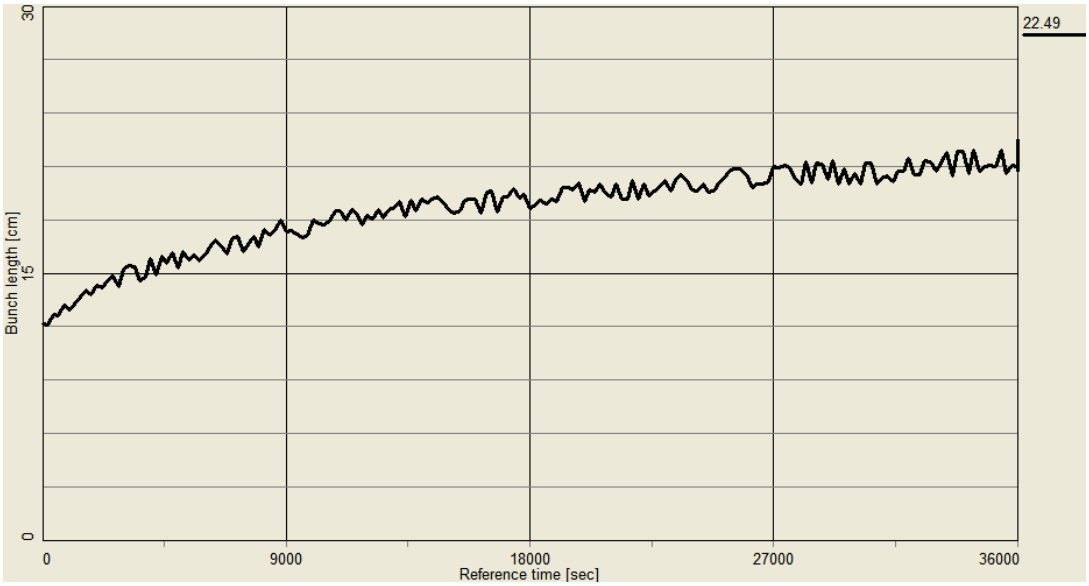

Fig. 3.7.7 Time evolution of rms bunch length – protons at 250 GeV.

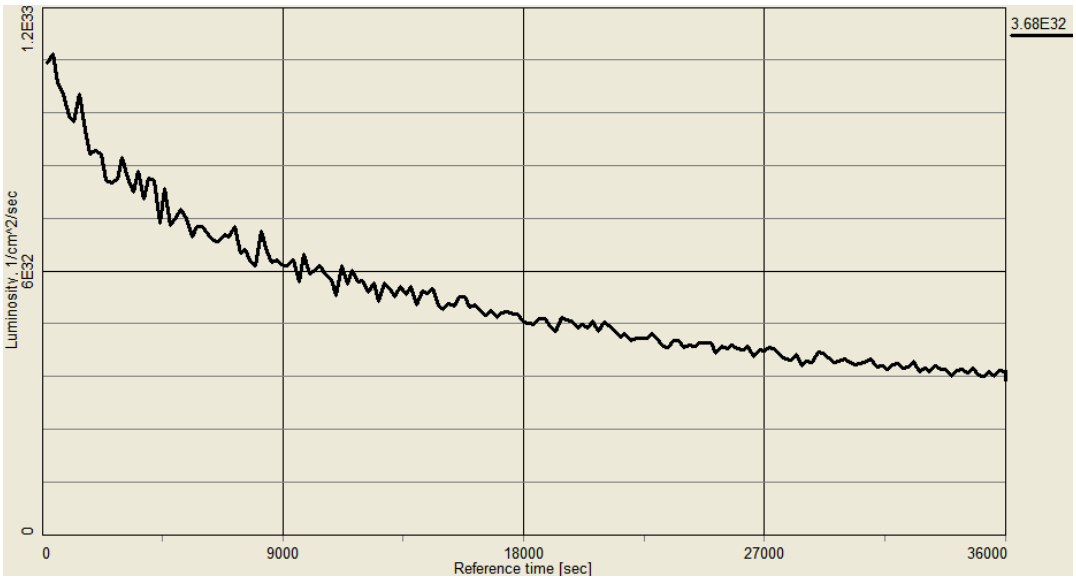

Fig. 3.7.8 Time evolution of luminosity for protons at 250 GeV. Initial emittance 95% normalized emittance of 8 π μm (pre-cooled at low energy), beta*=0.5m. No cooling at the top energy.

For parameters in Fig. 3.7.8 (112 bunches, beta*=0.5m, N=2e11, initial 95% normalized emittance of 8 π μm) the peak luminosity is $L=1.0\cdot10^{33}$ [cm^2sec^{-1}]. The average luminosity during 6-hour store is $<L>=6.3\cdot10^{32}$ [cm^2sec^{-1}].

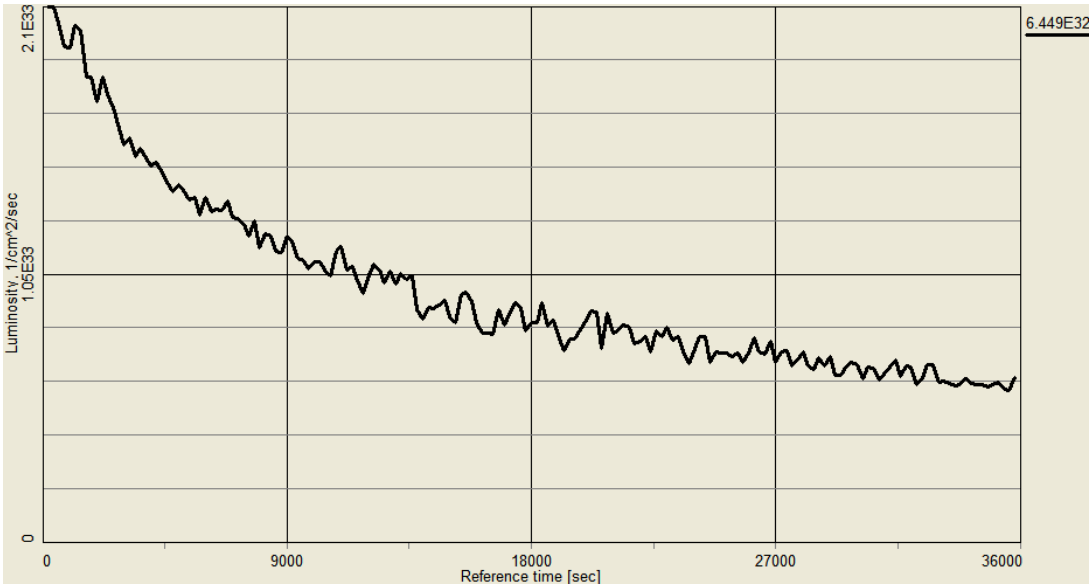

Fig. 3.7.9 Time evolution of luminosity for protons at 250 GeV (initial emittance 95% normalized emittance of 8 π μm, beta*=0.5m)

For parameters in Fig. 3.7.9 (112 bunches, beta*=0.25m, N=2e11, initial 95% normalized emittance of 8 π μm) the peak luminosity is $L=2.0\cdot10^{33}$ [cm^2sec^{-1}]. The average luminosity during 10-hour store is $<L>=1\cdot10^{33}$ [cm^2sec^{-1}].

3.8 Luminosity limitations under cooling

3.8.1 Incoherent beam-beam effects

The electro-magnetic force field of a moving bunch produces a force which acts on individual particles in another bunch moving in the opposite direction. Such force acting on individual particles is referred to as incoherent beam-beam force. One can integrate this force over the collision to obtain the incoherent beam-beam kick.

Beam-beam kick for head-on collision

One typically starts consideration of beam-beam effects with calculation of an increment of transverse particle momentum change after crossing the encounter bunch, considering "strong-weak" approximation of beam-beam interaction. In this model it is assumed that particles of the weak-beam (index 2) are influenced by a strong electromagnetic field of the opposite bunch (index 1), while the strong bunch does not feel any field of the weak bunch.

The change of slope of particle trajectory in linear approximation can be written as follows:

$$\Delta\frac{dx}{ds}=\frac{\Delta p_x}{p_s}=4\pi\frac{\xi_x}{\beta_x^*}x\,,\ \Delta\frac{dy}{ds}=\frac{\Delta p_y}{p_s}=4\pi\frac{\xi_y}{\beta_y^*}y\,, \qquad (3.8.1)$$

where ξ_x, ξ_y are beam-beam parameters, which have a meaning of linear part of betatron tune shift due to beam-beam collision:

$$\xi_x = N_1 \frac{\beta_x^*}{4\pi} \frac{q_1 q_2}{4\pi\varepsilon_0 m_2 c^2} \frac{(1+\beta_1\beta_2)}{\gamma_2\beta_2(\beta_1+\beta_2)} \frac{2}{\sigma_x(\sigma_x+\sigma_z)}, \tag{3.8.2}$$

$$\xi_y = N_1 \frac{\beta_y^*}{4\pi} \frac{q_1 q_2}{4\pi\varepsilon_0 m_2 c^2} \frac{(1+\beta_1\beta_2)}{\gamma_2\beta_2(\beta_1+\beta_2)} \frac{2}{\sigma_z(\sigma_x+\sigma_z)}. \tag{3.8.3}$$

Here, the values of beta-function at the interaction point are β_x^*, β_y^*

For collisions of the particles at equal velocities ($\beta_1 = \beta_2 = \beta$), charge numbers ($q_1 = q_2 = Z$) and atomic numbers the beam-beam parameters can be simplified:

$$\xi_x = \frac{\beta^*}{4\pi} \frac{Z^2}{A} r_p \frac{N(1+\beta^2)}{\beta^2\gamma\sigma_x(\sigma_x+\sigma_z)}, \tag{3.8.4}$$

$$\xi_z = \frac{\beta^*}{4\pi} \frac{Z^2}{A} r_p \frac{N(1+\beta^2)}{\beta^2\gamma\sigma_z(\sigma_x+\sigma_z)}. \tag{3.8.5}$$

For the relativistic factor $\beta=1$ one has

$$\xi = \frac{\beta^*}{2\pi} \frac{Z^2}{A} r_p \frac{N}{\gamma\sigma_z(\sigma_x+\sigma_z)} \tag{3.8.6}$$

Stability of linear incoherent motion

In the linear approximation, the motion of a test particle in the presence of the other beam is stable if the absolute value of the trace of the one-turn transfer matrix is less than 2.

Such stability criteria gives very large attainable linear beam-beam tune shifts, which indicates that much smaller experimentally achieved beam-beam parameters are not due to this stability mechanism.

3.8.2 Coherent beam-beam effects

Coherent beam-beam effects arise from the forces which an exciting bunch exerts on a whole test bunch during collision. The corresponding coherent kick is obtained by integrating incoherent beam-beam kick over the charge distribution of the test bunch. In ideal case, due to a symmetry, the coherent beam-beam kick vanishes for head-on collisions.

Linear tune shift

The linear coherent beam-beam tune shift can be calculated and becomes just one half of the linear incoherent shift ξ :

$$\Xi = \frac{\beta^*}{4\pi}\frac{Z^2}{A} r_p \frac{N}{\gamma\sigma_x(\sigma_x+\sigma_z)} \qquad (3.8.7)$$

Stability of linear coherent motion

Coherent oscillation of two beams under certain condition can lead to instability. With one bunch per beam to modes are possible, the 0-mode, where both beam oscillate in phase and π-mode where both beam oscillate out of phase. With m bunches per beam, one gets $2m$ modes of oscillation, correspondingly.

The stability of the system can be also calculated in the linear matrix theory. Although the threshold is now significantly lower then in the incoherent case it is still well above the experimentally observed beam-beam limits.

3.8.3 Nonlinear effects and beam-beam limit

Non-linear tune spread and resonances

The nonlinear variation of the beam-beam force with radius in a round Gaussian beam causes a tune shift of individual particles to have dependence on particle oscillation amplitude. For the distribution of particles within the beam this results in a tune-spread in the beam. In addition the beam-beam force drives non-linear resonances.

Experimental beam-beam limit is usually attributed to excitation of non-linear resonances. Overlapping of resonances results in stochastic particles motion with corresponding particle loss. The strength of nonlinear beam-beam resonances can be related to the incoherent beam-beam parameter which allows to use its value to describe beam-beam limit. In principle, an estimate of the real beam-beam limit should include nonlinear resonances excited by the magnet imperfections which then make beam-beam limit to be machine dependent.

In lepton machines, the beam-beam tune spread is much high than in hadron machine. As a result, many nonlinear resonances are crossed. However, diffusion caused by a very high-order nonlinear resonance is compensated by intrinsic damping mechanism of lepton machines which is the synchrotron radiation.

In the absence of damping mechanism diffusion even by a very high-order resonances can have significant effect on particles losses, which is believed to be the case for hadron machine. Introduction of additional fast damping mechanism, such as e-cooling can offset diffusion due to high-order resonance, at least partially, and thus lead to higher values of beam-beam parameters. Due to very slow cooling rates at high energy, this damping mechanism may not lead to

compensation of beam-beam diffusion. However, this question of equilibrium between beam-beam and cooling requires very careful computational study, especially for non-Gaussian distributions which may appear as a result of cooling.

3.8.4 Beam-beam simulations for ion beam under cooling

It is extremely important to treat beam-beam effects for the ion beam while the cooling is present. The main purpose of cooling is to counteract diffusion of ion beam which may be caused by various effects. For accurate treatment, dynamic simulation code should include both cooling and diffusion sources, including intrabeam scattering and beam-beam diffusion. As a simple model, one can describe beam-beam effects with a diffusion coefficient, based on beam-beam space-charge force. Such a coefficient, either approximate analytic or empiric (based on real measurements in RHIC) can be used in dynamic simulation code. Simulations of beam cooling including beam-beam diffusion are planned in the future.

As a result of beam-beam force one has two major effects: excitation of beam-beam resonances and tune spread. Because of the tune spread many non-linear imperfection resonances can be crossed which results in significant beam diffusion and in so called empiric beam-beam limit. A reliable way to account for beam-beam effects and to have a reasonable description of achievable beam-beam limit is to include non-linear optics of the machine (imperfection resonance) into account. Such simulations of beam-beam effects and cooling are planned in the framework of UAL simulation [34]. In addition, the UAL based simulation should describe both incoherent and coherent effects in a self-consistent manner.

Presently, simulations of electron cooling are done without taking into account beam-beam diffusions. As a guideline we only use the values of the beam-beam parameter which is calculated from the local density when the “Model beam” approach is being used.

As an example, Fig. 3.8.1 shows the beam-beam parameter for the cooling simulations in Fig. 3.5.4 and parameters in Table 3.5.1.

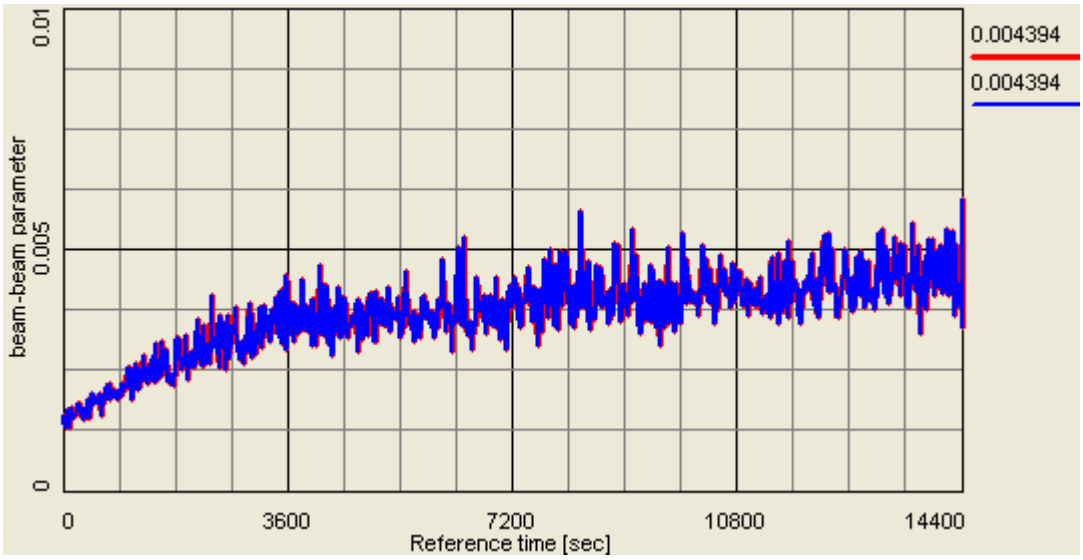

Fig. 3.8.1 Resulting beam-beam parameter for parameters in Table 3.5.1 and Fig. 3.5.4, using local beam density.

3.9 Effects on ion beam dynamics

3.9.1 Tune shifts

1) Incoherent space-charge tune shift within the ion beam

For an ion beam with Gaussian distribution one has

$$\Delta Q_{SC} = \frac{Z^2 N_i r_p C_r}{4\pi A\ \beta^2\gamma^2\varepsilon_{in}\sigma_{is}\sqrt{2\pi}} \qquad (3.9.1)$$

where C_r is ring circumference, ε_{in} is the normalized rms emittance and σ_{is} the rms bunch length. For typical parameters of Au ion beam at 100 GeV one gets ΔQ_{sc} about 0.001.

2) Incoherent tune shift of ions due to interaction with electrons

Electron beam also acts like a focusing lens on positive Au ions which produces an additional tune shift of ion particles:

$$\Delta Q_e = \frac{Z n_e r_p l_c \beta_i}{2A\beta^2\gamma^3} \qquad (3.9.2)$$

where l_c is the length of the cooling section, n_e is the density of electron beam in the laboratory frame and β_i is the average beta-function in the cooling section. For baseline cooler parameter ΔQ_e is about $8\cdot10^{-5}$.

3.9.2 Coherent ion-electron interactions

A simple description of such interaction can be done via the model of two oscillators [35]. Even with such simple model, for typical parameters of low-energy cooler, one can obtain that for a very high electron densities and long cooling section the net effect of ion-electron interaction can result in “heating” of the ion beam rather than cooling.

Approximate models were developed in Refs. [35, 36, 37] which allow us to estimate thresholds of this type of instabilities for RHIC parameters. The thresholds of these instabilities were calculated by G. Wang, and showed that for proposed density of the electron beam, the ion beam will remain stable both in the transverse and longitudinal directions.

For the transverse dipole mode instability estimated threshold requires electron density 3 orders of magnitude larger than designed. For the longitudinal dipole mode instability estimated threshold requires electron density one order of magnitude large than designed. For quadrupole mode instability found threshold is about two orders of magnitude larger than designed values. More details on these estimates for RHIC parameters can be found in a separate report by G. Wang [38].

3.9.3 Collective instabilities for ion distribution under cooling

A careful study of collective instabilities becomes an important issue for ion beam under cooling at least for two reason:

- tune spread and momentum spread decreases which may result in unsufficient Landau damping

- direct space-charge field increases as the beam cools down with a formation of dense core.

The situation is expected to be less critical for present parameter of RHIC cooler, since with present parameters transverse and longitudinal emittances of ions are cooled only slightly, as well as distributions under cooling do not produce dense cores as for the case of the magnetized cooling approach. However, simulation with the realistic RHIC environment are planned in the future to explore this issue in detail.

Requirements on coupling impedance after cooling

For the longitudinal stability a rough condition is

$$\left|\frac{Z}{n}\right| \le F_L \frac{A}{Z_i^{\,2}} \frac{\beta^2 \gamma \left(m_p c^2 / e\right) |\eta|}{I_0} \left(\frac{\Delta p}{p}\right)^2_{FWHM} \qquad (3.9.3)$$

where the longitudinal form factor depends on the distribution and approximately F_L=1. Here, I_0 is the average ion beam current for a coasting beam. For a bunched beam, one can roughly use the local peak current $I_p=eZ_i\beta c/l_b$.

For low-energy cooling, cooling above transition becomes a problem due to the space-charge contribution to the impedance which results in a significant tune shift. For RHIC energies, the space-charge impedance in negligible so that stability will be simply governed by a degree of a collapse of momentum spread $\Delta p/p$. The process of cooling should be carefully controlled to avoid large decrease in $\Delta p/p$.

For the transverse stability, the requirement on the transverse impedance is given by

$$Z_t \le 4F_T \frac{A}{Z_i^{\,2}} \frac{\gamma \left(mc^2 / e\right)}{I_0} \frac{Q}{R} \left(\Delta Q\right)_{FWHM} \qquad (3.9.4)$$

where full tune-spread ΔQ_{FWHM} is given by

$$(\Delta Q)_{FWHM} = \left[\left(\left| (n - Q)\eta + Q' \right| (\Delta p / p) \right)^2 + \left(\left(\partial^2 Q / \partial a^2 \right) a^2 \right)^2 \right]^{1/2} \qquad (3.9.5)$$

The first term in Eq. (3.9.3) is due to the revolution frequency, the second term is due chromaticity Q' and the third term is due to the nonlinear tune spread with octupoles.

A study of the longitudinal and transverse stability of cooled ion beam in RHIC, with the beam distribution resulting due to cooling will be done in the future.

3.9.4 Effect of cooling on polarization of protons

Two effects which may cause depolarization of the circulating ions by the electron cooler are:

1) Spin precession in the longitudinal magnetic field B of the solenoid in cooling section.
2) Hyperfine interactions (hf) with the cooler electrons.

For typical parameters of a low-energy cooler with strong magnetic field in the solenoid, the spin precession angle caused by this field is very large. However, this effect is easily compensated by additional solenoids with opposite field directions. For the present parameters of RHIC cooling section, compensating solenoid pairs consist of the magnets with opposite field directions.

Theoretical estimates of hf effects were done for typical parameters of low-energy cooler. The depolarization times found suggest that this effect is completely negligible.

Experiments with polarized protons were done in circular accelerators equipped with electron coolers, such as IUCF (Indiana, USA) and COSY (Juelich, Germany). No effects on polarization of protons as a result of the electron cooler were observed [39].

3.10 REFERENCES

[1] A.O. Sidorin et al., Nuclear Instr. Methods A 558, p. 325, 2006 (Joint Institute for Nuclear Research, Dubna, Russia http://lepta.jinr.ru).
[2] C. Nieter, J. Cary, J. Comp. Phys. 196 , p.448 (2004); http://www.txcorp.com
[3] S. Nagaitsev et al., PRL 96, 044801 (2006); http://www-ecool.fnal.gov
[4] V.V. Parkhomchuk and I. Ben-Zvi, Tech. Report C-AD/AP/47 (2001).
[5] V.V. Parkhomchuk, A.N. Skrinky, Rep. Prog. Physics 54, p.919 (1991).
[6] A.V. Fedotov et al., Proceedings of PAC05, p 4236; p.4251 (2005).
[7] I. Ben-Zvi, AIP Conf. Proceedings 821 (COOL05, Galena, IL), p.75 (2005).
[8] Ya. Derbenev, TJAB Note, February 2001 (unpublished).
[9] V. Litvinenko, independently proposed to use undulator for recombination suppression (2005).
[10] S. Chandrasekhar, *Principles of Stellar Dynamics* (U. Chicago Press, 1942).
[11] Ya. Derbenev, A. Skrinsky, Part. Accelerators 8, p. 235 (1978).
[12] J. J. Binney, MNRAS 181, p. 735 (1977).
[13] D.L. Bruhwiler *et al*., AIP Conf. Proceed. **773** (Bensheim, Germany, 2004), p. 394.
[14] A. Fedotov, D. Bruhwiler, D. Abell A. Sidorin., AIP Conf. Proc. 821, p. 319 (2005).
[15] A. Fedotov, D. Bruhwiler, A. Sidorin, D. Abell, I. Ben-Zvi, R. Busby, J. Cary, V. Litvinenko, Phys. Rev. ST Accel. Beams 9, 074401 (2006)., Phys. Rev. ST Accel. Beams, V. 9, 074401 (2006).
[16] L. Prost et al., Workshop HB2006 (KEK, Tsukuba, Japan) (2006).
[17] G. Bell et al., RHIC e-cooling workshop (Upton, NY,2006), http://www.bnl.gov/cad/ecooling.
[18] A. Piwinski, Proc. of 9th Intern. Conf. High Energy Acc. (1974); CERN 92-01, p. 405.
[19] M. Martini, CERN PS/84-9 (AA), 1984.
[20] J. Bjorken and S. Mtingwa, Particle Accel. 13 (1983), p.115.
[21] V. Lebedev, AIP Conf. Proc. 773 (HB2004), p. 440.
[22] W. Fischer et al. Proccedings of EPAC02, p. 236 (2002).
[23] J. Wei et al., AIP Conf. Proc. 773 (HB2004), p. 389.
[24] A. Fedotov et al, unpublished (2004).
[25] A. Fedotov et al, Workshop HB2006 (KEK,Tsukuba, Japan), pub. by JACoW, p.259, 2006.
[26] A. Burov, "Electron cooling against IBS", FNL-TM-2258 (2003).
[27] A. Fedotov et al., Proceedings of PAC05, p. 4263 (2005).
[28] G. Parzen, Tech. Notes C-AD/AP/144, C-AD/AP/150 (2004).
[29] M. Horndl et al., PRL 95, 243201 (2005).
[30] A. Wolf, H. Danared, I. Kaganovich (private communications, 2006).
[31] "eRHIC Zeroth-Order Design Report", BNL C-A/AP Note 142 (2004)
http://www.agsrhichome.bnl.gov/eRHIC/eRHIC_ZDR.htm
[32] Cooling dynamics studies: http://www.bnl.gov/cad/ecooling
[33] A.V. Fedotov, I. Ben-Zvi., D.L. Bruhwiler, V.N. Litvinenko, A. O. Sidorin, A.O., New J. Physics, Special issue on Accelerator Physics, Vol. 8, p. 283 (IOP publishers., UK, 2006)
[34] N. Malitsky, R. Talman, "Unified Accelerator Libraries", AIP 391 (1996).
[35] V.V. Parkhomchuck, V.B. Reva, J. of Exp. and Theor. Physics, V.91, p. 975 (2000).
[36] P.R. Zenkevich, A.E. Bolshakov, NIM A 441, p. 441 (2000).
[37] V.B. Reva, Presentation at RHIC electron cooling workshop (Upton, NY, May 2006).
[38] G. Wang, "Collective electron-ion interactions for RHIC e-cooler" (2006):
http://www.bnl.gov/cad/ecooling
[39] I. Meshkov, S. Nagaitsev, J. Dietrich (private communication, 2006).

4 ELECTRON BEAM DYNAMICS

The purpose of this chapter is to provide a brief introduction to the beam dynamics aspects of the electron cooling facility for the Relativistic Heavy Ion Collider based on an energy recovery linac (ERL) [1]. The first section explains the electron injector, which operates in the low energy beam dynamics regime (space charge dominated) and its various beam dynamics aspects (SRF photo gun, emittance compensation scheme, beam merger etc.). The second section is about the high energy beam dynamics, where space charge effects are non critical. The third section describes the beam dynamics in the cooling section, where the beam size is large such that the space charge force again plays the main role in the beam dynamics. In forth part we describe collective effects which may affect the electron beam performance. In the appendix we present benchmarking of the space-charge beam dynamics codes and optimization process.

4.1The high brightness Electron Injector

The electron injector is a critical part of any ERL that has to deliver low emittance and high charge per bunch. For the electron cooling of RHIC we require electron bunches of 5 nC with rms pulse length 35 ps at a low normalized emittance (below 4 mm mrad rms) and a high repetition rate (9.383 MHz), as described in Table 3.1.2 of Chapter 3.

The electron cooler injector (see Fig. 4.1.1.) consist of 1 ½ superconducting RF gun with photocathode located in the half-cell, a solenoid, four chevron dipoles (split focusing) and two opposing solenoids (in order to match the electron beam with linac entrance more accurately).

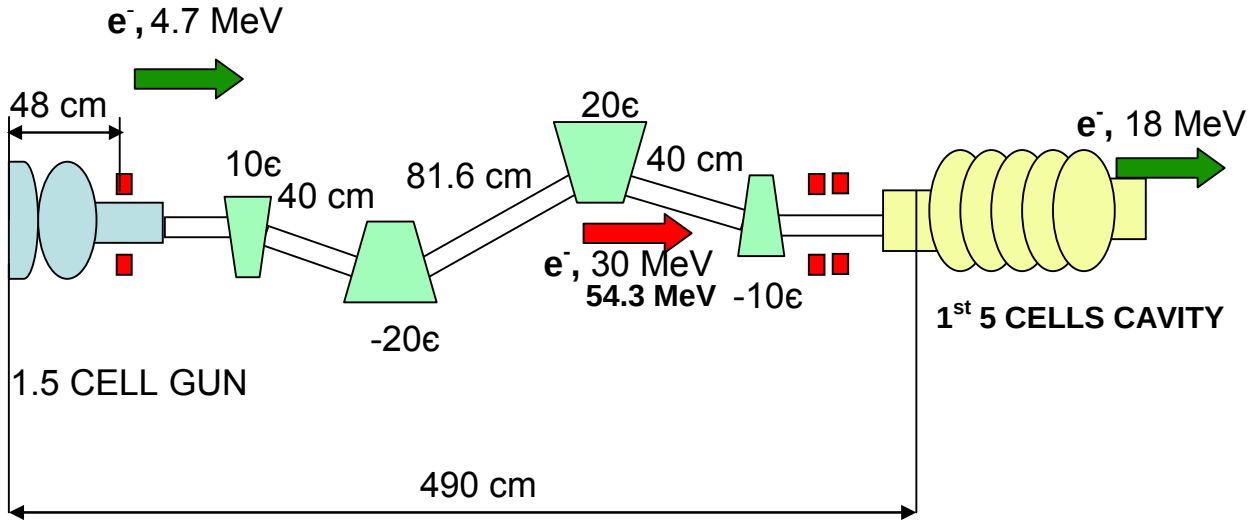

Figure 4.1.1: Schematic layout of SC RF Injector for the RHIC ERL electron cooler facility.

The basic idea is to generate high intensity beam pulses on a cold photocathode by shining a short-pulse high-power laser pulses on the cathode. The high intensity of the laser combined with the high accelerating field of the gun cavity allow the extraction of a very high current density from a small area, leading to a high-brightness electron beam. In addition, the photocathode's location in a high electric field allows immediate acceleration of the electrons to as high energy as possible, reducing emittance degradation due to the strong space charge force. Furthermore, the linear part of the space charge effects is compensated by applying a suitable external solenoid magnetic field, in

the technique known as emittance compensation. The last part of the injector is the merger system which combines the injected electron beam with the recycled high energy electron beams collinearly with the linac axis.

4.1.1 SRF Gun

The frequency of the gun will be 703.75 MHz, or the 75th harmonic of the 9.383 MHz bunch spacing frequency of RHIC II. To operate in CW mode with 50 mA current and 4.7 MeV kinetic energy beam the gun should supply about 250 kW power in to the beam. Low RF power losses in superconducting RF (SRF) gun and high peak electric field near the cathode followed by the emittance compensation scheme make SRF guns ideal injectors for high current low emittance applications.

There are various projects which right now are considering the use of SRF photo-injector. The first SRF gun developed with a successful insertion mechanism is Kernforschungszentrum Rossendorf (KFR) gun [2]. The gun operated successfully and demonstrated a peak electric field of 22 MV/m over the cathode area. It seems that in three to four years time the SRF Gun will become a routinly running injector for high current low emittances applications.

To keep the beam from the growing in size shortly after being emitted from the cathode, a focusing element in close proximity to the cathode is very desirable. A cathode recess provides an electric RF focusing near a cathode region where the space charge force is most significance. The 1½ cell gun shape with recessed cathode is shown on Fig. 4.1.2. A consequence of the cathode recess is that the accelerating field at the cathode is reduced by about a factor of two (Fig. 4.1.3.).

The performance of a SRF photo-injector has been studied using SUPERFISH (to calculate the electric and magnetic fields) by PARMELA [3] (to calculate the beam dynamics).

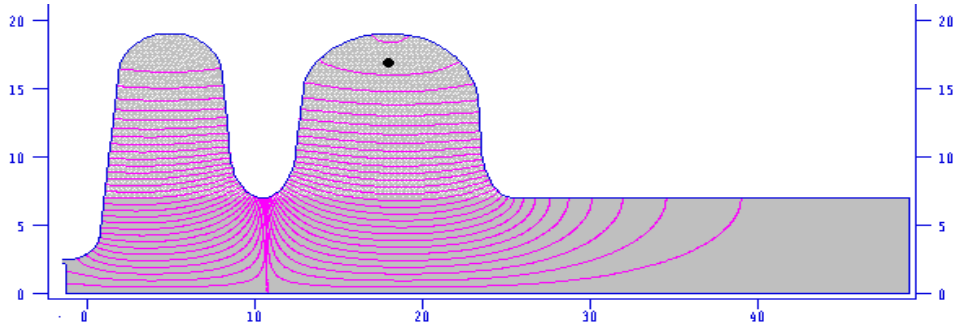

Figure 4.1.2: 1½ cell gun model with recess cathode was used by SUPERFISH.

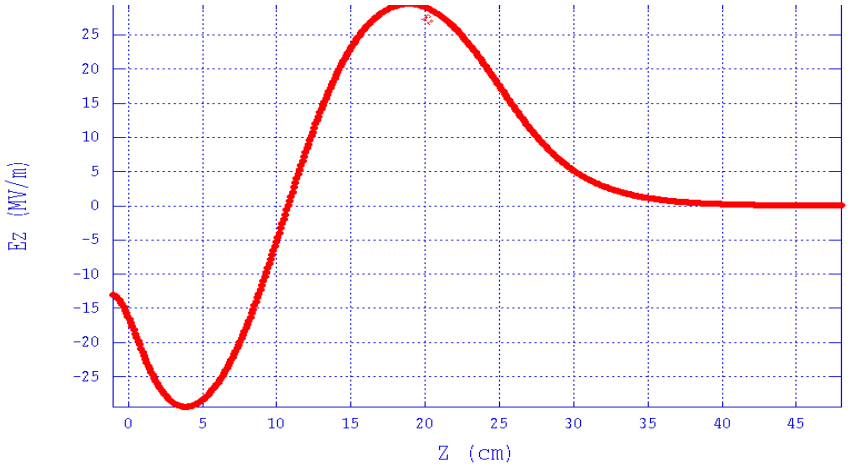

Figure 4.1.3: An electric field distribution for 1½ cell gun is calculated by SUPERFISH.

One important aspect of running the gun is the correct choice of its launch phase. The energy gain dependence on the initial phase (Fig. 4.1.4) shows that the crest point is at 42 degrees for this gun and this electric field. In order to minimize energy spread at the exit of the gun, a 35 degrees launch phase is chosen [4].

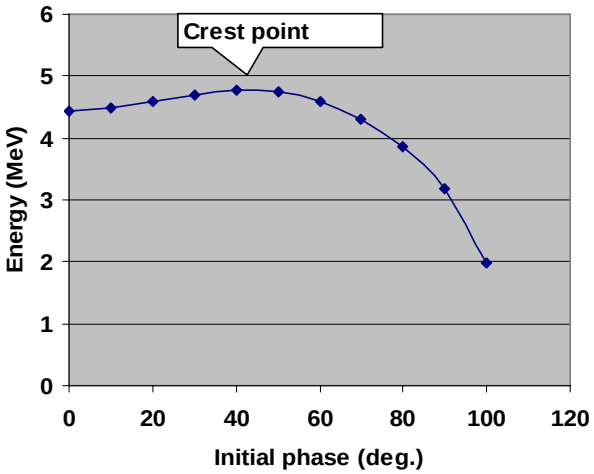

Figure 4.1.4: Energy gain from gun as a function of launch phase.

The longitudinal phase space at the exit of the gun is shown on Fig. 4.1.5. The parameters of the gun are presented in Tab.4.1.1.

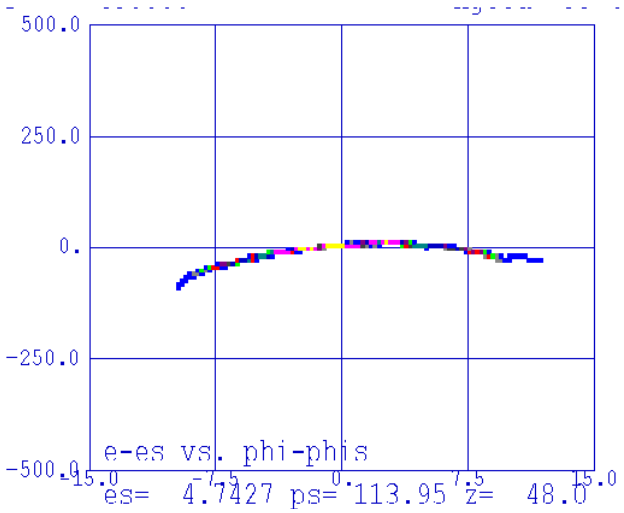

Figure 4.1.5: The longitudinal phase space after the gun for 5 nC electron bunch with elliptical initial distribution.

Table 4.1.1. 1½ cell SC Gun parameters

Frequency, MHz	703.75
Maximum field at the cathode , MV/m	14
Maximum electric field at the axis, MV/m	30
Maximum electric field at surface, MV/m	49.3
Maximum magnetic field at surface, A/m	76.8 kA/m
Initial phase, degrees	35
Charge/bunch, nC	5
Kinetic energy at the exit, MeV	4.7
Rms energy spread	$3.2\ 10^{-3*)}$
Normalized emittance $\varepsilon_x/\varepsilon_y$, mm mrad	$7.6/7.6^{*)}$

*) Result for elleptical beam initial distribution: maximum radius 6.2 mm and maximum length 71 psec. At his point, right after the gun, the emittance compensation did not take place, leading to a large emittance value.

4.1.2 Merger system

4.2.1.1 Achromatic merger at the presence of a strong space charge effects

One of the critical parts of the injection line is the merger of the low energy- and high energy beams (Fig. 4.1.6). As the low energy beam is strongly affected by space charge, the merger must be designed to minimize a degradation of this emittance. A typical system of this type has two properly spaced focusing solenoids are used for the emittance compensation.

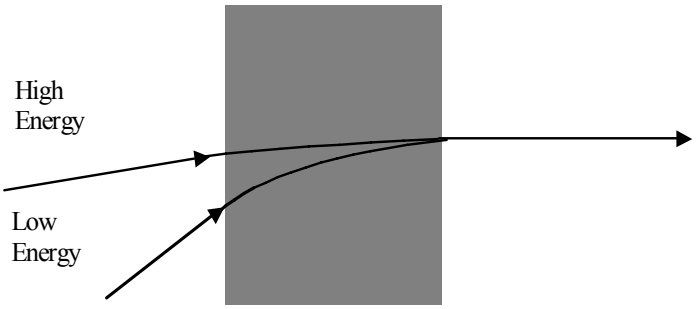

Figure 4.1.6: Main function of a merger – combining two (or more) beams with different energies

The injection energy is not recovered, it is just the ERL energy gain which may be recovered. Thus the use of a low injection energy permits a smaller investment of (unrecovered) power for gun and a low dumped beam energy. The original emittance compensation schema [5] does not include any dipoles between RF gun and linac (or booster cavity). Focusing of the bending magnets in the merging section has significant effect on the low energy electrons. Different focusing in vertical and horizontal planes (astigmatism) requires different distances to the linac, which is of course impossible. Hence, the use of chevron magnets with equal focusing strength in x- and y- direction is preferable. Any dipole magnet excites the coupling between energy and transverse motion which leads to effective correlated emittance growth, given by:

$$\varepsilon_x^{\,eff} = \sqrt{\varepsilon_x^{\,2} + \sigma_x^2 D'^2 \sigma_\delta^2 + \sigma_{x'}^2 D^2 \sigma_\delta^2}\,, \qquad (4.1.1)$$

where: D is the dispersion, D' is the dispersion derivative, ε_x is the emittance without the dispersion and $\sigma_x, \sigma_{x'}, \sigma_\delta$ are rms size, angular spread and energy spread respectively.

The full beam merging system has to decouple such correlations at the exit (i.e. full decupling of longitudinal and transverse motions). There are many systems which work very well in zero approximation (that is with no space charge effects and at a constant energy): chicane, dogleg, achromatic bend etc.

Basically it means that the achromatic system has to satisfy the two traditional conditions:

$$\begin{cases} \int_{s_o}^{s_f} K_o(s) \cdot m_{12}\left(s \middle| s_f\right) ds = 0; \\ \int_{s_o}^{s_f} K_o(s) \cdot m_{22}\left(s \middle| s_f\right) ds = 0, \end{cases} \qquad (4.1.2)$$

where $K_0(s)$-is curvature of trajectory, s_0, s, s_f - are initial, current and final positions respectively along the transport system $m_{12}(s|s_f)$, $m_{12}(s|s_f)$ – are (1-2) and (2-2) elements of 6x6 transport matrix from s to s_f position.

In the presence of strong space charge effects, the particles energy changes during its passage through the merger system. Then two additional conditions have to be satisfied [6]:

$$\begin{cases} \int_{s_o}^{s_f} K_o(s) \cdot s \cdot m_{12}\left(s \middle| s_f\right) ds = 0; \\ \int_{s_o}^{s_f} K_o(s) \cdot s \cdot m_{22}\left(s \middle| s_f\right) ds = 0. \end{cases} \qquad (4.1.3)$$

One of the possible merging schemes which satisfied both pairs of conditions and preserves the emittance of the low energy is shown in Fig. 4.1.7. This system provides a minimum set of elements (4 magnets) for correlations compensation. The beauty of zigzag system is demonstrated in Fig.4.1.8 where three different merger systems are compared. The vertical emittances for zigzag

merger, chicane and simple straight line with solenoids focusing instead of dipole focusing are the same. This illustrates that the effective focusing in these three systems is similar. However, only for the zigzag system the horizontal emittance (the plance where the dispersion is excited) equals the vertical emittance. The weak focusing by dipoles in this system is compatible with the emittance compensation technique where it is assumed that the electrons are moving laminarly (i.e. electron trajectories do not cross) [5]. For the dogleg system, because of its inherent strong focusing, there is no laminar electron motion any more, thus one of the important conditions for emittance compensation is broken. Even vertical emittance is much high than for the straight line system.

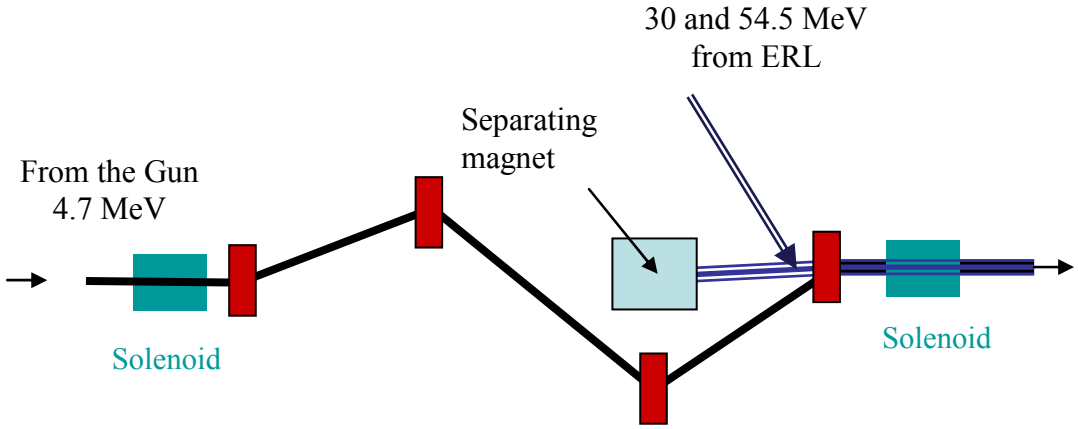

Figure 4.1.4. A merging system comprised of four chevron-type magnets, which is compensate the dispersion effects for space charge dominated beam.

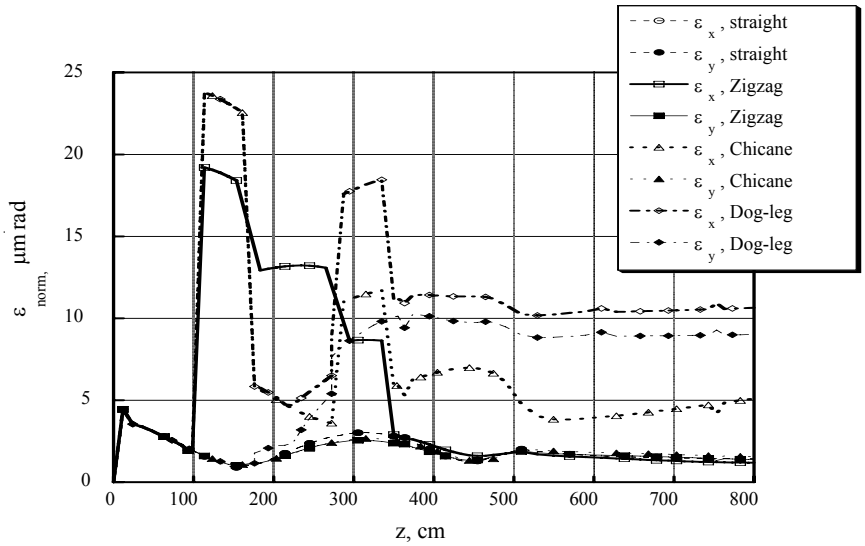

Figure 4.1.5. An evolution of horizontal and vertical normalized emittances in the four systems axially symmetric emittance compensation scheme, the Zigzag, the Chicane and the Dog-leg.

4.1.3 Beam dynamics for different initial laser shape.

In order to improve the performance of the beam (in terms of smallest emittance at a given bunch charge), we study three different types of laser driving pulse shapes (Fig. 4.1.9.). All distributions are uniform in transverse direction and have different longitudinal distribution.

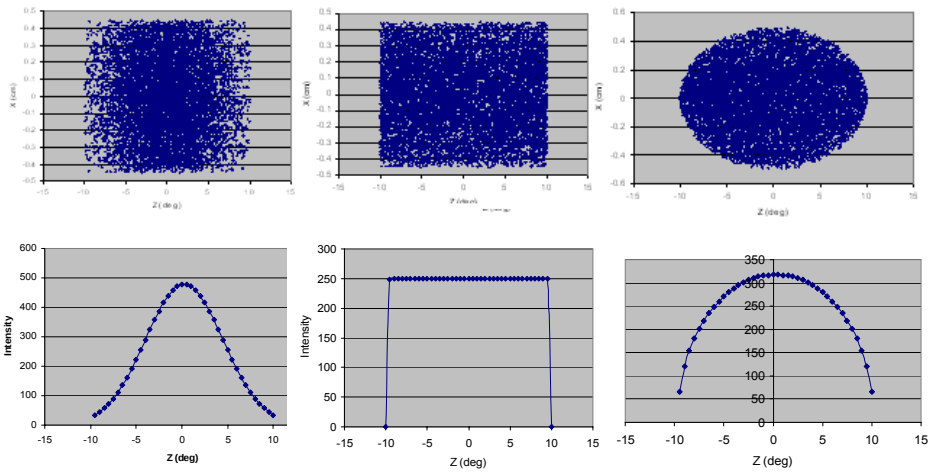

a) Gaussian b) Beer-can c) Elliptical

Figure 4.1.9: Three different initial laser shapes for beam dynamic simulation.

The first is a Gaussian distribution which characterized by rms length of 17 psec and a radius of 4.5 mm, the second is a so-called "beer-can" (or cylindrical uniform) distribution characterized by a full length of 92 psec and a radius of 5.5 mm, the last one is an elliptical distribution characterized by a maximum radius of 6.2 mm and a maximum length of 71 psec.

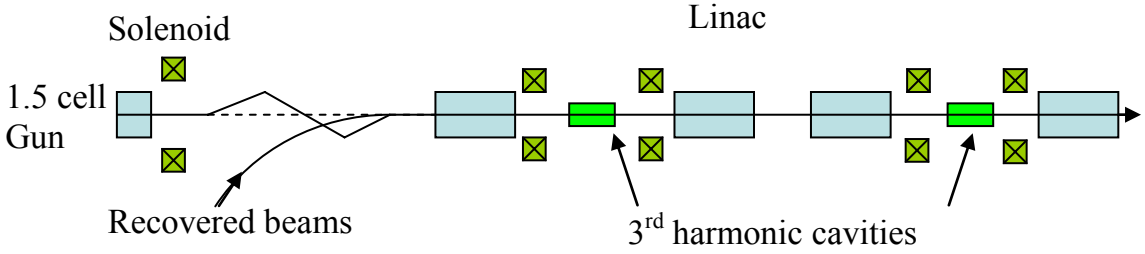

Figure 4.1.10: The test bed system for optimization injection part.

In order to save simulation time, a simple test-bed system was devised which skips the high-energy magnetic system of the ERL but concentrates instead on the low energy side, which includes all the merging and space-charge critical elements. The test-bed system consist of the full scheme injector (the object of study in this test-bed) followed by first pass through the linac and second time pass through the linac again without the return loop between the two passes (Fig. 4.1.10).
The normalized emittance evaluation in the test-bed system for beer-can initial distributions is shown on Fig. 4.1.11. The effective emittance jump caused by the dispersion exited by dipole magnet is well compensated by other dipole in the zigzag system. At the exit of the linac the horizontal normalized rms emittance is 3.1 mm mrad and the vertical is 2.8 mm mrad.
An energy spread evaluation is shown on Fig. 4.1.12 and Fig. 4.1.13. Simulation result for three distributions is summarized in Tab. 4.1.2.

Table 4.1.2. The parameters of the electron beam at the exit of the test-bed system

Distribution type	Gaussian	Beer-can	Elliptical
Kinetic energy , MeV	54.34	54.34	54.34
Charge per bunch, nC	5	5	5
Rms normalized emittance, $\varepsilon_x/\varepsilon_y$ mm·mrad	5.9/4.6	3.2/2.9	3.0/2.4
Rms momentum spread	$4\cdot10^{-4}$	$1.8\cdot10^{-4}$	$2\cdot10^{-4}$
Rms bunch length, cm	0.58	0.78	0.54

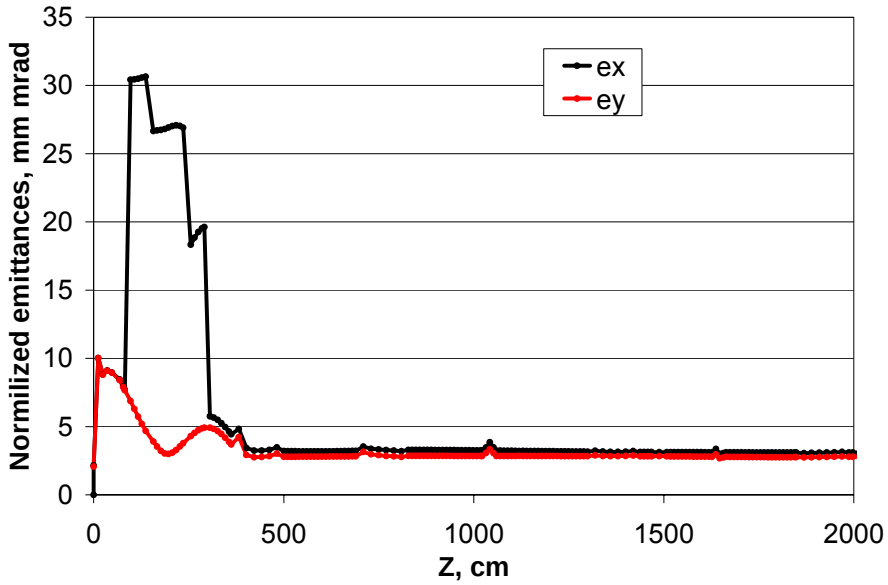

Figure 4.1.11: Evolution of the projected normalized transverse emittances rms in the test-bed system for beer-can distribution (final horizontal emittance 3.1 mm mrad, vertical emittance 2.8 mm mrad).

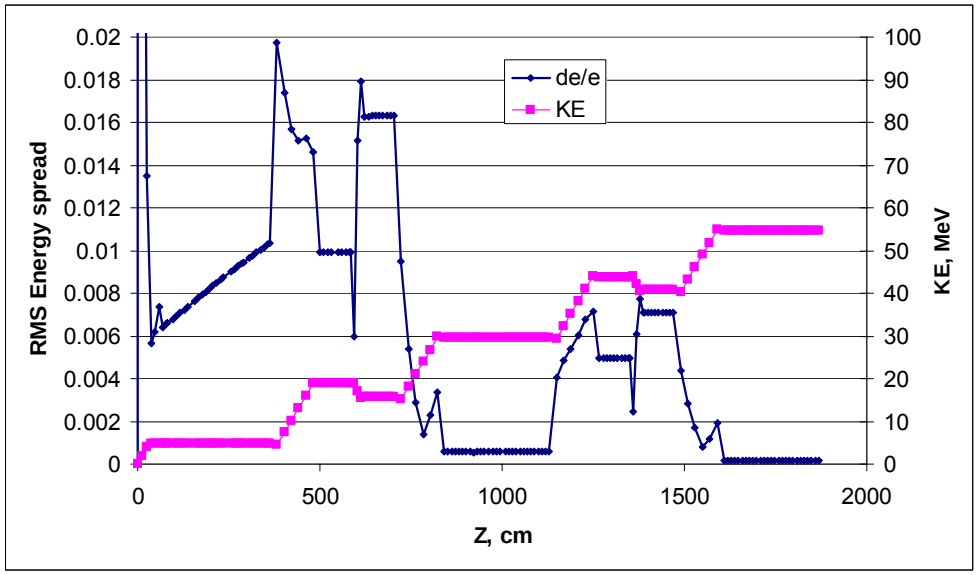

Figure 4.1.12: RMS energy spread and kinetic energy evolution in test-bed system for beer-can distribution. (final energy spread 1.6 10^{-4}, kinetic energy 54.3 MeV)

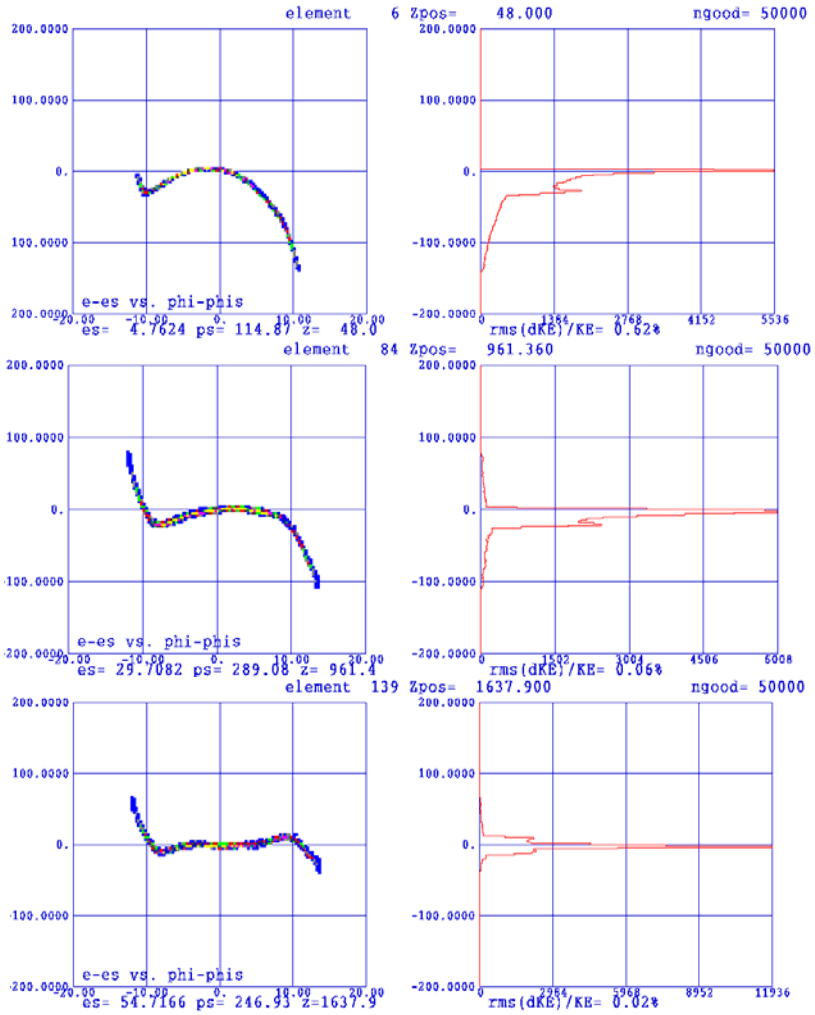

Figure 4.1.13: The longitudinal phase space at left side and energy spread at right at different locations. From the top to the bottom: after the SRF Gun, after first time acceleration up to 30 MeV, at final energy 54.3 MeV

4.1.4 Sensitivity to drive-laser beam parameters.

Some aspects of sensitivity of final electron beam parameters to the initial laser pulse parameters were done. The results show that for the chosen launch phase and for beer-can distribution the electron beam performance parameters stay nearly unchanged as various key parameters are scanned (Fig. 4.1.14).

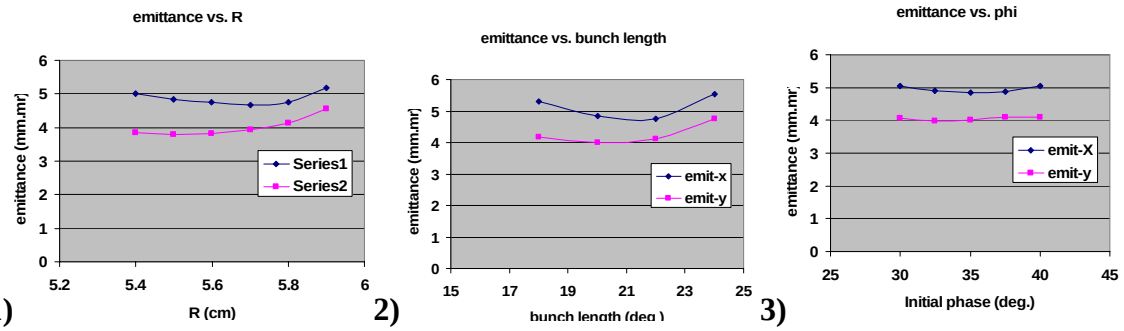

Figure 4.1.14: The dependence of final emittances on various laser beam parameters: 1) initial laser pulse length, 2) laser pulse radius, 3) laser launch phase

4.1.5 Further optimization

Code benchmarking and more optimization of the initial electron beam shape, RF phase and magnetic system of the injector are discussed in Appendix 4.A.1 and Appendix 4.A.2. The results of these optimizations are summarized in Tab. 4.1.3. It shows that the requirements for the cooler are met with conventional technology using a beer can distribution. With an emittance of 2 μ for the ideal machine there is a reasonable budget for the real world (misalignments, etc.)

A significant improvement is gained from using the tear drop shape. The emittance is reduced by 60 %. Alternatively, one can increase the bunch charge to 10 nC and reduce the cooling time by a factor of two. Figures 4.1.15 and 4.1.16 show the projected emittances as a function of path length from the cathode to the end of the linac.

Table 4.1.3: Normalized emittance as a function of particle distribution, cathode temperature and bunch charge.

Bunch shape	Bunch charge	Emittance horizontal	Emittance vertical	Energy Spread
Beer Can	5 nC	1.99 μ	2.07 μ	3.04e-4
	7 nC	3.45 μ	3.96 μ	3.11e-4
	10 nC	5.07 μ	5.14 μ	3.07e-4
Tear Drop	5 nC	1.03 μ	1.00 μ	1.48e-4
	7 nC	1.62 μ	1.73 μ	1.55e-4
	10 nC	2.29 μ	2.75 μ	1.72e-4

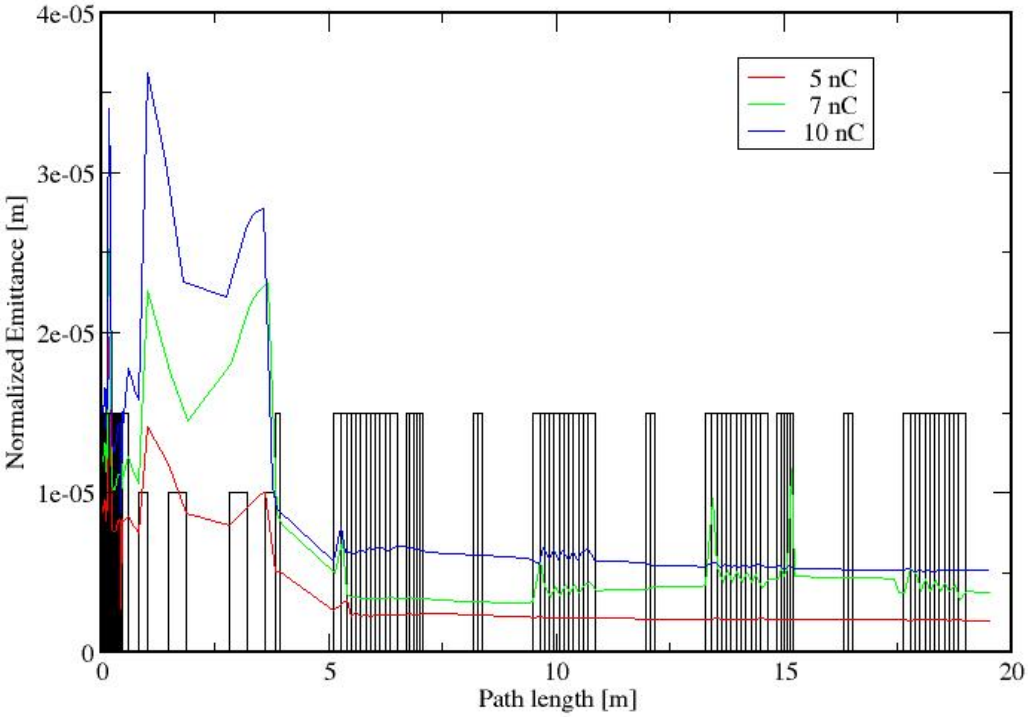

Figure 4.1.15: Projected emittances for the Beer Can distribution. Shown is the square root of the 4-D emittance.

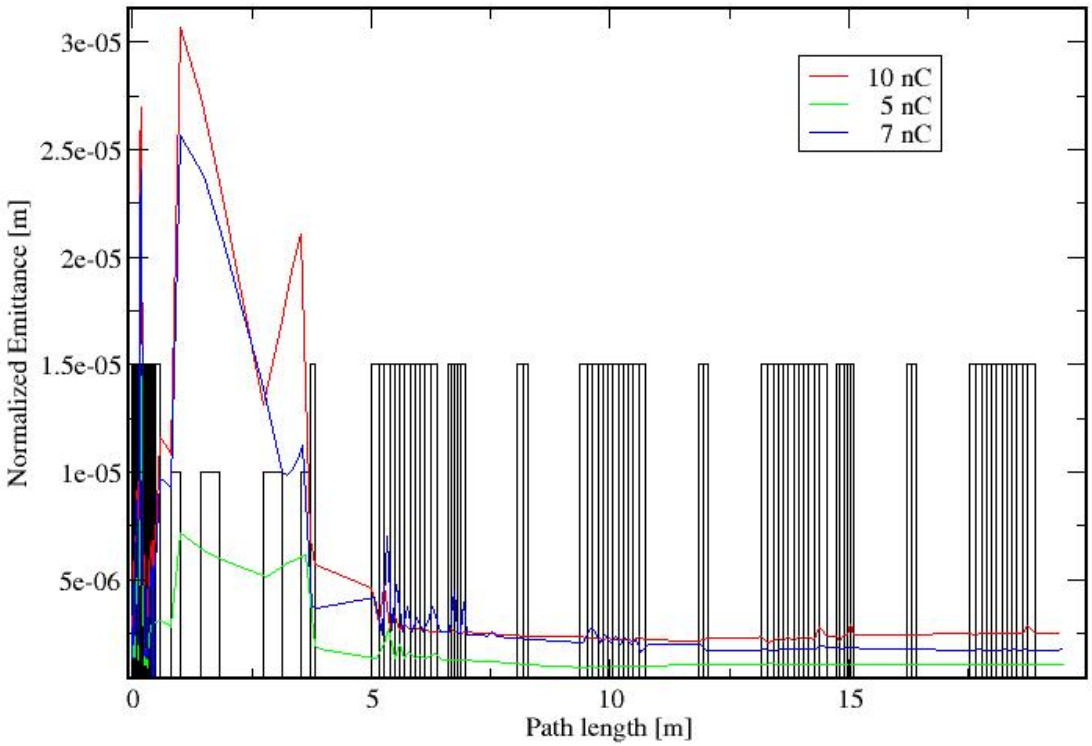

Figure 4.1.16: Projected emittances for the Tear Drop distribution. Shown is the square root of the 4-D emittance

4.1.6 Halo

Due to he non-linear forces the beam develops a halo as it is accelerated through the linac. This is especially true for the beer can distribution where the space charge forces in the head and the tail are strongly non-linear. These halo particles are often far outside the core of the bunch. These particles do not contribute to the cooling of the ion beam, but they do not do any harm either, as long as the action of these particles is smaller than the ion emittance and they are not scraped. However, they contribute strongly to the RMS emittance.

It makes therefore sense to ignore these particles in the emittance compensation. For that purpose a post-processing program was written, that reads the particle distribution at the linac exit from the PARMELA binary output and removes particles with large action.

The program first calculates the Twiss parameters for the bunch and than the particle action for each particle. It removes 1% of the particles with the larges action. This changes the Twiss functions. The process is iterated until the specified amount of particles is removed. Figure 4.1.17 illustrates the successive removal in the x-x' space.

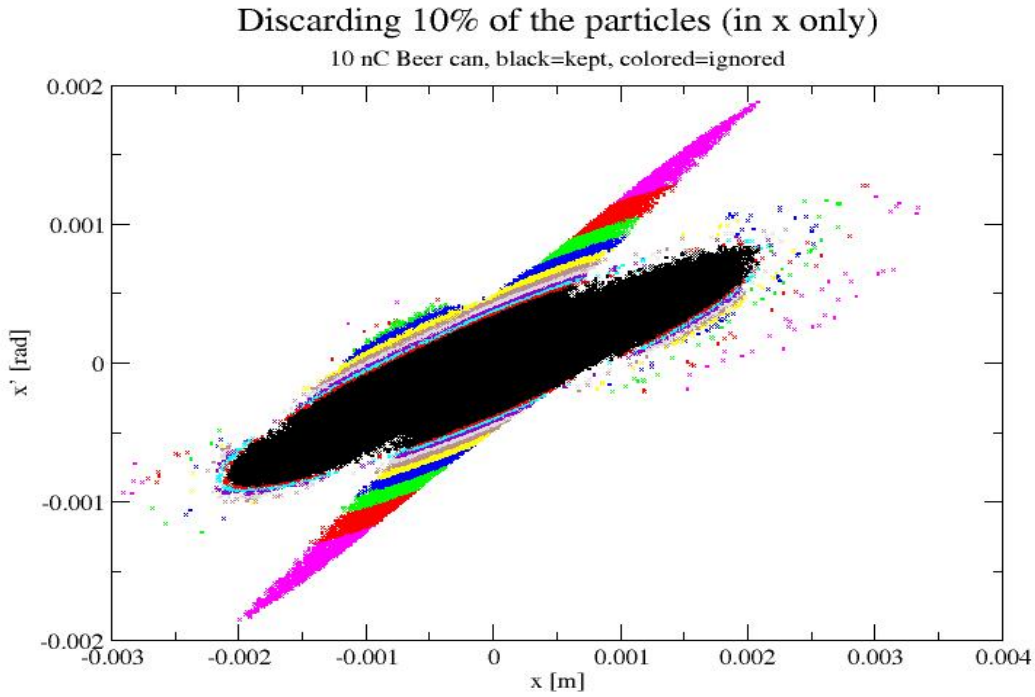

Figure 4.1.17: Successive removal of the halo

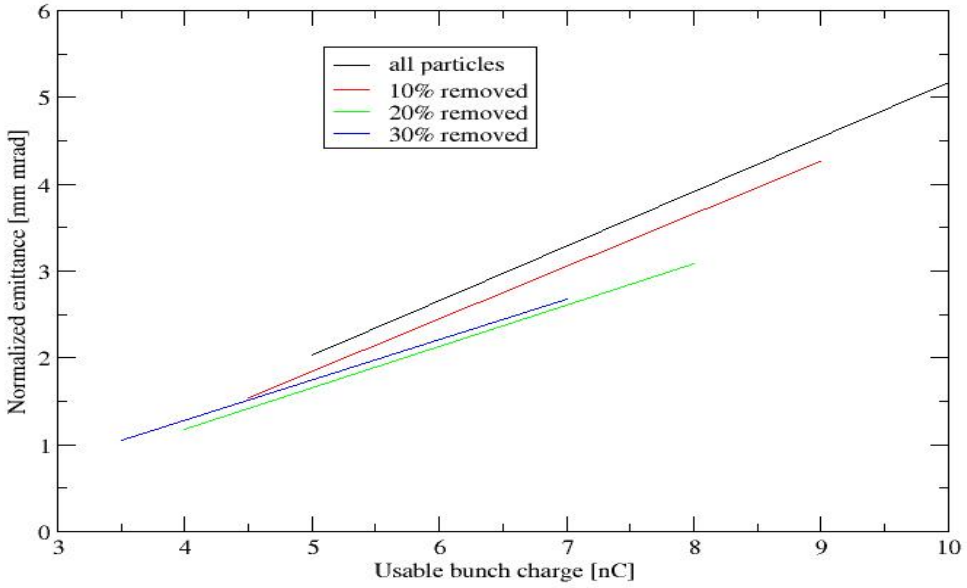

Figure 4.1.18: Emittance after removal of large action particles for the beer can distribution with 0.1 eV transverse temperature. Removing more than 20% does not help since the remaining charge decreases proportional to the emittance.

The improvement resulting from this method is illustrated in Fig. 4.1.18. The idea is to increase the bunch charge by some percentage and then ignore that percentage of particles with the largest

actions. The effective emittance is plotted as a function of the usable charge for different amount of extra beam. A large improvement comes from the first 20%, above that is no improvement.

4.1.7 Conclusion

We have demonstrated a design of the electron cooler injector that fulfills and exceeds the requirements of the RHIC electron cooler. Using a tear drop distribution the bunch charge can be doubled to 10 nC, which will reduce the cooling time for RHIC accordingly. Using a beer can distribution the increased bunch charge will be still beneficial, since the halo particles created by the distribution are harmless.
We have also gained some confidence in the simulations by carefully exploring the space charge integration parameters and benchmarking the PARMELA results with other space charge tracking programs.
Finally, we have created a powerful optimization tool by combining PARMELA with the CONDOR [17] optimizing package and devised an optimization strategy to obtain low emittance beams.

4.2 Twin Loop Energy Recovery Linac

4.2.1 General ERL layout

The schematic layout of a two pass ERL for the RHIC electron cooler is shown on Figure 4.2.1. The two=pass system reduces the cost of the ERL. The superconducting RF (SRF) Gun (1) produces 5 nC 4.7 MeV electron beam. The beam goes through the injection channel (2) comes into SC RF Linac (3) to be accelerated first time up to 30 MeV. The 30 MeV beam makes two achromatic 180 degrees bends (4, 4') and returns to the linac (3) a second time to get acceleration to 54.5 MeV. The 54.5 is transported to the RHIC (5) for cooling ion beam in both rings (see VII). The used 54.5 MeV electron beam is returning back (6) into the linac (3) in a deceleration phase. After the first deceleration to 30 MeV the beam goes through the same two 180 degrees achromatic bends (4, 4') again. In the last pass through the linac the beam gives back the rest of the energy to cavities and goes to the beam dump (7) at the injection energy of 4.7 MeV.
The decelerating beams deposit into the SRF linac the same amount of energy as that taken by the accelerating beams. Therefore, the RF power required to operate the SRF linac is very low and is at few watts level. We plan on using 50 kW RF transmitters for operating the SRF cavities mostly to improve the stability of the system for reactive power load fluctuations caused by microphonics, however a fast tuner system under consideration may reduce this power substantially.

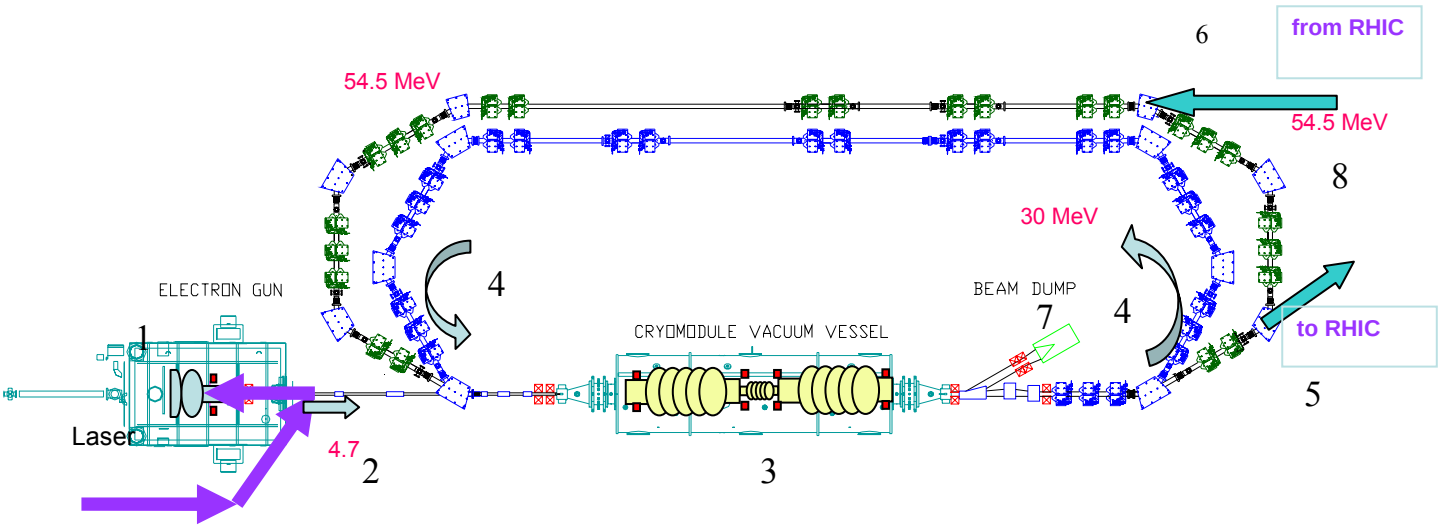

Figure 4.2.6: Schematic layout of the two-pass ERL for the RHIC electron cooler facility: 1) SC RF gun, 2) injection channel, 3) SC RF linac, 4) and 4') 180 degrees achromatic bends, 5) and 6) transport channels to- and from- RHIC, 7) beam dump, 8) short-cut.

4.2.2 Twin-pass magnetic system

Each 180 degrees bends of the first loop (Fig 4.2.1) (4) and (4') consists of three 60 degrees dipole magnets with three independent quadrupole magnets between them. The quadrupoles between the dipoles makes the bends achromatic and isochronous. Nine quadrupoles in the dispersion-free straight section provides for matching of the β-function and for choosing the desirable phase advances independently in the horizontal and vertical planes. At relatively high energy 30 MeV and above, space charge effects on the beam dynamics become very small. In first approximation a linear matrix approach can be used for the layout design and for matching the electron beam from the linac to the return loop. The MAD output lattice functions for first pass from linac exit to next entrance to the linac are shown on Fig. 4.2.2.

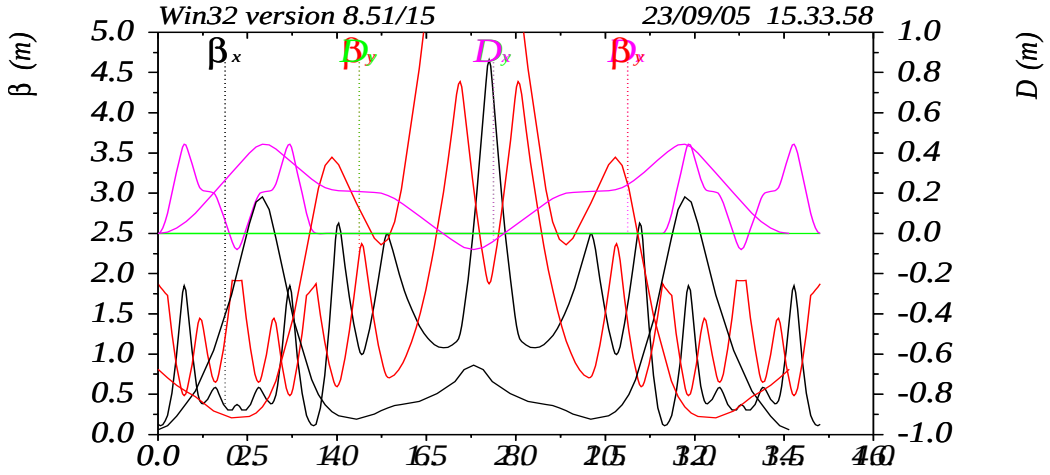

Figure 4.2.2: The beta functions and dispersion evaluation in the first loop.

Dispersion in the bends is always smaller than 0.5 m. There is a dispersion free section between the two 180 degrees bends. A zero longitudinal dispersion of the whole loop makes the longitudinal motion in first order very simple.

The present design of a second loop lattice has a short-cut (8) (Fig. 4.2.1) to drive electron beam directly to the linac in a decelerating phase without reaching the cooling region. This short-cut will be used for independent tests of the ERL without interference with RHIC operation. The energy of the electrons at the second loop is 54.5 MeV and effects of the space charge can be neglected even more. The lattice functions for second loop from linac exit at 54.3 MeV energy to entrance in decelerating phase to the linac again are shown on Fig. 4.2.3.

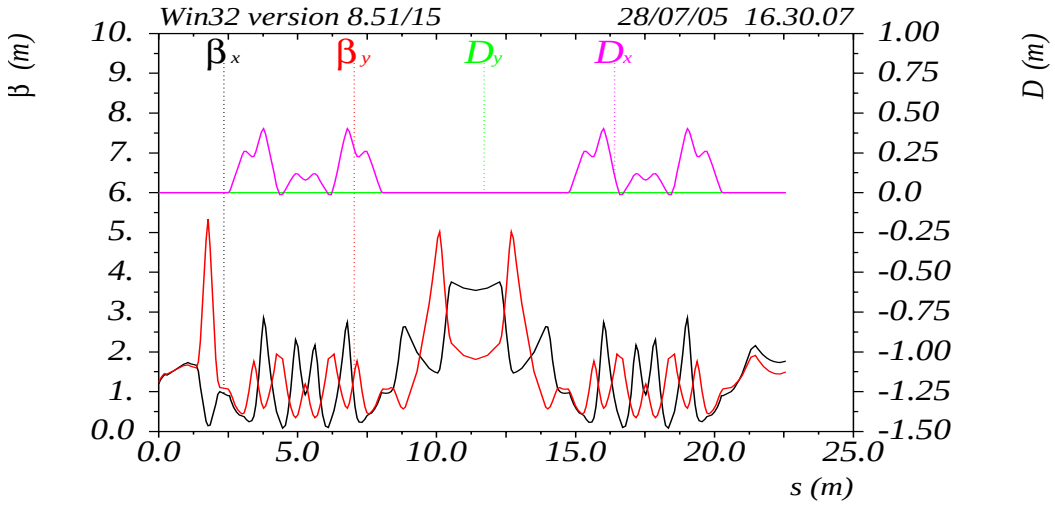

Figure 4.2.3: The beta functions and dispersion evaluation in the second loop short-cut.

There is also a dispersion free section between two 180 degrees bends where the beam will be accurately studied before sending it to the electron cooling section of RHIC.

4.2.3 Transport line to RHIC

After reaching the energy of 55 MeV the electron beam follows a transport line to the RHIC cooling section. The transport line consists of similar quadruples and dipoles (Fig. 4.2.4.) magnets which guide the electron beam to RHIC and back. Quadrupoles provide matching beta functions from ERL and cooling section and make dispersion zero in cooling section.

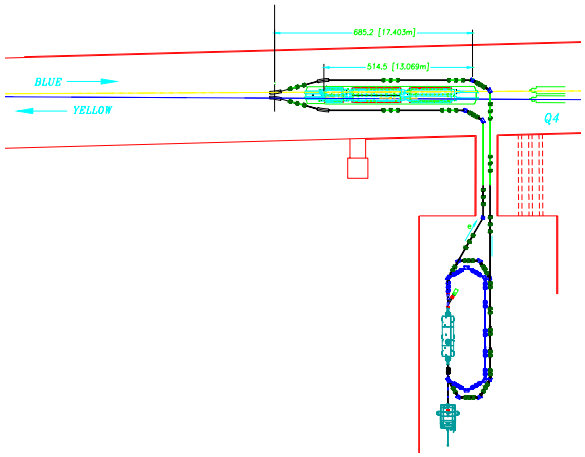

Figure 4.2.4: Layout of a transport line from ERL to RHIC and back.

4.2.4 Matching two rings

The studies of electron beam performance degradation after one pass through cooling section in one ring shows that emittance could grow less than 1 % (see below section 4.4). The electron beam emittance and energy spread are still good enough to reuse the beam for cooling of the ion beam in the other RHIC ring. This feature leads to a considerable cost saving, eliminating the need for a second ERL. To keep the parameters for electron cooling at optimum, the electron beam should be well matched between two rings. The transport line from one ring to the other should satisfy the following requirements:

- beta functions should be matched with beta functions in cooling sections 500 m (Tab. 3.1.2 electron beam requirements);
- full transit time from the center of the cooling section in one ring to the center of the cooling section in the other ring should be an integral number of ion beams periods, 1/9.383 MHz = 106.6 nsec.

The schematic layout of the two rings matcher is shown on Fig. 4.2.5. The region there the matcher could be installed is limited by the sizes of RHIC tunnel and necessity to bypass of matching RHIC superconducting triplet. In present design the electron time trip from center of yellow ring to center of blue ring is 3 distances between bunches. The chosen path length is allowed to cool successfully RHIC not only for 120 bunches operation but for 180 bunches as well.

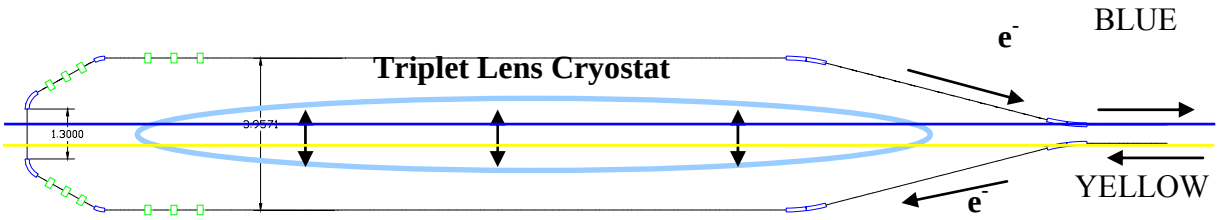

Figure 4.2.5: Two ring achromatic matcher. Blue boxes are dipoles and green boxes are quadrupoles.

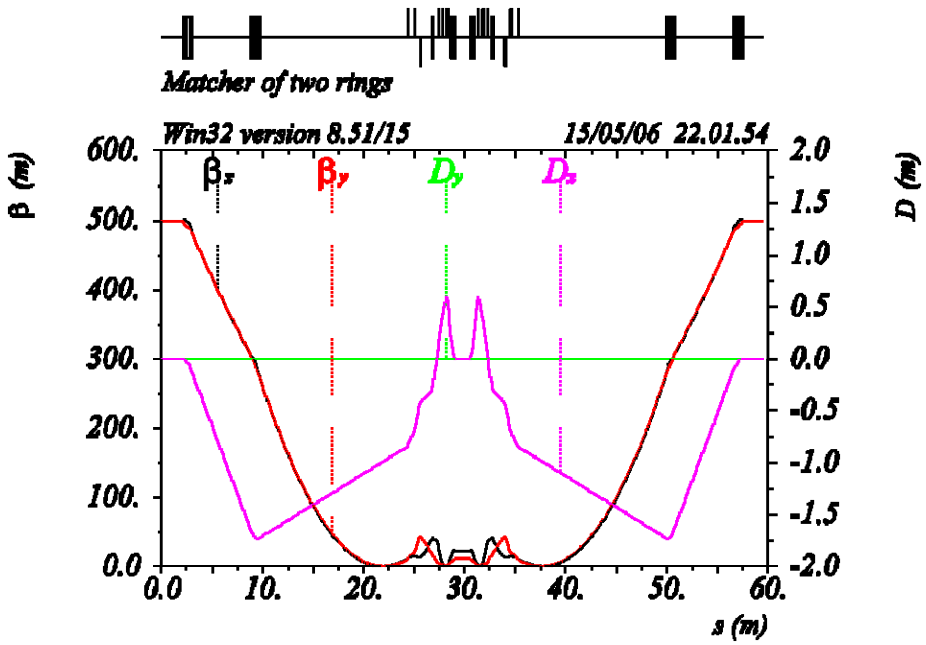

Figure 4.2.6. Beta-function and dispersion in the matching section of the two rings.

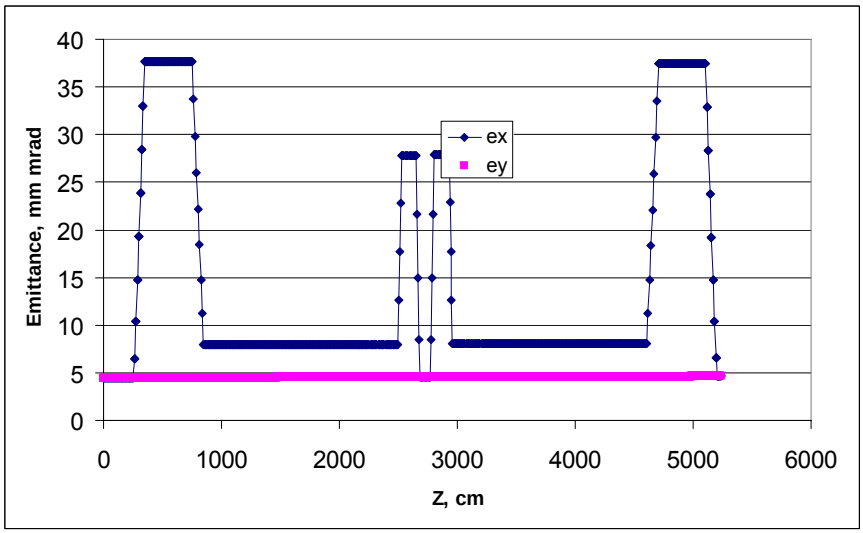

Figure 4.2.7. Normalized emittances evolution in the matching section of the two rings.

The beta function in the rings is 500 m, thus to avoid large beta function oscillations, weak chevron 15 degree 4 m radius dipoles extract and return the electron beam to and from ion beam trajectory. Before making the 180 degree strong focusing turn, a simple beam-optical telescope is used. The system has a zero dispersion region near an intersection of electron beam vacuum chamber and RHIC ion vacuum chamber. The beta function and dispersion are shown on Fig. 4.2.6. To avoid vacuum chamber intersection a small vertical tilt of all electron beam trajectory can be used but in this case the vertical dispersion has to be taken to the account.

The effective horizontal emittance growth because of nonzero dispersion region is shown on Fig. 4.2.7. However the emittance returns back to its original value after beam completes its return back to RHIC ring.

One of the interesting scenarios of the cooler operation is to double the repetition rate of the electron beam and change the loop delay time from 3 ion bunch spaces to 3.5 spaces. In this scenario odd electron bunches will interact only with blue ring ions and the even bunches will interact only with yellow beam ions. This mode provides a backup plan in which each ring is cooled by a fresh electron beam. The price paid is the doubling of the average electron beam current.

4.2.5 Start-to-end simulation.

For the large beta functions in the cooling section, the space charge force can effect on the beam dynamics even at an energy of 55 MeV. The evolution of the electron beam parameters under these conditions was studied using optics calculated by MAD8 (Fig. 4.2.2, Fig. 2.2.3).

Results of start to end simulation of the two-pass ERL are shown in Fig. 4.2.8 and Fig. 4.2.9. The initial electron beam distribution is a beer-can, with full length of 92 psec and a radius of 5.5 mm. Beam parameters at the cooler work energy are shown in Tab. 4.2.1.

Table 4.2.1: The parameters of the electron beam at the working energy for electron cooling of gold ions.

Type of distribution	Beer-can
Kinetic energy, MeV	54.34
Charge per bunch, nC	5
Rms normalized emittance, ex/ey mm·mrad	3.0/3.2
Rms momentum spread	$3.6 \cdot 10^{-4}$
Rms bunch length, cm	0.78

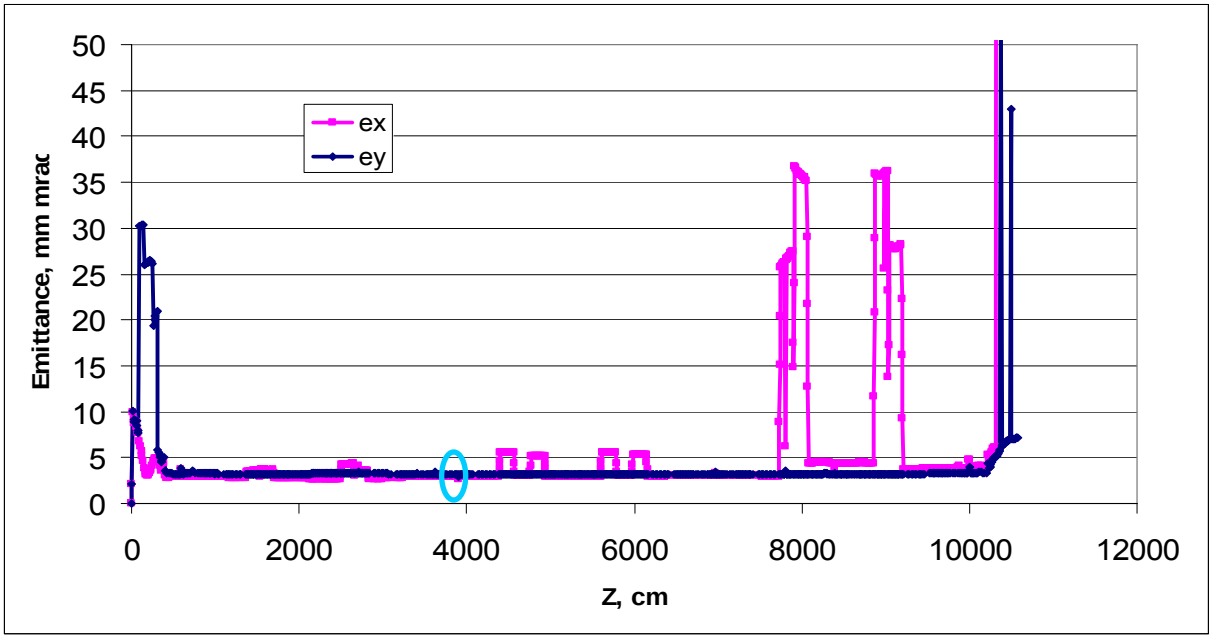

Figure 4.2.8: Normalized emittances evaluation in two passes ERL for electron cooler for beer-can distribution. (e_x/ε_y= 3.0/3.2 mm mrad at kinetic energy 54.3 MeV). The cyan circle points to the location of the cooling section

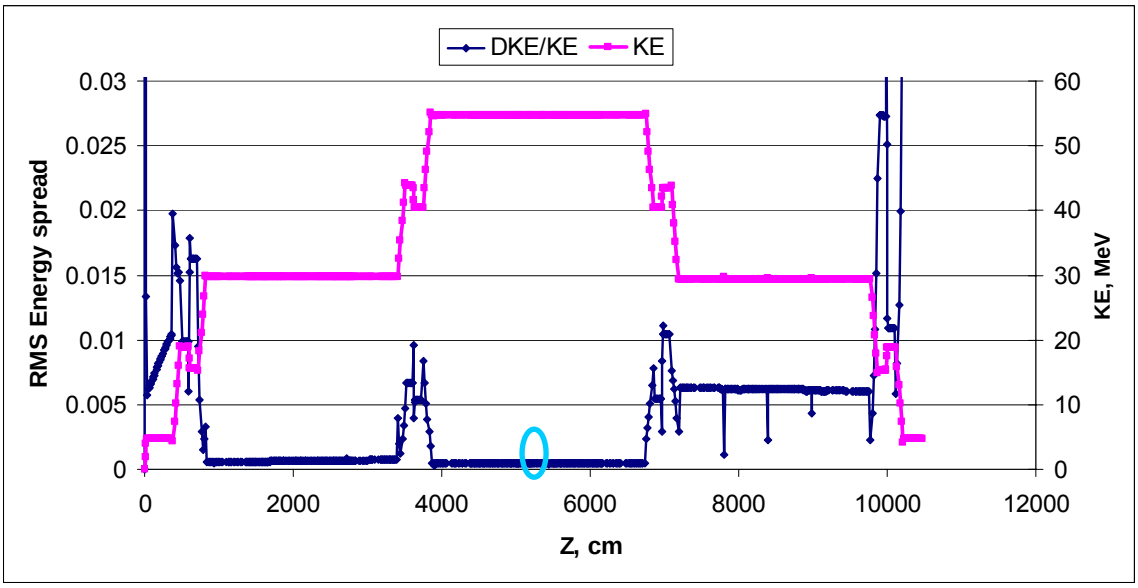

Figure 4.2.9: RMS energy spread and kinetic energy evolutions in the two-pass ERL for electron cooling for a beer-can distribution. (energy spread 3.6 10^{-4} at kinetic energy 54.3 MeV). The cyan circle points at the location of the cooling section

4.3 Cooling section.

4.3.1 General layout

The cooling section is the region there the electron beam and ion beam overlap to produce the cooling action. This part of the system is the longest one in the electron system yet the electron beam must maintain its peak performance all along this section. Details of the cooling performance are discussed in chapter 3.

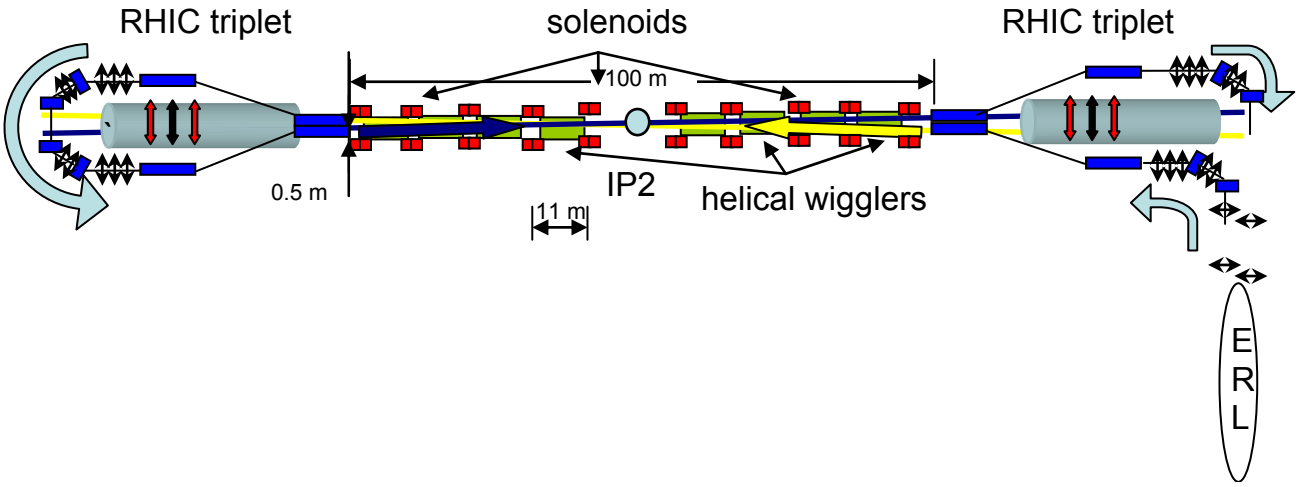

Figure 4.3.1: Schematic layout of RHIC cooling section. Each electron beam cools ions in yellow ring then in blue ring.

The large beta function (large size and small angular spread) 500 m in cooling section is required for the optimized cooling rate (see chapter 3.5). The schematic layout of the cooling section is shown in Fig. 4.3.1. The electron beam beta function is blown up to 500 m and the electron beam is merged precisely with the ion beam. The blue and yellow cooling sections consist of 11 m sub-sections. Most of cooling section is covered by helical undulators. The helical undulators in the cooling section are used to suppress recombination of the heaviest ions (gold and above, see details in chapter 3.4). Some space is taken up by closely spaced steering dipoles and beam position monitors used to keep the electron beam and ion beam in close relative alignment, and pairs of solenoids are used to compensate the effects of space charge defocusing. The schematic layout of a single 11 mm structure is shown in Fig. 4.3.2.

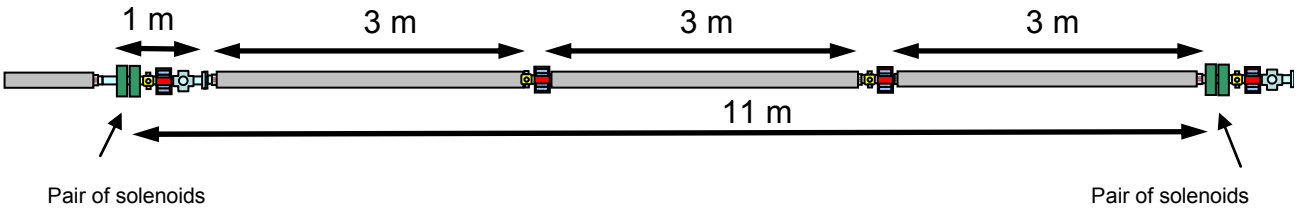

Figure 4.3.2: The schematic layout of 11m structure consisting of 3x3m helical wigglers, 3 steering dipoles, pair of solenoids, vacuum equipment and instrumentation line.

4.3.2 Space charge effects

Compensation of transverse defocusing

In the presence of space charge forces and external focusing, the envelope equation of a round beam is as follows:

$$\sigma'' - \frac{\varepsilon_n^2}{(\gamma\beta)^2\sigma^3} - \frac{I}{2(\gamma\beta)^3 I_0\sigma} + K_{sol}\sigma = 0, \qquad (4.3.1)$$

where $\sigma_x=\sigma_y=\sigma$ is rms size of the round beam, I is the peak current, $(\gamma\beta)$ is the relativistic factor, $I_0=14$ *kA* is the van Alfven current, ε_n is normalized emittance K_{sol}- is the strength of an external solenoid field if any of these exist. For the cooler parameters of the electron beam in cooling section $I=60A$, $(\gamma\beta)=107$, $\varepsilon_n = 4\times10^{-6}$ m, $\sigma=4.3\times10^{-3}$m (see Tab. 3.1.2.) The space charge term is 25 times larger than the emittance term. Thus the beam dynamics in cooling section is dominated by space charge effects.

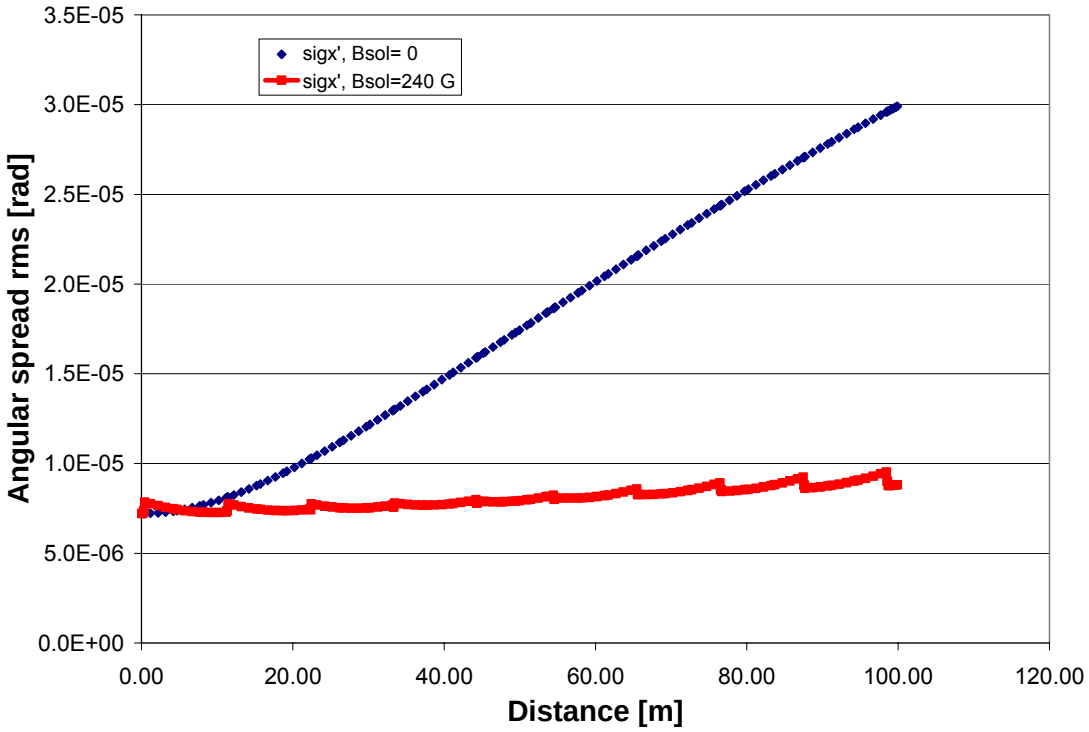

Figure 4.3.3: Evolution of angular spread rms in 100 m cooling section. (blue line - without solenoids, red line with solenoid B=240 G).

The absolute value of electron beam self space charge defocusing strength is $7.8\cdot10^{-5}$ m^{-2}. Even such a small defocusing strength leads to an angular spread of $3\cdot10^{-5}$ which is 3 times bigger than allowed for cooling. For compensation of the space charge defocusing and keeping the angular spread in the allowed range, the cooling section is fitted with pairs of solenoids (running in opposite magnetic field) every 11 m.

Solenoid focusing strength is given by:

$$K_{sol} = \left(\frac{eB}{2mc^2\gamma\beta}\right)^2, \qquad (4.3.2)$$

where mc^2 is an electron energy in a rest frame, B is magnetic field , e is the charge of an electron. To compensate effect of a space charge with the 20 cm long solenoid in each 11 meters one needs a modest magnetic field of 240 G. The result of the electron beam propagation along the cooling section with and without these solenoids is shown in Fig. 4.3.3.

Energy spread growth

According to the simulations, the space charge induced energy spread satisfies cooling requirements even if effect of image charge is not included. Additionally, an image charge on the vacuum chamber reduces the growth rate of the energy spread dramatically. Figure 4.3.4 shows bunch energy spread growth induced by longitudinal space charge after 100 m long cooling section simulated by PARMELA.

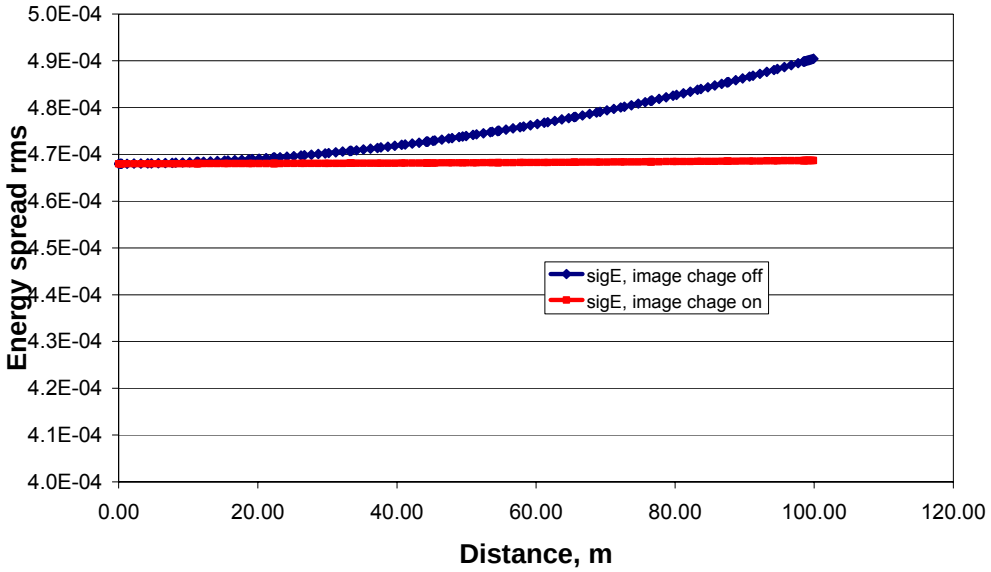

Figure 4.3.4: Evolution of an energy spread rms in 100 m cooling section. (blue line - without image charge, red line - with image charge on.)

4.4 Collective Effects

The effects of the beam space charge in the cooling section were discussed in section 4.3.2. In this section, we consider other effects which depend on the beam intensity that can affect quality of the electron beam. These effects include the multi-pass beam breakup, effects of short range wake fields produced by the beam electromagnetic field interacting with accelerator components, Coherent Synchrotron Radiation (CSR), ion trapping in the ERL, electron cloud in the cooling section, effects of image charges, and Intra-Beam Scattering (IBS).

4.4.1 Multi-pass Beam Breakup (BBU)

Multi-pass BBU arises from the interaction of an intense recirculated beam with dipole higher-order modes (HOM) of the accelerating structures and can present an insurmountable problem for operations of a multi-pass machine. The design of the 5-cell SC BNL cavity was optimized to reduce the quality factor of HOMs and push BBU threshold beyond the ampere level. Both numerical simulations using the code MAFIA and preliminary measurements with the copper model

show that the ferrite absorbers situated next the five cell cavity set the quality factor of dipole HOMs to the range of 10^2-10^4. These numbers are two to four orders of magnitude lower than the quality factor of dipole HOMs of the JLAB FEL 7-cell cavity with the BBU threshold of approximately 2.5 mA.

Multi-pass BBU in the e-cooler ERL was simulated using codes GBBU [7] and TDBBU [8]. The *Q* and *R/Q* values of dipole HOMs were simulated by MAFIA. To study the dependence of the BBU threshold on ERL parameters the recirculation time and the recirculation matrix of each loop were varied within a "reasonable" range. Additionally, the threshold was simulated for ten different random seeds of dipole HOM frequency. In each case, the frequency of each HOM was generated randomly with a Gaussian distribution with an r.m.s. width of 3 MHz around the central frequency calculated by MAFIA. In most of these simulations, the BBU threshold was between 2.5 and 5 Amps. The minimum threshold current observed in these studies was 1.5 A which is still well above 50 mA, nominally required for cooling. The maximum threshold current observed in these simulations was 8.6 A.

4.4.2 Short-range wake fields

Interaction of the beam electromagnetic field with beam surroundings can induce electric and magnetic wake fields causing beam quality degradation. In this sub-section, we will consider an effect of short-lived, high-frequency fields with the decay time shorter than the time gap between bunches: the resistive wake, interaction with accelerating cavities, etc. (BBU considered in section 4.1 is an example of the long-range wake field effect.) Additionally, we separate the short-range wake field effects in those affecting the energy spread, also referred to as longitudinal effects, and those affecting the transverse motion.

4.4.2.1 Longitudinal effects

Interaction with accelerating cavities

Interaction of the electron beam with the 5-cell SC BNL cavity was simulated by R. Calaga using the code MAFIA [9]. In his dissertation, Calaga has calculated the loss-factor $k_{\|}$ which is equal to the cavity voltage induced by a bunch normalized to the bunch charge. The loss factor includes the effect of both long-range wakes (low-frequency HOMs) and short range wakes (high frequency fields above the pipe cut-off.) Energy lost by a particle within a bunch is a convolution of the wake function with the charge distribution ahead of the particle. Thus, particles in the head of the bunch lose almost no energy while tail particles experience the maximum energy loss. Therefore, the energy spread induced within a bunch after passing a cavity is roughly equal to the energy lost by a bunch:

$$\sigma_{\delta E/E} \approx \frac{q_b(pC)k_{\|}(V/pC)}{\Delta E(V)}, \quad (4.4.1)$$

where ΔE is the cavity accelerating voltage. For the electron cooler, the loss factor $k_{\|}$ is 1.12 V/pC, the bunch charge q_b is 5 nC (=5000 pC), and the energy gain per cavity is approximately 12.5 MeV. For these parameters, the energy spread is

$$\sigma_{\delta E/E} \approx 4.2 \cdot 10^{-4}. \quad (4.4.2)$$

Note that the number given by (4.4.2) is the energy spread induced after a single cavity. The energy spread at the end of acceleration will be equal to this number only if the ERL recirculation pass is exactly isochronous. Otherwise, the energy spread at the end of acceleration will be smaller.

The energy spread given by (4.4.2) does not exceed the specified $5\cdot10^{-4}$, required for cooling. Additionally, one can suppress the energy spread by a factor of few or more by a judicial choice of accelerating phase if this is required.

Resistive wake

The resistive wake is the effect arising from interaction of the bunch electromagnetic field with a resistive vacuum pipe wall. In this sub-section, we estimate the energy spread growth due to interaction of the beam field with a stainless steel pipe in the 100 m-long cooling section.

The wake function of the resistive wake is given by [10]

$$w(z)=\frac{16L}{b^2}\left[\frac{1}{3}\exp\left(\frac{z}{(2\chi)^{1/3}b}\right)\cos\left(\frac{\sqrt{3}z}{(2\chi)^{1/3}b}\right)-\frac{\sqrt{2}}{\pi}\int_{-\infty}^{0}\frac{x^2\exp\left(\frac{zx^2}{(2\chi)^{1/3}b}\right)}{x^6+8}dx\right], \qquad (4.4.3)$$

where L is the cooling section length equal to 100 m, b is the beam pipe radius equal to 35 mm, and χ is the dimensionless parameter equal to $c/(4\pi\sigma b)$ where c is the speed of light and σ is the conductivity of stainless steel, 1.3e16 sec^{-1}.

The energy loss by a particle at a distance ξ from the beginning of a bunch with a rectangular charge distribution is given by

$$\delta E(\xi)=-\frac{N_e e^2}{l_b}\int_{\xi}^{1/2} w(\xi-z)dz\,, \qquad (4.4.4)$$

where l_b is the bunch length, N_e is the number of electrons in a bunch, and e is the elementary charge. For the electron cooler parameters (5 nC charge-per-bunch and l_b=3.4 cm), the r.m.s. energy spread produced by the resistive wake after 100 m and the average energy loss by beam particles are respectively:

$$\left(\frac{\sigma_E}{E}\right)_{RW}=4.5\cdot10^{-5}$$

$$\left\langle\frac{\delta E}{E}\right\rangle_{RW}=-3.8\cdot10^{-5}$$

These numbers are more than an order of magnitude smaller than the requirement on the energy spread in the cooling section.

Interaction with bellows and other contributions

Numerical simulations of wake fields produced by such vacuum system components as bellows and pumping ports still have to be conducted. However, we do not expect large contributions to the energy spread from those components. Simplistic estimates using the short, shallow, broad band cavity model [10] applied to bellows with 10 convolutions of a cross-section area of 0.5x0.5 cm^2 yielded an additional normalized r.m.s. energy spread of the order of $5\cdot10^{-7}$.

4.4.2.2 Transverse effects

Interaction with accelerating cavities

The average transverse deflection voltage induced by transverse wake fields can be defined using the "transverse kick factor", $k_\perp$, as

$$c\frac{\delta p_\perp}{e}(V) = q(pC)x(m)k_\perp(V/pC/m), \qquad (4.4.5)$$

where q is the bunch charge and x is the bunch displacement. The kick factor for the 5-cell BNL cavity was calculated by R. Calaga in his MAFIA simulations:

$$k_\perp = 3.28 \text{ V/pC/m}. \quad (4.4.6)$$

For a 5 nC bunch displaced by 1 mm in the cavity, the average transverse deflection angle at the first cavity (E~12 MeV) is

$$\langle x' \rangle = \frac{\delta p_\perp}{p} = \frac{eqxk_\perp}{\gamma mc^2} = 1.2 \cdot 10^{-6}. \qquad (4.4.7)$$

For higher energy cavities/passes, the deflection angle will be lower inversely proportionally to the beam energy.

Similarly to the energy spread, the angular spread arises from the fact that the head particles experience no deflection while tail particles are deflected on angles larger than the average deflection angle. For the sake of estimate, one can assume that the angular spread is approximately equal to the average deflection angle, that is, $1.2 \cdot 10^{-6}$. This angular spread can be treated as an increase of the projected emittance and has to be added quadratically to the existing bunch angular spread. The angular spread due to the beam emittance at the first cavity will be approximately 10^{-4}. Because the angular spread produced by cavity wake fields is added quadratically, its impact on the beam emittance is negligible.

Resistive wake

Image currents in the wall of the vacuum chamber induce the wake electromagnetic field which can deflect beam particles. The dipole wake proportional to the beam displacement has a largest impact on the beam quality. Therefore, higher order wakes such as quadrupole, etc. can be neglected. Note that the resistive dipole wake does not change the emittance for a given electron bunch slice but increases the projected emittance.

The deflection angle of a particle at the longitudinal coordinate z within a bunch is

$$x'(z) = \frac{N_e r_e}{\gamma} x \int_z^\infty \rho(z') w_\perp(z - z') dz', \quad (4.4.8)$$

where r_e is the classical electron radius, x is the beam displacement from the center of the vacuum pipe, γ is relativistic factor, and the wake function $w_\perp$ is given by

$$w_\perp(z) = -\frac{2L}{\pi b^3}\sqrt{\frac{c}{\sigma|z|}}, \qquad (4.4.9)$$

where b is the beam pipe radius, L the length of the vacuum chamber, and σ is the conductivity of the vacuum pipe material. For a bunch with a rectangular linear charge distribution, the deflection angle is

$$x'(z) = \frac{4L}{\pi b^3}\sqrt{\frac{c}{\sigma}}\frac{N_e r_e}{\gamma l_b} x\sqrt{\frac{l_b}{2} - z}\,. \qquad (4.4.10)$$

At the cooling section, electron bunches reside inside RHIC ion bunches. Therefore, the effect of the ion bunch wake field has to be included with the opposite sign:

$$x'(z) = -\frac{\sqrt{2}L}{\pi b^3}\sqrt{\frac{c}{\pi\sigma}}\frac{ZN_i r_e}{\gamma\sigma_{zi}} x\int_0^\infty \frac{\exp\left[-\frac{(\xi+z)^2}{2\sigma_{zi}^2}\right]}{\sqrt{\xi}} d\xi\,, \quad (4.4.11)$$

where N_i is the number of ions of the charge state Z in an ion bunch, and σ_{zi} is the r.m.s. length of ion bunches. Note that the ion wake changes slowly inside an electron bunch because ion bunches are much longer than electron bunches (σ_{zi}≈20 cm). Therefore, the ion wake induces approximately the same deflection for all electrons.

Using (4.4.10) and (4.4.11), one can calculate the angular spread produced by the resistive wake in the 100 m long cooling section with the stainless steel pipe of radius of 35 mm. Assuming that the bunch is offset by 1 mm, one obtains an r.m.s. angular spread of $5\cdot10^{-7}$. This spread has to be added quadratically to the angular spread of the beam. In the cooling section, the angular spread is approximately equal to 10^{-5}. Thus, one can conclude that the transverse effect of the resistive wake in the cooling section can be neglected.

In the ERL recirculation pass, the electron beam oscillates due to betatron oscillations. The resistive wake can resonantly amplify oscillations of the beam tail causing a transverse breakup within a single bunch. This effect was observed at the SLC and is sometimes referred to as the "banana effect". An increase of the betatron amplitude of the bunch tail normalized to the initial amplitude can be estimated as

$$\mathrm{Y} = -\frac{N_e r_e \langle\beta\rangle}{4\gamma} w_\perp(\sigma_e)\,, \qquad (4.4.12)$$

where σ_e is the longitudinal r.m.s size of electron bunches equal to 1 cm. For the e-cooler parameters, the amplification factor (4.4.12) is only $8\cdot10^{-3}$ after the 100 m long cooling section and, therefore, can be neglected.

4.4.3 Other contributions

As with the energy spread, we do not expect impedance of other vacuum components to produce large contributions to the electron beam angular spread.

4.4.3.1 Coherent Synchrotron Radiation (CSR)

The r.m.s. energy spread and the average particle energy loss, ignoring vacuum chamber shielding, can be estimated from the following expressions:

$$\sigma_E = 0.25\frac{r_e N_e L_{eff}}{\gamma(R^2\sigma_{es}{}^4)^{1/3}}, \qquad (4.4.13)$$

$$<\delta E> = -0.35\frac{r_e N_e L_{eff}}{\gamma(R^2\sigma_{es}{}^4)^{1/3}}, \qquad (4.4.14)$$

where L_{eff} is total effective length of bending path, R is the bending radius, σ_{es} is the rms length of the bunch, N_e is number of electron per bunch and r_e is the classical radius of electron.

Taking typical parameters of the electron beam transport one gets approximately σ_E=0.001 and $<\delta E>$=-0.0014, indicating an energy spread due to CSR larger than the requirement for cooling 0.0005. However, as mentioned before, formulas (4.4.13) and (4.4.14) did not include shielding by the vacuum pipe and, therefore, overestimate the energy spread and energy loss. The effectiveness of shielding is described by the parameter:

$$x_{th} = \frac{2\pi^3 R\sigma_{es}{}^2}{(3h^3)}, \qquad (4.4.15)$$

where h is the gap of the vacuum chamber in dipole magnets and R is the bending radius of the magnets. If x_{th} is much smaller than unity, shielding is negligible and formulas (4.4.13) and (4.4.14) can be used without modifications. If x_{th} is larger than $4\pi^2$, the coherent radiation is completely suppressed. In the range $1< x_{th} < 4\pi^2$, SCR is reduced by the factor $F_r=x_{th}^{-1/3}\exp(-x_{th})$. For the parameters of electron cooler with R=0.5 m and h=0.03 m, equation (4.4.15) yields x_{th} approximately equal to 38. This means that CSR in the e-cooler ERL will be almost completely suppressed by shielding.

Although estimates presented above suggest that CSR effects will be strongly suppressed, a more accurate evaluation of the CSR effect is still needed, including computer simulations of CSR with shielding.

4.4.3.2 Deflection of the beam centroid by image charges

A beam induces image charges on the walls of the vacuum chamber. If the beam is centered inside a round vacuum pipe, the image charges and currents are distributed symmetrically on the walls and exert no coherent force upon the beam. If the beam is offset, the redistributed image charges will impose a coherent force on the beam proportional to the beam offset. As usual, the image charge force consists of the electric and magnetic components. In free space, the electric and magnetic components of the beam space-charge force cancel each other, reducing the net force by the factor γ^2. For the image charges, the relativistic cancellation depends on the frequency spectrum of the beam. The e-cooler beam spectrum consists of harmonics of 10 MHz starting from zero frequency and all the way up to maxim frequency approximately equal to inverse temporal bunch length. For all harmonics except the zeroth, the skin depth is much shorter than the wall thickness. Therefore, there will be the relativistic cancellation for higher frequencies. On the contrary, the magnetic field of the DC component (zeroth harmonic) penetrates through the vacuum chamber, inducing no image currents. Therefore, the electric force by the image charges is canceled by the magnetic field of the image currents for the DC component. Fortunately, the intensity of the DC component is proportional to the beam duty factor and is small for the e-cooler (10^{-3}).

The images of higher frequency harmonics exert the coherent force on beam particles given by:

$$F_x^{hf} = \frac{2e^2 N_e x}{\gamma^2 b^2 l_b}. \qquad (4.4.16)$$

The DC force differs from (4.4.16) by the factor η/γ^2, where η is the beam duty factor:

$$F_x^{dc} = \frac{2e^2 N_e \eta x}{b^2 l_b}. \qquad (4.4.17)$$

The equation of motion of the beam centroid is:

$$x'' = k^2 x, \qquad (4.4.18)$$

where k is the inverse growth scale, given by

$$k^{hf} = \sqrt{\frac{2r_e N_e}{\beta^2 \gamma^3 b^2 l_b}} \text{ or } k^{dc} = \sqrt{\frac{2r_e N_e \eta}{\beta^2 \gamma b^2 l_b}} \qquad (4.4.19)$$

for the high frequency harmonics and for the DC component respectively. Plugging in the number for the e-cooler, one gets the growth length

$$l_{hf} = \frac{1}{k_{hf}} = 550 \text{ m and } l_{dc} = \frac{1}{k_{dc}} = 160 \text{ m}. \qquad (4.4.20)$$

Assuming the initial beam displacement of 1 mm, these forces cause the beam centroid to gain a deflection angle at the end of the 100 m long cooling section equal to $3 \cdot 10^{-7}$ and $4 \cdot 10^{-6}$ respectively. These numbers overestimate the resulting deflection. The presented calculations did not include the focusing effect of the solenoids situated at the cooling section that will practically compensate the deflection produced by the image charges.

4.4.3.3 Ion trapping

Trapping of residual gas ions produced by the electron beam is a well known effect observed in circular and linear accelerators. Ion trapping can distort the linear machine optics, create strong nonlinearities, and enhance beam losses via scattering of electrons on the residual gas ions. Before starting with the analysis, note that ion trapping is not possible in the cooling section because the charge of RHIC ion bunches is larger than that of electron bunches. Therefore, ions can get trapped in the electron beam in the ERL recirculation pass and beam delivery channels.

Stability of trapped ions, accumulation time, and linear effect on the electron beam

Stability of ions inside the electron beam can be studied analytically using the matrix analysis in which the bunch-ion interaction is presented as a thin focusing lens and the time gap between bunches is treated as a drift. This analysis yields the stability criteria for singly ionized ions within the electron beam:

$$A \geq \frac{r_p N_e c t_b}{2a^2}, \quad (4.4.21)$$

where A is the atomic mass of stable ions, r_p is the classical proton mass, N_e is the number of electrons in each electron bunch, ct_b is the distance between centers of two electron bunches, and a is the radius of electron bunches. For the e-cooler parameters in the first pass (charge-per-bunch of 5 nC, normalized beam emittance of 5 μm, beam energy of 25 MeV, bunch repetition rate of 10 MHz, and a beta function of 10 m), Equation (4.4.21) yields the mass of stable ions

$$A \geq 0.23, \qquad (4.4.22)$$

indicating that ions of all gas species can accumulate in the electron beam at least in some locations around the ERL.

Each electron ionizes residual atoms with an average rate of

$$\tau^{-1} = nc\sigma, \quad (4.4.23)$$

where n is the number of residual gas atoms in a unit volume and c is the velocity of electrons assumed to be equal to the speed of light. Using a simple model that includes the space charge force of accumulated ions, one can obtain the average neutralization degree ξ as a function of time as:

$$\xi(t) = \frac{N_i}{N_e} = 1 - e^{-\frac{t}{\tau}}, \quad (4.4.24)$$

where N_i is the total number of ions accumulated on the path-length equal to the distance between centers of two neighboring electron bunches, ct_b, and N_e is the number of electrons in each electron bunch. For the expected pressure of hydrogen (σ=3·10^{-19} cm^2) of 10^{-10}, equation (4.4.23) yields the characteristic accumulation time

$$\tau \approx 30 \text{ sec}. \quad (4.4.25)$$

The operational experience with trapped ions accumulated worldwide shows that the stability analysis presented above and the trapping time calculations are in a reasonably good agreement with experimental results. However, the same experience shows that it is hard to exactly predict the effect of trapped ions on the electron beam. In this paper, we will calculate only the impact of trapped ions on the betatron phase advance assuming a linear focusing force produced by the ions. Later we will use these calculations to set the limit on the maximum neutralization degree assuming that non-linear effects are small if the linear focusing is small. The additional betatron phase advance $\delta\mu$ due to the ion focusing can be estimated as:

$$\frac{\delta\mu}{\mu} = \frac{\int \beta(\partial F/\partial x)ds}{2pc\int \beta^{-1}ds} = \frac{r_e n_e \langle\beta\rangle}{\varepsilon_n}\xi, \quad (4.4.26)$$

where $\partial F/\partial x$ is the derivative of the transverse force produced by ions, β is the beta function, r_e is the classical electron radius, ε_n is the normalized electron beam emittance, n_e is given by N_e/ct_b, and ξ is the neutralization degree as defined in (4.4.24). For the e-cooler ERL, equation (4.4.26) yields $\delta\mu/\mu \sim 5.8$, meaning a strong focusing due to ions in the case of full neutralization (ξ=1). Note that equation (4.4.26) is accurate only for $\delta\mu/\mu << 1$. As mentioned above, this equation will be used later in the limit of a weak ion focusing to set the maximum allowed neutralization degree.

Clearing time gaps and maximum time interval between clearing gaps

In the case when the regular electron beam with a bunch rep. rate of 10 MHz is interrupted by periodic, long clearing gaps, the trapped ions will be unstable if the following approximate inequality is satisfied:

$$\left|\sqrt{4+(\omega_i T_c)^2}\cos(\mu_i N_b + \varphi_i)\right| > 2, \quad (4.4.27)$$

where T_c is the duration of the clearing gap, N_b is the number of bunches in trains separated by clearing gaps, ω_i is the frequency of oscillations of a specific ion species within the electron beam, μ_i is the ion phase advance per time gap between two electron bunches, $\omega_i \cdot t_b$, and the phase φ_i is given by $\tan(\varphi_i) = \omega_i T_c/2$. Obviously, the condition (4.27) cannot be satisfied for all ion species simultaneously because of the cosine. However, clearing gaps will effectively clear ion species in the ERL if the following inequality holds:

$$\sqrt{4+(\omega_i T_c)^2} >> 2 . \quad (4.4.28)$$

Figure 4.4.1 shows the value of the expression $\sqrt{4+(\omega_i T_c)^2}$ for the cooler ERL as a function of the atomic weight of ions. From the figure, one can conclude that 300 nsec clearing gaps will not provide effective clearing, 1 μsec long clearing gaps will clear effectively only light ions with A<5, while 3 μsec gaps will provide effective clearing of all ions with masses up to 50.

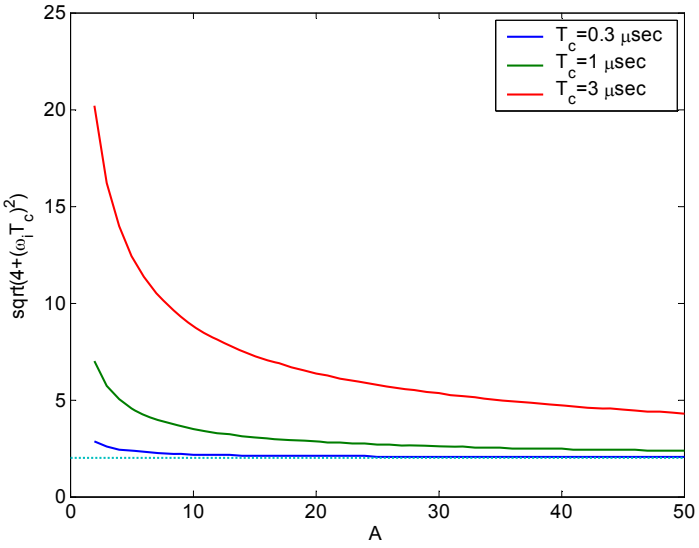

Figure 4.4.1: Value of $\sqrt{4+(\omega_i T_c)^2}$ as a function of ion mass. Dashed blue line is y=2.

The time interval between clearing gaps can be calculated from a condition on the maximum allowed neutralization degree corresponding to an acceptably small betatron tune shift due to trapped ions. Assuming the maximum tune shift $\delta\mu/\mu$ of 0.05, equations (4.4.24) and (4.4.26) yield the maximum length of 10 MHz bunch trains as

$$t = \tau \left(\frac{\delta\mu}{\mu} \right)_{\max} \frac{\varepsilon_n}{r_e n_e \langle\beta\rangle} = 0.25 \,\text{sec}, \quad (4.4.29)$$

where all used notations were introduced above.

Using 3 μsec long clearing gaps to clear trapped ions can cause prohibitively large RF transient effects if the beam current is turned off and on instantaneously. To avoid sharp RF system transients the beam current can be slowly ramped up and down with a transition time of a few milliseconds and clearing gaps of a few microseconds or even milliseconds. According to equation (4.4.29), this operational regime still will provide the beam with a duty factor of 99% or so.

Clearing electrodes

Clearing electrodes are another method that can be used to clear trapped ions from the electron beam. The electrostatic field of such electrodes draws trapped ions out of the electron beam when ions reach the area where the electrodes are situated. The evolution of the density of trapped ions is described by the equation:

$$\frac{dn_i}{dt} = \dot{n}_i^+ - \frac{n_i}{\tau^-}, \quad (4.4.30)$$

where n_i is the average linear ion density, $\dot{n}_i^+$ is the term describing the ionization process, and τ^- is the life-time of trapped ions. This equation does not include the space charge of accumulated ions assuming a low neutralization degree. The asymptotic solution of this equation is a constant:

$$n_i(t \to \infty) = \dot{n}_i^+ \tau^- , \qquad (4.4.31)$$

which can be rewritten using the neutralization degree ξ as:

$$\xi(t \to \infty) = \frac{\tau^-}{\tau} . \qquad (4.4.32)$$

The life time of a trapped ion depends on many details including the ion thermal velocity, the amount of momentum transfer during ionization, location in the ERL where ionization occurred, neutralization degree, etc. However, it is safe to assume that the life time of trapped ions will be no longer than the distance between two sets of clearing electrodes divided by the average thermal velocity of ions. (This is incorrect for dipole magnets where ions are magnetized. However, dipole magnets occupy only a small portion of the ERL circumference.) Assuming that the distance between two electrode sets is 5 m, the thermal velocity of H_2^+ ions of 1000 m/sec, and other parameters described above, one gets a the maximum life time of ions of 5 msec. Equation (4.4.26) yields the additional betatron phase advance due ion focusing equal to $5 \cdot 10^{-4}$, which is negligible.

4.4.3.4 Electron cloud

The charge of cooled RHIC ion bunches exceeds the charge of electron bunches by a factor of a few. This prevents ion trapping in the cooling section but opens the door to the electron cloud effect, which was observed in warm sections of RHIC. According to measurements done at RHIC the linear charge density of the electron cloud, if not suppressed, is of the order of 1 nC/m with an r.m.s. transverse size of the cloud distribution, σ_{ec}, of the order of 2 cm. The defocusing due to the e-cloud can be characterized by the characteristic growth length, given by:

$$k_{ec} = \sqrt{\frac{r_e n_{ec}}{2\gamma\sigma_{ec}^2}} , \qquad (4.4.33)$$

where n_{ec} is the number of e-cloud electrons per unit length. For the cooler parameters, equation (4.4.33) yields the characteristic growth length equal to 70 m and the r.m.s. angular spread at the end of the 100m long cooling section equal to $1.4 \cdot 10^{-4}$, which is much larger than the specification on the angular spread in the cooling section. Calculations show that the e-cloud charge density has to be lowered by a factor of 20 to lower the angular spread below $5 \cdot 10^{-6}$.

NEG coating of vacuum pipe proved to reduce the e-cloud density by more than an order of magnitude. We also expect additional e-cloud suppression by the field of the undulator wrapped on the vacuum chamber of the cooling section. After the e-cloud will be suppressed by NEG coating, the linear part of the residual angular spread growth can be compensated by the focusing solenoids designed to compensate the beam space charge at the cooling section. Additional suppression of the effective secondary emission coefficient by a factor of a few can be achieved by modifying the vacuum pipe surface if this is necessary.

The operational experience with the electron cloud at RHIC and simple estimates show that the aforementioned methods and tools will allow us to keep the electron cloud under control. However, considering the potential seriousness of this problem we plan to continue detailed studies and simulations of the effect.

4.4.3.5 Intra-beam scattering (IBS)

Intra-beam scattering within the electron beam

For the present parameters of electron beam, the longitudinal r.m.s. velocity spread of electrons in the beam frame is smaller than transverse. The transverse-longitudinal relaxation due to IBS results in an increase of the longitudinal r.m.s. velocity spread. A relative fractional increase of the longitudinal rms velocity spread after 100 meters was found to be at the 10^{-4} level, which is considered to be negligible.

Intra-beam scattering between the electron and ion beam

A relative increase of the longitudinal r.m.s. velocity spread was found to be less than 1% as a result of 100 meters of interaction with the ion beam, which is considered to be negligible.

4.4.4 REFERENCES

[1] Electron Cooling for RHIC, I. Ben-Zvi, et al., Proceedings of the 2001 Particle Accelerator Conference, Chicago, IL, USA, June 18-22, 2001, p.48
V.V. Parkhomchuk and I. Ben-Zvi, Tech. Report C-AD/AP/47 (2001).
[2] D.Janssen et al., NIM A, 507 (2003) pp 314-317.
[3] L. M. Young, J. H. Billen, "Parmela documentation", LA-UR-96-1835.
[4] Xiangyun Chang, Ilan Ben-Zvi, and Jörg Kewisch, “Emittance compensation of compact superconducting guns and booster linac system”, Phys. Rev. ST Accel. Beams 9, 044201 (2006).
[5] L. Serafini and J. B. Rosenzweig, Phys. Rev. E 55, 7565 (1997).
[6] V.N. Litvinenko, R. Hajima, D. Kayran,.”Merger designs for ERL”. NIM A 557, (2006) pp 165-175.
[7] E. Pozdeyev, Phys. Rev. ST Accel. Beams 8, 054401 (2005).
[8] G. A. Krafft and J. J. Bisognano, in Proceedings of the 1987 Particle Accelerator Conference, Washington, DC (IEEE Catalog No. 87CH2387-9), pp. 1356–1358.
[9] R. R. Calaga, Ph. D. Dissertation, Stony Brook University
[10] A. W. Chao, Physics of Collective Beam Instabilities in High Energy Accelerators, John Wiley & Sons, Inc., 1993
[11] J. Qiang, R. Ryne, B. Blind, J. Billen, T. Bhatia, R. Garnett, G. Neuschaefer, and H. Takeda, "High resolution parallel particle-in-cell simulations of beam dynamics in the Spallation Neutron Source linac," Nucl. Instr. Meth. Phys. Res. A, 457, 1 (2001).
[12] G. Pöplau, U. van Rienen, K. Flöttmann: 3D SPACE CHARGE CALCULATIONS FOR BUNCHES IN THE TRACKING CODE ASTRA, Proceedings of EPAC 2006, Edinburgh, Scotland
[13] R.D. Ryne et al: A TEST SUITE OF SPACE-CHARGE PROBLEMS FOR CODE BENCHMARKING, Proceedings of EPAC 2004, Lucerne, Switzerland
[14] A. Franchi et. al.:Benchmarking linac codes for the HIPPI project, ICFA 2004
[15] C. Limborg et al: CODE COMPARISON FOR SIMULATIONS OF PHOTO-INJECTORS, SLAC-PUB-10735
[16] J Kewisch, X.Y. Chang: Emittance Compensation for Magnetized Beams, to be published, PAC 2007
[17] Frank Vanden Berghen. Optimization algorithm for Non-Linear, Constrained, Derivative-free optimization of Continuous, High-computing-load, Noisy Objective Functions. Technical report, IRIDIA, Universit_e Libre de Bruxelles, Belgium, may 2004. Available at http://iridia.ulb.ac.be/_fvandenb/work/thesis/.

Appendix 4.A

4.A.1 Code Comparison and Optimization of the RHIC Electron Cooler Injector

The RHIC electron cooler requires an electron beam with a bunch charge of 5 nC and a normalized emittance of less than 4 μ. The beam is created in a 1½ cell SRF electron gun, where it is accelerated to about 5 MeV. It is then focused by a solenoid and passes the dipole merging system, where the used bunches are injected back into the accelerating cavities for energy recovery. Because of the low beam energy in this region the beam dynamics is strongly influenced by the space charge forces and some emittance increase is unavoidable. Through careful optimization of the beam size, focusing and timing the beam emittance can be minimized at the exit of the linac.

In addition a new technology may be used to improve the beam quality of the cooler injector: Shaping the spatial dimensions of the laser pulse shapes the electron bunch. The creation of a cylindrical distribution (beer can) is establish technology. A better but more difficult to achieve shape is an ellipsoid, where space charge fields inside the bunch are linear. The shape can be improved when the ellipsoid is slightly deformed (tear drop) to counteract space charge effects during the emission from the cathode.

There are a number of computer codes available that include the space charge force in the calculation of beam dynamics. For the design of the ERL we used the well-established code PARMELA [3], which has been benchmarked with many accelerators. Since the brightness of the electron cooler beam pushes the envelope it was desirable (and suggested by the Machine Advisory Committee) to verify the PARMELA results with other computer codes.

Two codes were used: ImpactT [11] and ASTRA [12]. Benchmarking of these codes has been done before [13, 14, 15]. The strongest effects of the space charge force occur at low energies. Therefore the dependence of the beam dynamics on the integration parameters was investigated from the cathode to the exit of the gun.

After establishing some confidence in the PARMELA results we discuss an optimization strategy and present the optimization results for both the beer can and tear drop distribution for various bunch charges.

Finally we investigate the influence of beam haloes on the beam emittance.

4.A.1.1 Layout of the injector

The beam line contains the following elements:

1. Cathode. A transverse temperature of 0.1 eV is assumed in all calculation. This is the expected value of the diamond cathode. The bunch shape of the tear drop distribution is given in Figure 4.A.3.
2. 1½ cell 700 MHz SRF gun as shown in figure 4.A.2. The length from the cathode to the exit of the gun is 48 cm. The gun has a recessed cathode to provide focusing to the beam. A choke allows removing the cathode assembly.
3. 10 cm solenoid S1
4. 24 cm drift

5. The Z-bend merging system, which re-injects the high energy electron beam into the accelerating cavity for energy recovery:
    a. 10 cm chevron dipole, deflecting 10 degrees.
    b. variable drift D1
    c. 20 cm chevron dipole, deflecting –20 degrees
    d. variable drift D2
    e. 20 cm chevron dipole, deflecting 20 degrees
    f. 40 cm drift
    g. 10 cm chevron dipole, deflecting -10 degrees.
6. 10 cm drift
7. 10 cm solenoid S2
8. variable drift D3
9. Accelerating Cavity 700 MHz(variable phase)
10. 20 cm drift
11. 2100 MHz cavity, 37.3 cm
12. 100 cm drift
13. 20 cm solenoid 0.2 kG
14. 109.2 cm drift
15. Cavity 700 MHz, 138 cm
16. 60 cm drift
17. 20 cm solenoid 0.5 kG
18. 134 cm drift
19. 50 cm drift
20. 20 cm solenoid 2 kG
21. 170 cm drift
22. Cavity 700 MHz
23. 70 cm drift
24. 20 cm solenoid 2 kG
25. 119 cm drift
26. 2100 MHz cavity
27. 40 cm drift
28. 20 cm solenoid, 1.8 kG
29. 120 cm drift
30. 700 MHz cavity
31. 70 cm drift

The layout of the linac is preliminary and not critical to the beam quality. It will be adjusted when the design of the cavities is completed.

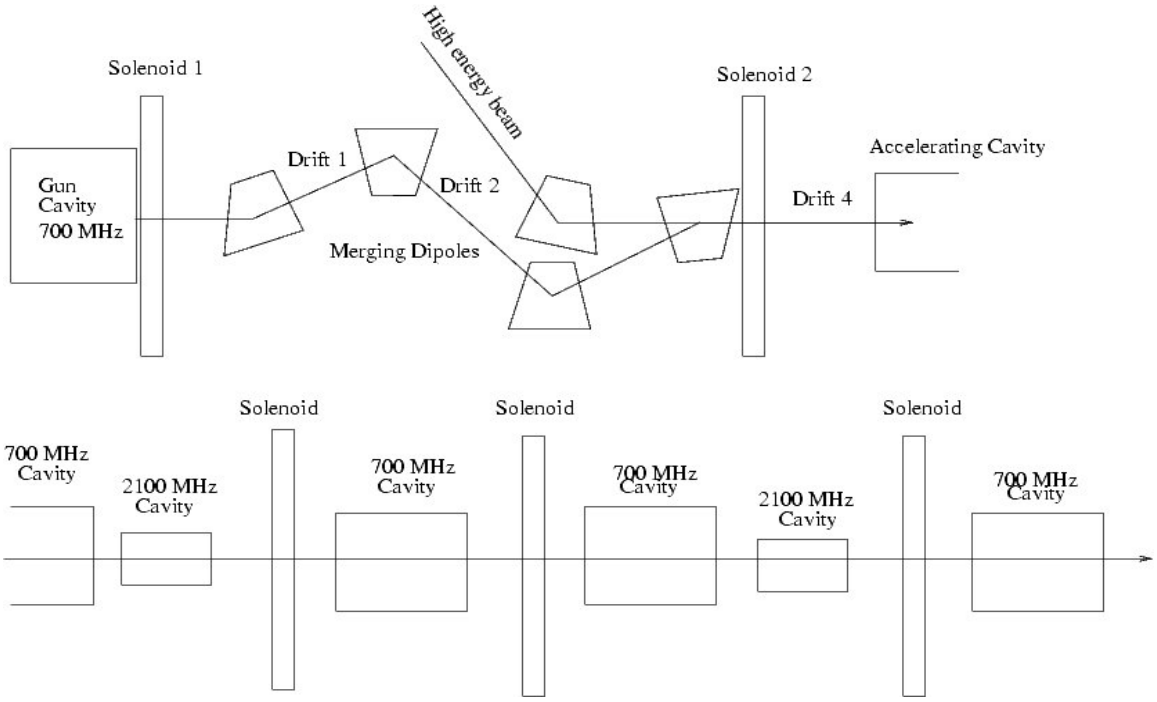

Figure 4.A.7: Injector Layout

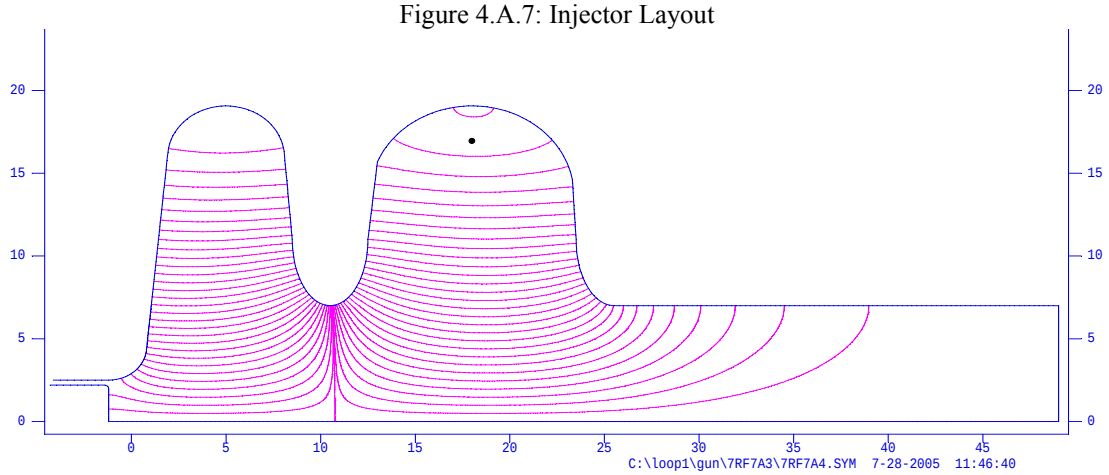

Figure 4.A.8: SUPERFISH calculation of the electron gun.

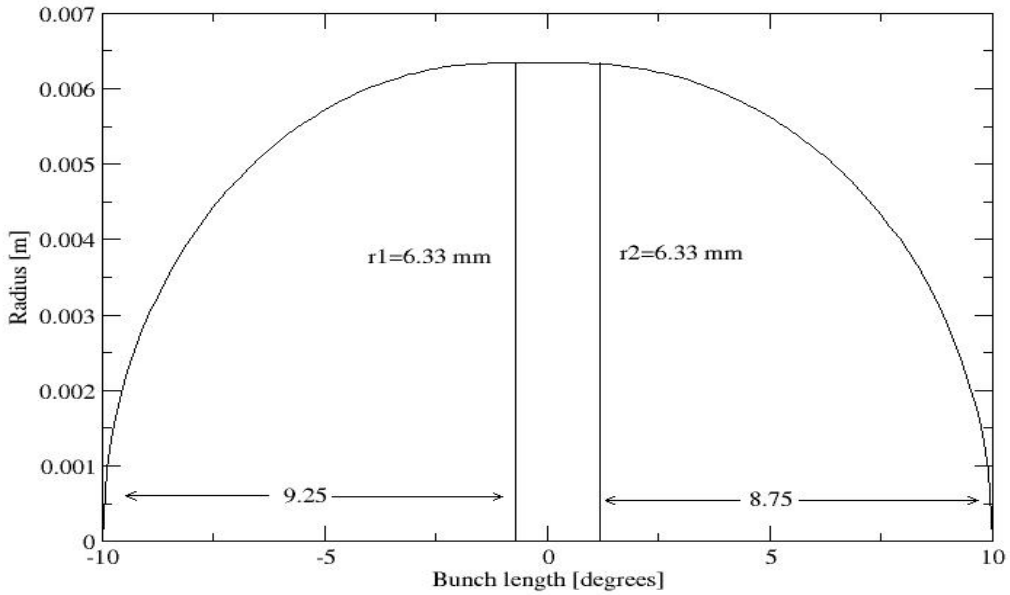

Figure 4.A.9: Electron bunch shape.

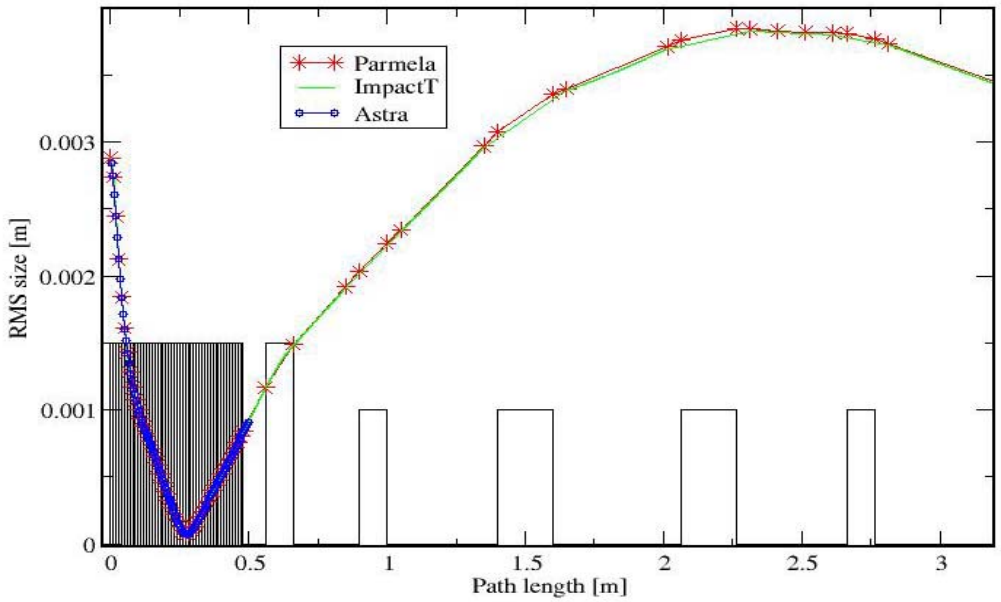

Figure 4.A.10: Envelope without space charge forces.

4.A.1.2 Calculations without space charge

Before we compare the calculation of the space charge effects in the three computer codes we compare the beam dynamics without space charge and discuss the differences in the result. Figure 4.A.4 shows the envelope of the beam calculated by the three programs. We see a perfect agreement between all three programs in the gun.

In order to further confirm the agreement we compare also the projected beam emittances, which are shown in Figure 4.A.5. Although the emittances are different inside the gun they agree at the gun exit. The reason for this behavior is the difference in the calculation of the emittance. The emittance is defined for a point in space, while the particle motion is calculated as a function of

time. PARMELA stores the coordinates of the particles when they leave each element and calculates the emittance in a post-processing step. ImpactT calculates the emittance on the fly by propagating all particles in a straight line to the position of the reference particle. In places with strong RF focusing this method produces a large error.

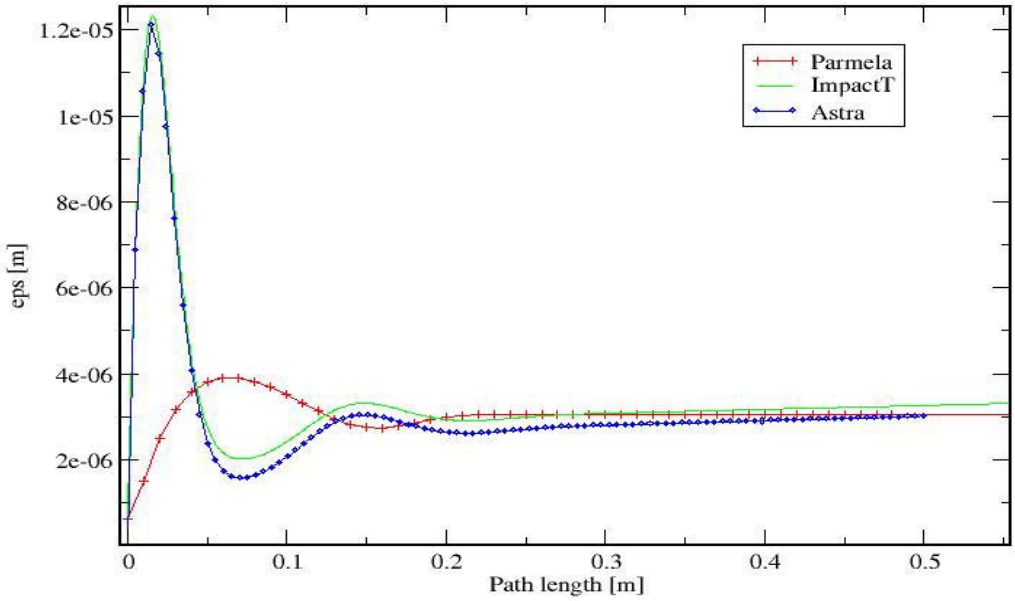

Figure 4.A.5: Beam emittance without space charge forces.

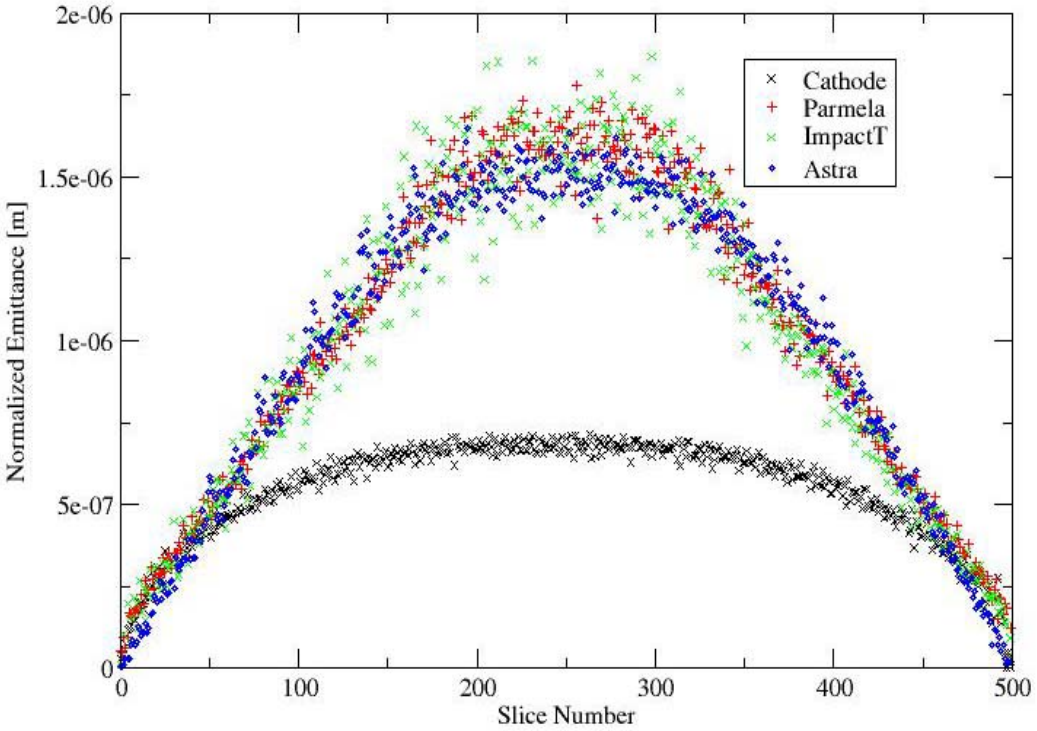

Figure 4.A.6: Slice emittances at the gun exit without space charge forces

Last, we inspect the slice emittances at the exit of the gun, shown in Figure 4.A.6. The bunch is cut longitudinally into 500 equal length slices and the emittance is calculated for each slice. This

removes the above-mentioned error in the emittance calculation. For comparison the slice emittances at the cathode are included. The elliptical radius and the constant transverse temperature give them.

We see a good agreement of the three programs when the space charge forces are turned off. Any differences in the calculations with space charge are therefore caused by differences in the space charge calculation methods

4.A.1.3 The Influence of Space charge parameters

The numerical integration of the electron motion is necessarily an approximation. An exact result would require computing power that is not available. A number of parameters control how the approximations are performed. The simulation results are strongly influenced by the choice of the space charge integration parameters and a good choice of parameters is essential for a comparison of the three programs. The following parameters were used:

The time step size

The step sizes for the integration are listed in table x. A test with ten times finer step size gave the same results within 0.5%.

Flight time	Parmela step size	Impact step size	Astra step size
0 to 0.1 degrees	0.1 degrees = 0.40 ps	0.1 degrees = 0.40 ps	variable
0.1 to 25 degrees	0.2 degrees = 0.79 ps	0.1 degrees = 0.40 ps	0.04 to 4 ps
After 25 degrees	0.5 degrees = 1.97 ps	0.5 degrees = 1.97ps	

Number of bins

The space charge forces are calculated in the following way: The bunch volume is cut into bins specified by the transverse and longitudinal number of intervals. The particle density in each bin is calculated. The system is then transformed into the co-moving frame of the bunch, where the particle velocities are non-relativistic and the magnetic fields are negligible. The electric fields are then calculated and transformed into electric and magnetic fields in the lab system, where the particle motion is calculated.

The number of bins has to be large enough to accurately describe the charge distribution. For PARMELA and ASTRA a grid of 50x500 was used. In ImpactT we used 128x128x128. This was limited by the available memory of the computer.

The number of macro particles

A rule of thumb is that there should be on average at least 10 macro particles in each bin for a smooth calculation of the space charge force. Since we used for our calculations 50 transverse bins and 500 longitudinal bins this rule requires $25 \cdot 10^3$ particles. We verified that, when using more than $50 \cdot 10^3$ particles, the results are stable. Our calculations were done with $250 \cdot 10^3$ particles

4.A.1.4 Comparison results

After comparing the calculations without space charge and verifying the validity of the space charge parameters we can now compare the space charge calculations of the three programs. Figure 4.A.7 shows the envelope calculated with PARMELA (red stars), IMPACT (green line) and ASTRA (blue circles). The boxes indicate the region of the gun cavity and the focusing solenoid. PARMELA predicts a larger envelope than ImpactT, ASTRA seems to agree in the beginning with PARMELA and later with ImpactT. There is no obvious explanation for the difference.

Figure 4.A.8 shows the projected emittances inside the gun. As in Fig. 4.A.5 the emittances converge towards the exit of the gun, when the transverse fields become zero and the particles move approximately in a straight line. Also like in Fig. 4.A.5 ASTRA and PARMELA converge to the same value, while ImpactT is slightly different.

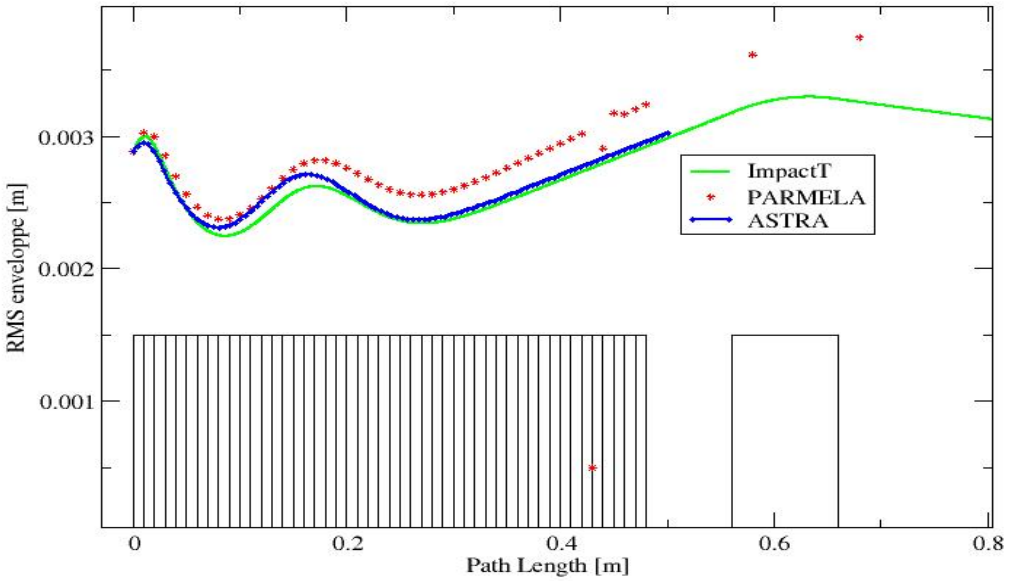

Figure 4.A.7: Beam envelopes calculated with PARMELA and ImpactT and ASTRA with space charge forces included.

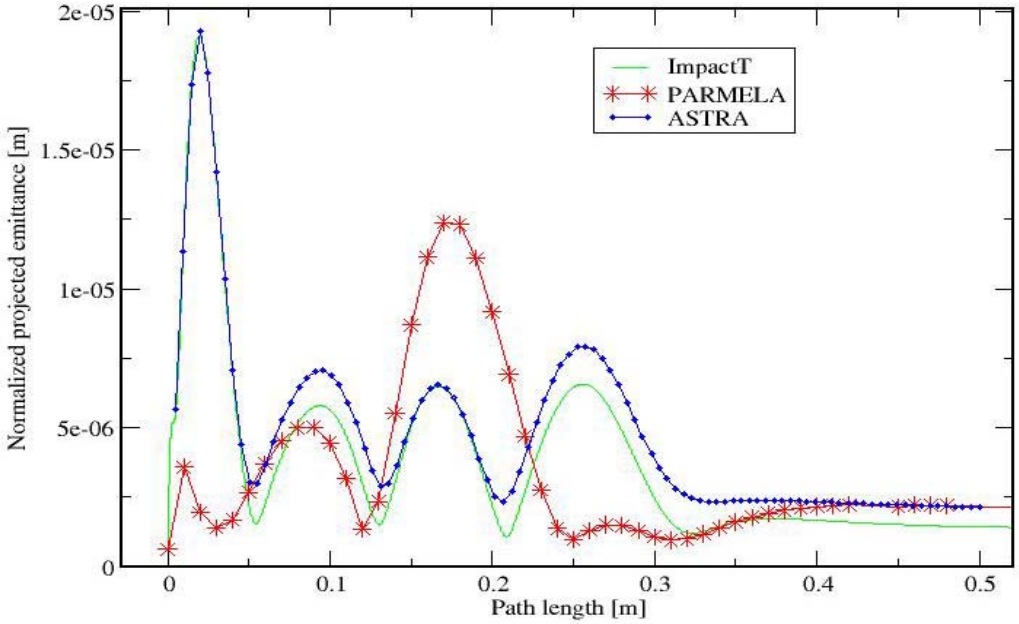

Figure 4.A.8: Projected emittances in the gun with space charge forces included

For further investigation of the differences we plot the slice emittances at the exit of the gun in Fig. 4.A.9. The slice emittances present information about the non-linearity of the transverse motion, while the projected emittance is usally dominated by the relative motion of the longitudinal slices due to the time dependence of the RF fields and the local charge density.

The setup of the injector we are using in this comparison has been optimized with the PARMELA program. One of the optimizing steps is to minimize the slice emittances at the exit of the gun by varying the bunch shape and the gun cavity fields. Therefore the slice emittances of PARMELA are close to the thermal emittance.

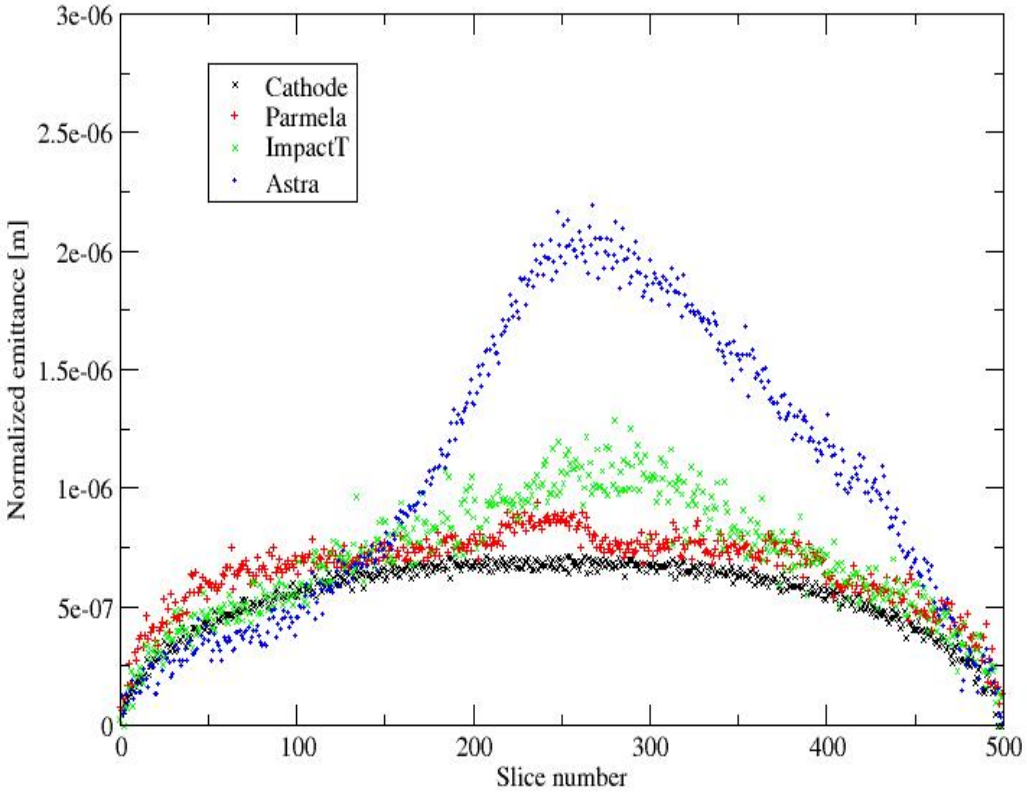

Figure 4.A.9: Slice emittance as a function of the position inside the bunch

The ImpactT slice emittances are reasonably close to the PARMELA results. ASTRA produces a much different result. The slice emittances are asymmetric over the longitudinal dimension (Some asymmetry seem to be present also in the ImpactT curve). This could be explained by the fact that when the electrons leave the cathode the particles in the head of the bunch (left side in the graph) experience less charge than the particles in the tail of the bunch. However, there is no explanation for the decrease of the slice emittances compared to the slice emittances at the cathode.

Since the space charge effects cause these differences we tried to eliminate them by varying the bunch charge empirically so that the beam size at the exit of the gun is identical. The charge in ImpactT had to be increased by 14%, the charge in ASTRA by 8%. Figure 4.A.10 shows the resulting envelopes. The adjustment of this one parameter produces a perfect agreement inside the gun. The curves diverge slightly in the following solenoids and dipoles. This is most likely caused by the fact that the ImpactT magnets are described by a smooth field curve while the PARMELA magnets have a hard edge.

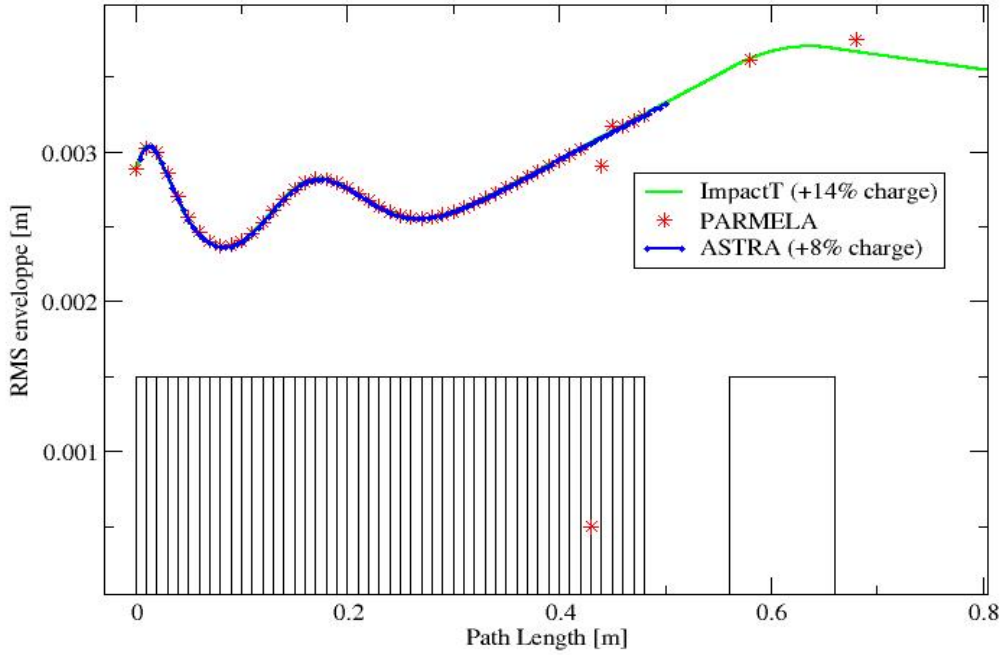

Figure 4.A.10: Envelopes with adjusted bunch charge.

The slice emittances as well as the projected emittances change little with the adjustment of the bunch charge. Since the figures look on first sight identical to Fig. 4.A.8 and Fig. 4.A.9 the results are therefore given as a table instead of a graph:

	Projected Emittance	Max Slice Emittance
PARMELA	2.21μ	0.94 μ
ImpactT	1.45 μ	1.29 μ
ImpactT +14%	1.72 μ	1.42 μ
ASTRA	2.17 μ	2.18 μ
ASTRA +8%	2.28 μ	2.28 μ

We find a disagreement in the space charge calculation between PARMELA, ASTRA and ImpactT, which is not mentioned in other benchmarking papers. The disagreement is also inconsistent: In some aspects ASTRA agrees with PARMELA, in other aspects ASTRA agrees with ImpactT. Due to the closed source of PARMELA and ASTRA it is not possible for us to investigate the cause of the difference.

	Envelope	Emittance	Slice Emittances
No Space Charge	All programs agree	PARMELA and ASTRA agree, ImpactT 10 % larger	All programs agree
With Space Charge	ImpactT and ASTRA close, PARMELA larger	PARMELA and ASTRA agree, ImpactT 10 % smaller	PARMELA and ImpactT agree, ASTRA larger
Adjusted Space Charge	All programs agree	PARMELA and ASTRA agree, ImpactT 5 % smaller	PARMELA and ImpactT agree, ASTRA larger

On the 30% level the codes agree reasonably well. This may be the best one can expect from the particle tracking method. The current computer technology still limits the accuracy of such calculations. One has to keep in mind that the setup we discussed in this paper pushes the brightness envelope by using especially shaped bunches and a super-conducting gun with a maximum electrical field of more that 30 MeV/m. What used to be noise now becomes a major contribution to the emittance growth?

PARMELA gives the most conservative results. It is also the most widely used and benchmarked program. It is therefore a reasonable approach to base the design of the RHIC electron cooler on PARMELA results.

4.A.2 Optimization process

The emittance blow-up is caused by three mechanisms:

- The non-linearity of the transverse space charge forces and external fields. There is some cancellation if the beam size is chosen correctly.
- The longitudinal variation of the linear forces caused by the time dependence of the fields and the charge distribution in the bunch. This can be mitigated by the process of emittance compensation [5]: By carefully choosing the focusing and drift length after the gun the space charge itself can be used to reverse the emittance blow up.
- The dispersion of the merging system causes coupling of the longitudinal motion into the transverse direction. By using the Z-bend system [6] this effect is strongly reduced.
- Chromaticity

The CONDOR optimizer [17] is used for the optimization. This package was developed for the industry and is aimed at “expensive and noisy” calculations, such as chemical reactions and turbine design and is an algorithmic extension of Powell's UOBYQA algorithm ("*Unconstrained Optimization BY Quadratical Approximation*"). The algorithm brackets the minimum in n-dimensional space and does not use derivatives calculated from differences. The initial step size is therefore choosen as large as possible which reduces the influence of noise. In our case the noise on the results is caused by the limited number of tracked particles and the number of bins in the space charge calculation.
The following parameters are used to minimize the emittance blow-up:

- The beam radius and length. Enlarging the radius will reduce the space charge forces, but increase the thermal emittance. Enlarging the bunch length reduces the space charge forces, but increases the energy spread and the effect of chromaticity.
- The gun voltage and start phase. This will influence the time (RF phase) when the bunch passes the center iris of the gun which affects the transverse focusing. It also changes the energy spread of the bunch at the exit of the gun which causes emittance growth through chromaticity. The energy spread is therefore another quality indicator (with a lesser weight).
- The focusing with two solenoids and distance between the gun and the linac are used for emittance compensation.

- The drift length between the merging dipoles minimizes the longitudinal-transverse coupling.

It is important to find a good starting point for the optimization, so that the optimizer does not get stuck in a local minimum. The optimization also becomes more complex and time consuming with the number of variables. Therefore the optimization is performed in multiple steps:

1. The first step finds a good starting point for the gun parameters. The sum of the slice emittances is minimized at the exit of the gun. PARMELA is used for the function evaluation. 250000 particles are tracked and the slice emittances are calculated by cutting the bunch longitudinally into 500 slices and calculating the emittance for each slice. Those emittances are the added quadratically, weighted by the number of particles in the slice. This gives a measure of the beam quality that excludes the first blow-up mechanism. The result would be the best parameter set if the following emittance compensation is perfect. The bunch length was fixed to ±10 degrees. Including the bunch length as a parameter resulted either in a minimal change or in a worse result. Once a good parameter set is found it can be used as a start point for calculations with different bunch charge and transverse temperature.
2. The second step finds a starting point for the optics from the exit of the gun to the the exit of the first linac cavity using the program SLENV [16]. SLENV integrates the slice envelopes of the bunch using the well known differential equation and calculate an approximate emittance. The function evaluation takes about 1 second (compared to 45 minutes for PARMELA) and allows rapid scanning of the parameter space. Parameters are the solenoid strength and the drift length between the solenoid and the accelerating cavity. SLENV is also used to minimize the dispersion in the merging section.
3. The beam line is set up according to the SLENV results. The cavity phases are optimized to minimize the energy spread throughout the linac. This is done with 20000 particles to save time
4. The same optimization is then performed using PARMELA for the function evaluation, using the SLENV results as a start point. The restart function of PARMELA is used to save the recalculation of the gun in every step. The drift length between the Z-bend dipoles are used as additional optimization parameters. The figures of merit are the projected emittances at two locations downstream of the accelerating cavity. A solenoid is between these points. If only one location is used the optimizer will try to make the beam size in the observation point zero, resulting in an optimal emittance in this point and a strong emittance growth afterwards.
5. Next the whole system is optimized with PARMELA. All parameters except the Z-bend drifts are used. An improvement of 10%-25% is achieved in this step.
6. Finally the cavity phases and the amplitude of the 3rd harmonic cavity in the linac are adjusted to minimize the energy spread at the end of the linac.

Following this recipe does not guarantee a well optimized injector. At each step the results must be inspected and if necessary repeated with a different start point to avoid a local minimum. Typically the complete optimization takes two weeks of compute time.

The results of these optimizations are summarized in Tab. 4.1.3. A significant improvement is gained from using the tear drop shape. The emittance is reduced by 60 %. Alternatively, one can increase the bunch charge to 10 nC and reduce the cooling time by a factor of two. Figures 4.1.15 and 4.1.16 show the projected emittances as a function of path length from the cathode to the end of the linac.